Diss. ETH. No. 25307

A Wearable Sensor Architecture for High-Quality Measurement of Multilead ECG and Frequency-Multiplexed EIT

A thesis submitted to attain the degree of

DOCTOR OF SCIENCES of ETH ZURICH

(Dr. sc. ETH Zurich)

presented by

Michaël Rapin

M. sc. Electrical Engineering, EPFL, Lausanne

born on the 21st of December, 1985

citizen of Corcelles-près-Payerne, Switzerland

accepted on the recommendation of

Prof. Dr. Jess Gerrit Snedeker, examiner

Prof. Dr. Walter Karlen, co-examiner

Dr. Olivier Chételat, co-examiner

2018

Happiness only real
when shared.
— Christopher McCandless

To my Family

Abstract

Recently, telemonitoring of vital signs has gained a lot of research interest. Patients suffering from chronic diseases, such as congestive heart failure (CHF), chronic obstructive pulmonary disease (COPD), or poorly controlled hypertension could benefit from remote continuous monitoring. An essential requirement for telemonitoring systems is ease of use. At the same time, telemonitoring systems need to be highly integrated so patients can monitor their vital signs during their daily life with minimal inconvenience.

A large set of vital parameters can be measured from the chest. For instance, chronic heart diseases can be evaluated via multilead electrocardiogram (ECG) measurements. Some studies also show the ability of electrical impedance tomography (EIT)—a safe and low-cost medical imaging modality—to assess relevant vital signs for COPD, asthma, and cystic fibrosis patients. EIT has also shown the ability to assess hemodynamics such as cardiac output, pulmonary or mean arterial blood pressure.

An integrated system offering the possibility to closely monitor physiological parameters in a patient's everyday environment is desirable. This thesis describes the development of a wearable system able to simultaneously measure high-quality multilead ECG and multichannel bioimpedance for EIT imaging. To maximize its ease of use, the sensors are integrated in a vest and dry electrodes are used.

First, a novel electrical architecture composed of so-called cooperative sensors is reported. While the classical ECG/EIT architectures use (double) shielded or multi-conductor cables to connect the electrodes to a central unit (leading to systems too bulky for wearables), the cooperative-sensor architecture significantly reduces the cabling complexity (neither shielded, nor multi-conductor cable) and eliminates the presence of the central unit. This results, without any impact on signal quality, in systems with easier integration.

To demonstrate the reliability of the proposed architecture, a 12-lead ECG monitoring system was designed with cooperative sensors. The measured peak-to-peak noise is approximately $30\,\mu V$. Moreover, measurements on a healthy volunteer showed that the noise level measured with the cooperative-sensor system (using dry electrodes) is equivalent to the one measured with a gold standard medical device (using gel electrodes).

By extending the cooperative-sensor architecture to multichannel bioimpedance measure-

ment, a wearable and easy-to-use system for EIT and multilead ECG measurements was designed. The fully-parallel EIT structure (meaning that all measuring currents and all resulting voltages are simultaneously injected and measured) avoids the use of multiplexers by the application of multiple current sources and multiple voltage measurements, allowing for flexible and adjustable stimulation/measurement patterns via a frequency-division multiplexing approach. The matching between the current sources and voltage measurements was calibrated with an accuracy of the impedance measurement of $\pm0.67\%$ (measured on a $150\,\Omega$ resistance). The noise measured on this same resistance was $8.73\,\mathrm{m\Omega}$ (standard deviation).

Finally, a qualitative evaluation on one human subject already showed promising and meaningful results, paving the way towards a new generation of wearable and easy-to-use systems for noninvasive cardiovascular monitoring with synchronous ECG/EIT measurement and variable electrode positions and numbers.

Key words: Wearable sensors, telemonitoring, electrocardiography (ECG), multilead, 12-lead ECG, biopotential, bioimpedance, electrical impedance tomography (EIT), frequency-division multiplexing (FDM), electronic circuit calibration, active electrodes, cooperative sensors, dry electrodes, body sensor networks (BSN).

Résumé

Dernièrement, la télésurveillance des signes vitaux a suscité beaucoup d'intérêt dans le domaine de la recherche. Les patients souffrant de maladies chroniques (telles que l'insuffisance cardiaque congestive (ICC), la bronchopneumopathie chronique obstructive (BPCO), ou les problèmes d'hypertension) pourraient bénéficier d'une surveillance en continu et à distance. Une exigence essentielle pour les systèmes de télésurveillance est leur facilité d'utilisation. De plus, ces systèmes doivent être particulièrement bien intégrés afin que les patients puissent surveiller leurs signes vitaux au quotidien avec un minimum de désagréments.

Un grand nombre de paramètres vitaux peuvent être mesurés au thorax. Par exemple, les maladies cardiaques chroniques peuvent être évaluées par des mesures d'électrocardiogramme (ECG) à dérivations multiples. Des études ont aussi montré l'aptitude de la tomographie d'impédance électrique (TIE)—une modalité d'imagerie médicale sûre et peu coûteuse—à évaluer les signes vitaux de patients souffrant de BPCO, d'asthme et de mucoviscidose. La TIE a également montré son aptitude à évaluer des paramètres hémodynamiques tels que le débit cardiaque, la pression artérielle pulmonaire ou moyenne.

Un système permettant de surveiller les paramètres physiologiques d'un patient dans son environnement quotidien est souhaitable. Cette thèse décrit le développement d'un système capable de mesurer simultanément un ECG à dérivations multiples de haute qualité ainsi que plusieurs canaux de bioimpédance permettant d'effectuer une imagerie par TIE. Afin de faciliter son utilisation, les capteurs sont intégrés dans une veste et des électrodes sèches sont utilisées.

En premier lieu, une nouvelle architecture électrique composée de capteurs dits coopératifs est détaillée. Alors que les architectures ECG/TIE classiques utilisent des câbles (double) blindés ou multiconducteurs pour connecter leurs électrodes à un boîtier centralisé (menant à des systèmes trop encombrants pour être portables), l'architecture proposée réduit considérablement la complexité du câblage (ni blindage, ni câbles multiconducteurs) et élimine la nécessité du boîtier centralisé. Ceci conduisant, sans aucun impact sur la qualité des signaux, à des systèmes facilement intégrables.

Afin de démontrer la fiabilité d'une telle architecture, un système ECG à 12 dérivations basé sur les capteurs coopératifs a été réalisé. Le bruit crête à crête mesuré est d'environ 30 µV. De

plus, des mesures sur un volontaire sain ont montré que la qualité des signaux mesurés avec le système coopératif (utilisant des électrodes sèches) est équivalente à celle mesurée avec un dispositif médical de référence (utilisant des électrodes gel).

En étendant l'architecture coopérative à une mesure de bioimpédance multicanaux, un système portable et facile à utiliser permettant des mesures simultanées de signaux TIE et ECG a été réalisé. La structure TIE entièrement parallèle (c.à.d., tous les courants de mesure et toutes les tensions résultantes sont simultanément injectés et mesurées) permet d'éviter l'utilisation de multiplexeurs au moyen de plusieurs sources de courant et de plusieurs mesures de tension connectées en parallèle. Ceci permettant un choix flexible et ajustable des différentes configurations de stimulation et de mesure via une approche de multiplexage par répartition en fréquence. Les différentes sources de courant et mesures de tension ont été calibrées avec une précision de la mesure d'impédance de $\pm 0.67\%$ (mesuré sur une résistance de $150\,\Omega$). De plus, l'écart type du bruit mesuré sur cette même résistance est de $8.73\,\mathrm{m}\Omega$.

Finalement, une évaluation qualitative sur un volontaire sain a montré des résultats significatifs et prometteurs, ouvrant la voie à une nouvelle génération de systèmes non-invasifs, portables et faciles à utiliser pour une surveillance cardiovasculaire via des mesures ECG/TIE synchrone avec un nombre et un positionnement variable des électrodes.

Mots clefs : Capteurs portables, surveillance à distance des patients, électrocardiographie (ECG), dérivations multiples, ECG à 12 dérivations, biopotentiel, bioimpédance, tomographie d'impédance électrique (TIE), multiplexage par répartition en fréquence, calibration de circuit électronique, électrodes actives, capteurs cooperatifs, électrodes sèches, réseau de capteurs corporels.

Remerciements

Un travail de Doctorat c'est avant tout une question de recherche. Tout d'abord on recherche un sujet qui nous passionne, ensuite on recherche un problème plus précis qui mérite que l'on y investisse notre temps. Puis on recherche les inévitables financements, avant (et enfin...) de commencer à rechercher des solutions (si possible) innovantes. Et comme ces solutions ne sont ~~mal~~heureusement pas toujours évidentes, il va aussi falloir rechercher la motivation et la persévérance qui permettront de faire face aux obstacles qui se dresseront devant nous. Ces obstacles, je ne les ai fort heureusement pas affrontés seul. Par ces quelques lignes, je recherche à remercier les personnes qui m'ont aidé avec enthousiasme (et parfois même avec humour [71]) à les franchir.

Je tiens tout d'abord à remercier Olivier Chételat (superviseur de ma thèse au CSEM). Nos innombrables discussions (que ce soit au bureau ou en covoiturant), ses idées innovantes et sa vision du projet ont été une composante essentielle à l'élaboration de ce travail. Cette collaboration a été très agréable et enrichissante (personnellement et professionnellement), allant même jusqu'à l'apprentissage du maniement des baguettes coréennes!

Je remercie particulièrement Marc Correvon (alias "le Chef") qui a cru en moi dès le début en me proposant de relever ce défi. Etant encore un peu jeune et naïf (il y a un peu plus de 4 ans), je n'ai pas osé dire non à ce challenge qui m'apportera beaucoup. Je le remercie pour sa confiance et son soutient humain, toujours soucieux de s'assurer que ma motivation reste à son paroxysme.

Je tiens aussi à remercier Jess Snedeker de l'ETHZ pour avoir accepté de superviser ma thèse. Même si le sujet diffère quelque peu de son domaine d'expertise habituel, il a su me soutenir et m'aiguiller aux moments clés. Je tiens aussi à le remercier pour son enthousiasme et sa disponibilité à chaque fois que j'en ai eu besoin. Merci aussi à Walter Karlen d'avoir accepté de se porter membre du jury. Son regard d'expert et son avis critique m'ont permis d'évoluer et de mieux comprendre comment des personnes externes peuvent percevoir mon travail.

Je remercie aussi Josias Wacker pour avoir partagé sa vision du projet et pour m'avoir épaulé lors de la rédaction des articles scientifiques. En effet, au début de ma thèse, la rédaction d'articles scientifiques me paraissait être un art très abstrait (à l'image de l'EIT me diront certains...). Merci aussi pour les courses à Chaumont qui permettent de remettre les idées (et souvent le ciel) au clair.

Remerciements

Danke à Fabian Fabu Braun et obrigado au (already Dr.) Fribourgeois Martin Proença (avec la cédille), anciens doctorants EIT du CSEM, qui m'ont brillemment montré la route à suivre [15, 78]. Je les remercie aussi pour les nombreuses et intéressantes discussions, et pour m'avoir accompagné durant cette aventure EIT.

Je tiens aussi à remercier mes collègues, Christophe Meier, Jacques-André Porchet, Etienne Haenni, Abdessamad Falhi, Patrick Theurillat, Damien Ferrario et Pascal Liechti, qui ont partagé mes soucis. Je les remercie pour avoir été autant (voir même plus) coopératifs que les capteurs ! Merci aussi à Mathieu Lemay et Josep Solà pour m'avoir conseillé (respectivement guidé) en début de thèse, notamment pour la rédaction de mes premiers articles scientifiques.

Merci aussi à l'équipe du bureau technique (Monique Frosio, Roberto Rusconi, Antonio Moreira De Sousa, Pascal Pilloud et leur·e·s dévoué·e·s apprenti·e·s) que je suis venu em-BT régulièrement et qui m'ont apporté une précieuse aide lorsque mes compétences pratiques arrivaient à leurs limites théoriques.

Je remercie les experts que j'ai eu la chance de rencontrer dans le cadre du projet WELCOME. Tout particulièrement Inéz Frerichs et Andy Adler pour leur aide très appréciée, notamment pour la rédaction de mon dernier article.

Et même si un doctorat est (en partie) un don de sa personne (et de son temps) pour la science, je voulais aussi remercier ma famille et mes amis qui m'ont permis de garder un équilibre entre ma vie professionnelle et privée, paramètre indispensable à la réussite d'une telle épreuve (d'endurance). Un merci tout particulier à Eloïse, ma plus grande fan (*sic*), qui aura rendu la dernière période de ma thèse bien plus agréable que je n'aurai pu l'imaginer ($\frac{1}{3}E - M < 0$).

Corcelles-près-Payerne, le 22 août 2018   Michaël

Contents

Contents

List of Figures

List of Tables

List of Acronyms

ADC	Analog-to-digital converter
AP	Inspiratory apnea
ASIC	Application-specific integrated circuit
BAN	Body area network
BASN	Body area sensor network
BCC	Body coupled communication
BLE	Bluetooth low energy
BSN	Body sensor network
BT	Bluetooth
CHF	Congestive heart failure
COPD	Chronic obstructive pulmonary disease
CPLD	Complex programmable logic device
CT	Central terminal according to Wilson
DAC	Digital-to-analog converter
DB	Deep breathing
DC	Direct current
ECG	Electrocardiogram/-ph/-phy
EEG	Electroencephalogram/-ph/-phy
EIT	Electrical impedance tomography
EMG	Electromyogram/-ph/-phy
EOG	Electrooculogram/-ph/-phy
FDM	Frequency-division multiplexing
I^2C	Inter-integrated circuit
IEC	International electrotechnical commission
LA	Left arm
LL	Left leg
NB	Normal breathing
OA	Operational amplifier
PCB(s)	Printed circuit board(s)
PI	Proportional-integral
PLL	Pulse lock loop
RA	Right arm
RC	Resistance-capacitance

List of Acronyms

RL	Right leg
rms	Root mean square
SNR	Signal-to-noise ratio
SpO$_2$	Peripheral capillary oxygen saturation
std	Standard deviation
UGBW	Unit gain bandwidth
VCO	Voltage controlled oscillator
WHO	World health organization

1 Introduction

1.1 Motivation and Problem Statement

Chronic diseases, also known as noncommunicable diseases, are one of the major health challenges of the 21st century. The world has reached a decisive point in the history of chronic diseases and has an unprecedented opportunity to alter its course [105]. According to the World Health Organization (WHO), in 2012, out of the 38 million deaths due to chronic diseases, more than 40 % were affecting people under 70 years of age. The majority of these deaths are preventable.

The four main types of chronic diseases are cardiovascular diseases (like heart attacks and stroke), cancers, chronic respiratory diseases (such as asthma and chronic obstructive pulmonary disease, also abbreviated as COPD), and diabetes [105]. Among these four diseases, cardiovascular and chronic respiratory diseases are intimately related to the state of health of the heart and the lungs. To evaluate the state of health of these two vital organs, a large set of important parameters can be measured on the chest. For instance, chronic heart diseases can be evaluated via multilead electrocardiogram (ECG) measurements [9, 91]. Other studies show the ability of electrical impedance tomography (EIT)—a safe and low-cost medical imaging modality—to assess relevant vital signs for COPD [95, 96], asthma [32], or cystic fibrosis patients [55, 58, 114]. EIT has also shown the ability to assess hemodynamic signals, such as pulmonary blood pressure [79], mean arterial blood pressure [90], or stroke volume [15]. For these applications, a robust, continuous signal acquisition is required.

Telemonitoring of vital signs—which consists of a patient management approach combining various information and sensing technologies for remote monitoring [77]—enables novel clinical strategies [9]. Patients suffering from chronic diseases, such as congestive heart failure (CHF), COPD, or poorly controlled hypertension could benefit from remote continuous monitoring [18]. An essential requirement for telemonitoring systems is ease of use [26], particularly for elderly patients [30]. At the same time, telemonitoring systems need to be highly integrated so that patients can monitor their vital signs during their daily-life with minimal inconvenience.

Today, numerous smart garments measuring various physiological signals are available [75, 76, 98]. Compared to bedside monitors that allow measuring many parameters, the number of sensors and measured signals in wearable systems are today limited. One reason is the complex cabling of the sensors requiring insulated, (double) shielded cables, as well as bulky connectors. Most of these systems use an electrical architecture where sensors are connected in a star arrangement to a central unit. Such cabling is undesired but acceptable for bedside monitors, whereas it is unacceptable for wearables.

1.2   Objectives of the Thesis

An integrated system offering the possibility to closely monitor physiological parameters in a patient's everyday environment is desirable. The objective of this thesis is to study a novel wearable system able to simultaneously measure multilead ECG and multichannel bioimpedance for EIT imaging. To maximize its ease of use, the sensors are integrated in a vest and dry electrodes are used. This way, the monitored patient can simply put on the vest without other inconvenience (such as electrodes placement, skin preparation, or complex startup procedure).

This thesis introduces a novel sensing architecture so-called "cooperative sensors". Without any compromise on signal quality, the cabling complexity is significantly reduced. Sensors are connected in a bus arrangement via two unshielded wires, making the complexity of the electrical connection independent of the number of sensors. The design and evaluation of this wearable and easy-to-use system for fully-parallel EIT (meaning that all measuring currents and all resulting voltages are simultaneously injected and measured) and multilead ECG measurement is reported. The main novelties of the proposed system are: 1) the electrical architecture of the system allowing for a minimal wiring between sensors, 2) the simultaneous measurement of high-quality multilead ECG and multichannel bioimpedance for EIT imaging, and 3) the unswitched fully-parallel EIT measurement via frequency-division multiplexed current stimulations.

1.3   Thesis Contributions

In this thesis, the electrical architecture of the so-called cooperative-sensor system is defined. This new architecture significantly reduces the wiring complexity and eliminates the presence of the central electronic unit to which all cables classically converge. This results, without any impact on the signal quality, in systems which are easier to integrate in wearables.

To demonstrate the reliability of the proposed architecture, a wearable 12-lead ECG monitoring system, an ECG holter, was integrated in a vest and compared to a gold-standard medical device. This comparison showed that the signal quality measured with the cooperative-sensor system (using dry electrodes) is similar to the one measured with the gold-standard medical device (using gel electrodes).

A wearable and easy-to-use system for EIT and synchronous multilead ECG measurement was also designed. Measurements on a healthy volunteer showed promising and physiologically meaningful results, paving the way towards a new generation of wearable ECG/EIT systems for noninvasive cardiovascular monitoring.

1.4 Organization of the Manuscript

Chapter 2 (Background) describes the classical approaches to acquire biopotentials and bioimpedances, and explains why (double) shielded or multi-conductor cables are classically required to measure high-quality signals. Then, the concept of EIT is introduced, and classical hardware commonly used for EIT data acquisition is briefly reviewed.

Chapter 3 (Cooperative Sensors for ECG Measurement) introduces the electrical architecture of the cooperative sensors developed in the framework of this thesis. For the sake of simplification, this chapter focuses on the measurement of multilead ECG. The communication and synchronization circuits allowing cooperative sensors to work in concert are detailed. In order to assess the performance of the cooperative-sensor system, different test setups were implemented and the results of the tests are shown. A wearable 12-lead ECG monitoring system based on cooperative sensors was implemented, demonstrating the reliability of the proposed approach for wearable ECG monitoring in real-life scenario.

Chapter 4 (Cooperative Sensors for Synchronous ECG and EIT Measurement) demonstrates the feasibility of cooperative sensors for multichannel bioimpedance (i.e., EIT) and synchronous multilead ECG measurement. Based on the circuits presented in chapter 3, the extension of the cooperative-sensor architecture necessary for fully-parallel EIT with simultaneous current injections and parallel voltage measurements via frequency-division multiplexing is detailed. Testing procedures and results for EIT system calibration and noise performance assessment are presented. Finally, preliminary measurements on a healthy volunteer show the ability of the system to measure EIT data synchronously with multilead ECG. Lung-related and heartbeat-related EIT images were reconstructed, demonstrating the feasibility of the proposed approach for noninvasive cardiovascular monitoring.

Chapter 5 (Synthesis) concludes this dissertation by providing a synthesis, a discussion of the limitations of the proposed work, and suggestions for future studies.

2 Background

This chapter describes the approaches classically used to acquire biopotentials (section 2.1) and bioimpedances (section 2.2), and explains why shielded (coaxial) or double-shielded (triaxial) cables with passive electrodes, or multi-conductor cables with active electrodes, are required to acquire signals of high quality. Section 2.3 introduces the concept of electrical impedance tomography (EIT), and classical hardware for EIT data acquisition is briefly reviewed. The content presented in this chapter is adapted from the postprint version of [80].

2.1   Classical Circuits for ECG Measurement

This section starts by a short introduction into electrocardiogram (ECG), then classical circuits for biopotential measurement are presented. Although biopotentials could originate from different sources—such as the muscles (electromyogram, EMG), the brain (electroencephalogram, EEG), the eyes (electrooculogram, EOG)—this chapter focuses on ECG. By adapting the input referred noise and the frequency band of interest of the sensing electronics, any other biopotential would be measured in the same way.

2.1.1   ECG Basics

An ECG is a graphical recording of the electrical signal originating from the depolarization and repolarization of the cardiac muscle. The size and the shape of the ECG signal, as well as the time intervals between the various peaks, contain useful information about the nature of disease affecting the heart [1]. ECGs are classically measured on the body surface and the amplitude of the measured voltage is of the order of 1 mV [59]. Given the low amplitude of the signal, an amplification is necessary. To accurately amplify the ECG signal, the amplifier shall have good performances in respect of at least the following characteristics [43] :

- linearity
- absence of drift
- noise (interference) rejection
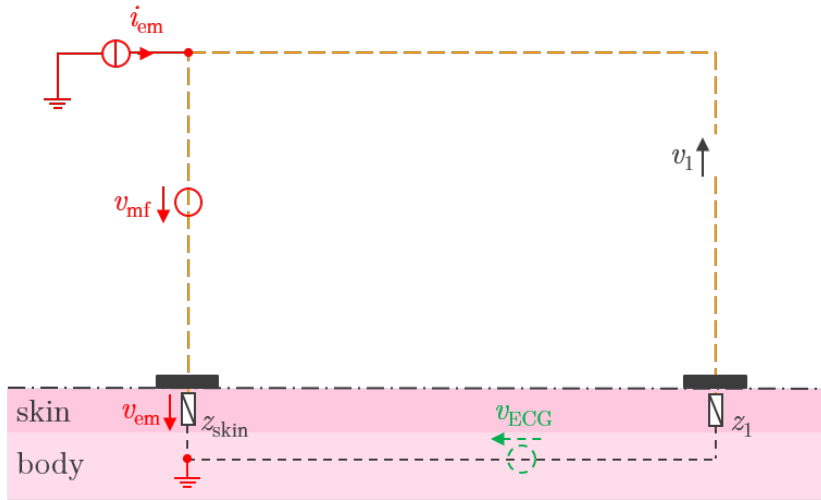
Figure 2.1 – Simplest circuit for ECG measurement. Here, v_{ECG} represents the ECG voltage, v_1 the measured voltage, i_{em} the current induced by electric-field variations, v_{em} the disturbance voltage resulting from the current i_{em} flowing toward the earth ground via the skin impedance z_{skin}, v_{mf} is the disturbance voltages induced by magnetic-field variations, and z_1 is the skin impedance beneath the branch used to measure v_1. Conductors sensitive to electromagnetic disturbances are marked with dashed orange lines.

The requirements of the recording system are formally collected in the international standards IEC 60601–2–25 [51] and IEC 60601–2–47 [52], and define for example the minimal input impedance of the sensing circuit, the maximal input-referred noise, and the signal bandwidth (typically from 0.05 Hz to 150 Hz for diagnostic ECG).

2.1.2 Simplest Circuit for ECG Measurement

The simplest circuit for ECG measurement is shown in figure 2.1. Basically, the ECG is modeled as a voltage source (v_{ECG}) located in the body, while series impedances (z_{skin} and z_1, also named skin impedances) model the impedances of the electrode-body interfaces. Other impedances, such as the impedance of the tissues inside the body or the impedance of the conductors, are negligible in this context. From this circuit, the ECG voltage v_{ECG} is directly measured as v_1.

In practice, the circuit of figure 2.1 performs poorly in presence of electromagnetic disturbance. For instance, according to Faraday's law of induction, magnetic-field variations result in a disturbance voltage in series with the ECG voltage (see v_{mf} in figure 2.1). Such disturbance may originate from the mains, typically at 50 or 60 Hz (or 16⅔ Hz for some railway lines). Motion in a constant magnetic field, such as the natural earth magnetic field, also induces a disturbance voltage. To reduce the effects resulting from magnetic-field variations, the loop area limited by the dashed orange lines and the skin should be minimized [49, 100]. Therefore, the wires connecting the electrodes shall be as short as possible and, consequently, close to the skin.

The most important source of electromagnetic noise is generally due to electric-field variations which can be modeled by a current source injecting a current into the exposed conductor (see i_{em} in figure 2.1, dashed orange lines represent exposed conductors). When the current i_{em} is injected at any point of the exposed lines, a part of it may cross the skin impedances (z_{skin} or z_1). As these impedances are relatively large, this can lead to a significant voltage in series with the ECG voltage (v_{ECG}) which directly affects the ECG measured as v_1. In general, the body is floating (or capacitively coupled) regarding to the earth ground. However, in the context of cooperative sensors, the voltage on the parasitic capacitance between the body and the earth ground has a limited impact since the the sensors are also floating regarding to the earth ground. The body is thus represented as grounded in the figures of this thesis.

2.1.3 Guard Electrode and Common-Mode Rejection

Figure 2.2 shows the classical approach used to solve the problem due to the disturbance current i_{em}. This new configuration includes an additional voltage-sensing branch to measure v_0. This branch is parallel to the one used to measure the voltage v_1 and is connected to the so-called reference wire (ref. wire). The ECG is obtained by measuring the voltage difference $v_1 - v_0$. That way, a large section of the circuit (i.e., the ref. wire) is insensitive to electric-field disturbances. Indeed, any disturbance current i_{em} injected at any point of the ref. wire flows across the impedance z_{guard} under the guard electrode. The induced disturbance voltage v_{guard} is identically measured by both v_0 and v_1. With this configuration, additional ECG leads can be obtained by simply adding replicates of the branch used to measure v_1.

The disturbance voltage v_{guard} however affects the measured common-mode voltage which is defined as $(v_0 + v_1)/2$—or as $(v_0 + v_1 + \cdots + v_N)/(N+1)$ for $N+1$ measured voltages. Depending on the common-mode rejection ratio (CMRR) of the amplifier circuits used to measure v_0 to v_N, the differences (i.e., the measured ECG leads) may still be affected by the common-mode voltage. Moreover, this common-mode voltage may also induce a saturation of the circuits used to amplify the measured voltages v_0 to v_N. The classical approach used to solve this issue is to control the common-mode to zero via the controller H and the controlled voltage source v_{cm} (see figure 2.2).

It has to be noted that any current injected in the section of the circuit that is marked in dashed orange (in figure 2.2) will still generate a voltage disturbance on v_0 and/or v_1, and therefore affect the measured ECG voltage.

2.1.4 Shielded Cables for High-Quality ECG Measurement

To further reduce the sensitivity to noise of the circuit shown in figure 2.2, shielded cables are used, leading to the classical circuit for ECG measurement shown in figure 2.3. Besides the guard electrode and the common-mode controller H, shielded cables are used to connect the passive electrodes to the central unit which contains all electronic circuits required for the
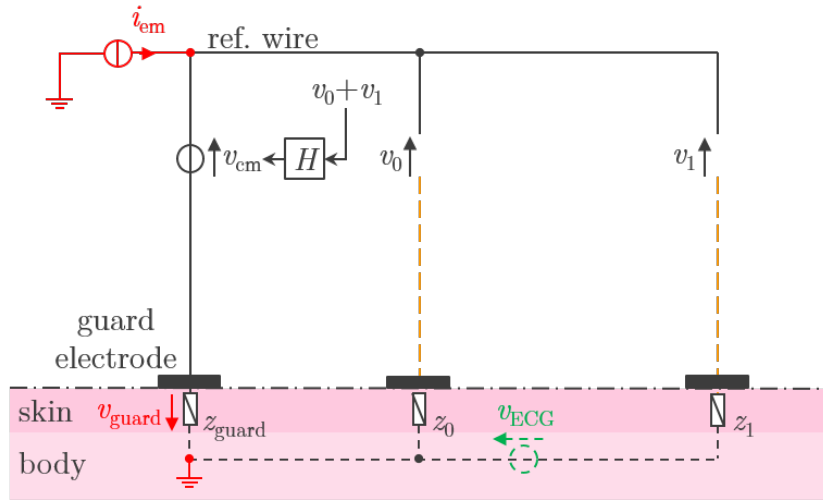
Figure 2.2 – Circuit for ECG measurement with a common-mode voltage controller. The controller H controls the common-mode voltage to zero via the voltage source v_{cm}. The voltage v_{guard} induced by the disturbance current i_{em} is readily compensated by v_{cm}. The impedances z_0 and z_1 are the skin impedances beneath the branches used to measure v_0 and v_1, respectively. The ECG voltage v_{ECG} is obtained by measuring the difference between v_0 and v_1. The ref. wire serves as a common analog reference potential to all measured voltages. Conductors sensitive to electromagnetic disturbances are marked with dashed orange lines.

measurement. One shielded cable is used per ECG lead [94], and optionally one for the guard electrode (the guard electrode is not shielded in figure 2.3). These shields are driven with the same potentials as the ones measured on the cable cores to guarantee high input impedances, which is—as described in the next subsection—essential to ensure a high ECG signal quality.

2.1.5 Analog Frontend Properties for High-Quality ECG Measurement

In practice, a low bias current of the analog frontend used to sense v_0 to v_N is required to guarantee a high-quality ECG measurement. Indeed, as a first approximation the voltages on the skin impedances z_0 to z_N (see figure 2.3) are equal to zero since the currents in the voltage-sensing branches are considered as null. However, actual analog frontends have bias currents flowing through these skin impedances that may induce a significant signal on the voltages measured as v_0 to v_N. Consequently, any changes in the skin impedance values, for instance due to the motion on the electrode-body interface, may generate artifacts on the measured voltages [115]. For this reason, it is important to minimize both the skin impedance and the bias current of the analog frontends.

Another issue related to the sensing circuits is the voltage divider embodied by the skin impedance and the input impedance of the voltage-sensing analog frontend [27] which atten-
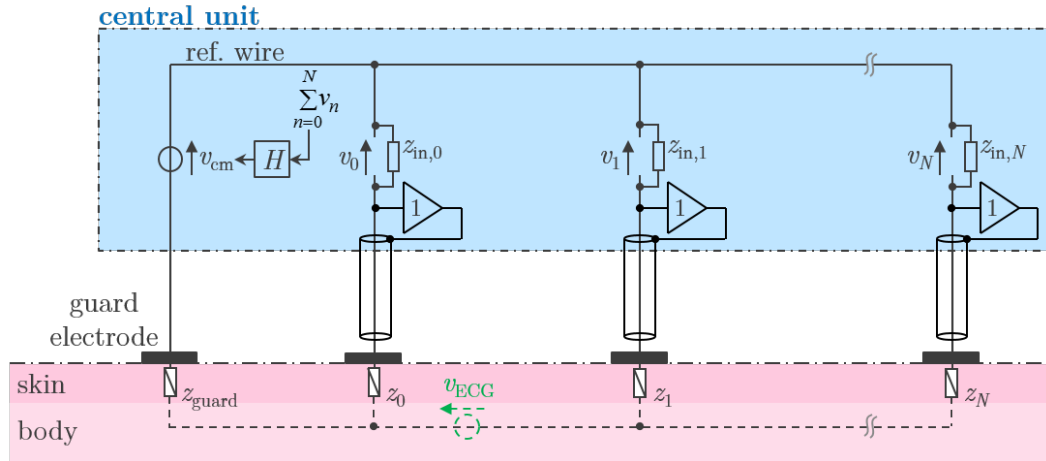
Figure 2.3 – Classical circuit for multilead ECG measurement with a central unit and shielded cables. The ECG leads are obtained via linear combinations of the voltages measured as v_0 to v_N. The input impedances of the analog frontends used to measure v_0 to v_N are modeled as $z_{\text{in},0}$ to $z_{\text{in},N}$, respectively.

uates the measured ECG signal according to equation 2.1:

$$v_n = v_{\text{ECG},n} \frac{z_{\text{in},n}}{z_{\text{in},n} + z_n} \tag{2.1}$$

where v_n and $v_{\text{ECG},n}$ are the voltages measured and seen by the nth measurement branch, respectively (with $n \in \{0, \ldots, N\}$). The impedance $z_{\text{in},n}$ is the input impedance of the analog frontend of the nth branch, and z_n its corresponding skin impedance. For this reason, it is important to maximize the input impedance of the analog frontends, and also to minimize the skin impedance.

2.1.6   Examples of Classical Instrumentation for ECG Measurement

As shown in figure 2.3, classical approaches to measure a multilead ECG classically require the use of a central electronic unit to which all cables converge. Moreover, disposable adhesive gel electrodes are usually affixed on specific body locations and cables linking these electrodes to the central unit must be shielded to guarantee high-quality ECG measurement. With classical approaches, increasing the number of ECG leads increases the number of cables converging to the central unit. Consequently, for a large number of leads, the size of the central unit might be limited by the size of the cables and connectors. Figure 2.4 (left) illustrates this classical star architecture, and figure 2.4 (center and right) show two examples of commercial devices implementing electronic circuits for a classical 12-lead ECG Holter. This figure underlines that connectors and cables take an important place in the device and that the cabling is a
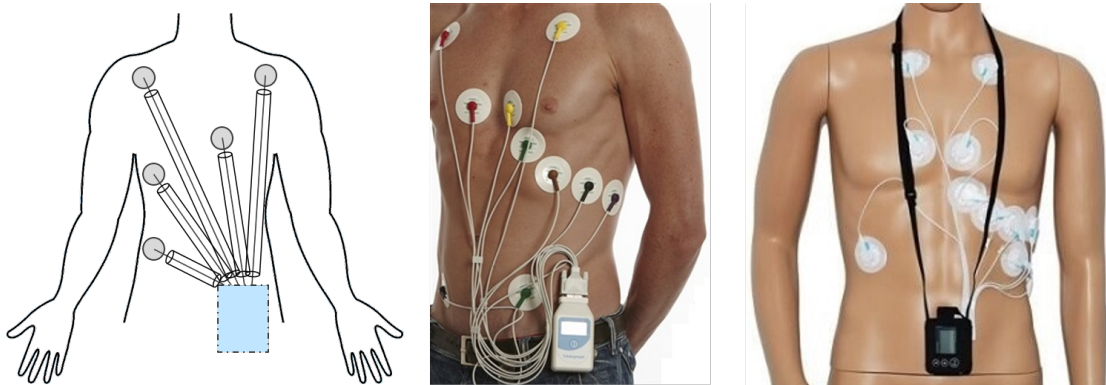
Figure 2.4 – Classical instrumentation for multilead ECG measurement with a central unit and shielded cables. Left: illustration of the classical star architecture; Center: 12-lead ECG Holter, Spirotrac ECG (Vitalograph, Buckingham, England); Right: 12-lead ECG Holter, iTengo+ (Borsam, Shenzhen, China).

limitation in the integration of tomorrow's wearables. It has to be noted that both systems use adhesive gel electrodes which are known to provide low skin impedance (and thus potentially better signal quality). However they are irritating for long-term use [13, 60, 69], and can also detach [112] or dry out.

2.2   Classical Circuits for Bioimpedance Measurement

This section starts with a short introduction about bioimpedance, then classical circuits for multichannel bioimpedance measurement are presented.

2.2.1   Bioimpedance Basics

Bioimpedance refers to the electrical properties of a biological tissue measured when a current flows through it [46]. On a cellular level, bioimpedance can be modeled as presented in figure 2.5 (left). The extracellular space is represented as the resistance R_e, whereas the intracellular space is represented as the resistance R_i, and the membrane as the resistance R_m in parallel to the capacitance C_m. Both intracellular and extracellular spaces are highly conductive, because they contain dissolved salt ions [46]. However, the cell membrane has a low conductivity due to its lipid bilayer [11]. Figure 2.5 (right) shows a first approximation of the cell equivalent circuit [11, 46].

As shown in figure 2.6, the path taken by the current depends on its frequency. Low-frequency currents hardly penetrate the cells, as their membranes are mostly capacitive [10]. The currents thus primarily travel through the extracellular space. At higher frequencies, however, the currents can cross the capacitance C_m and also flow through the intracellular space [46].

A closer look at the equivalent circuit of figure 2.5 (right) shows that the bioimpedance value is

Figure 2.5 – First approximation of the electrical model of a cell (adapted from [78]). C_m: membrane capacitance; R_m: membrane resistance; R_i: intracellular fluid resistance; R_e: extracellular fluid resistance; C_m^*, R_i^*, and R_e^*: capacitance and resistances of the equivalent circuit.
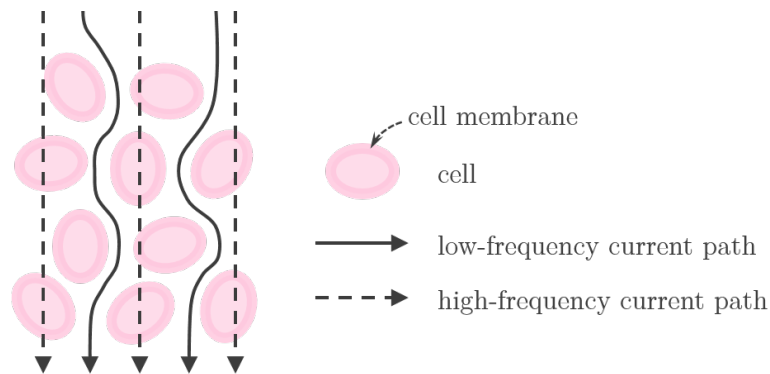
Figure 2.6 – Path of the electrical current through the cells for both low and high frequencies (adapted from [46]).

approximately equal to R_e^* at low frequencies, and to R_e^* in parallel to R_i^* at high frequencies. In between, the bioimpedance value is complex and its imaginary part (reactance) negative due to the capacitive property of bioimpedance. This aspect is illustrated with a semi-circular curve in the Cole-Cole plot of figure 2.7. In practice, the center of this semi-circular curve is shifted downward due to the heterogeneity of the measured tissue [24].
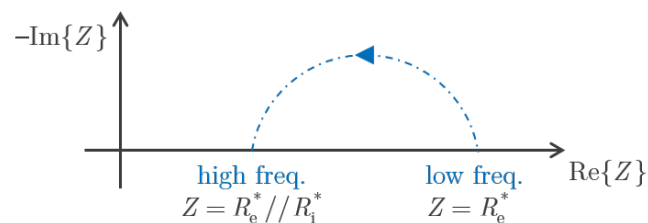
Figure 2.7 – Cole-Cole plot of the cell electrical model. The bioimpedance Z varies from R_e^* (low frequencies) to R_e^* in parallel to R_i^* (high frequencies).
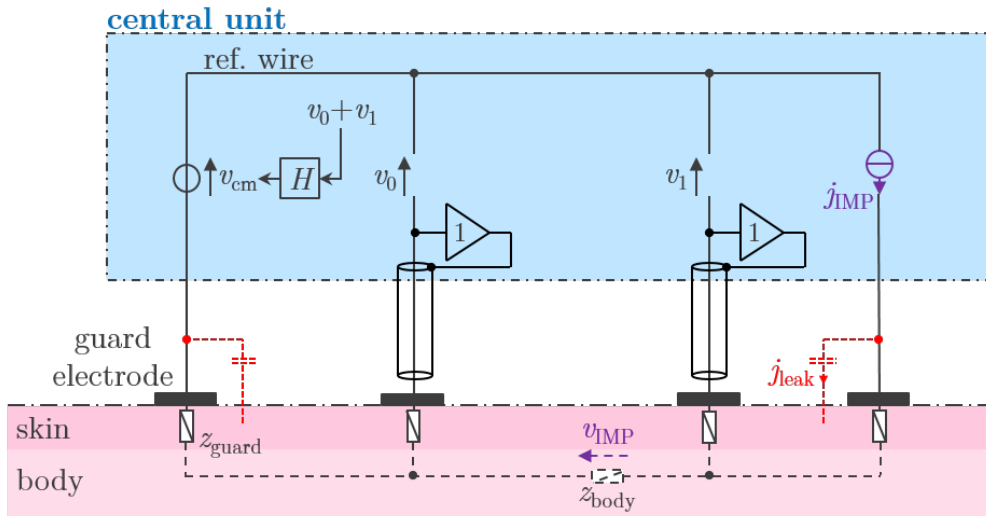
Figure 2.8 – Simple circuit for tetrapolar bioimpedance measurement. The measurement current j_{IMP} is injected in the body and the resulting voltage v_{IMP} on the bioimpedance z_{body} is measured via the difference between voltages v_1 and v_0. The leakage current j_{leak} is due to the capacitive coupling between the cables and the body.

2.2.2 Simple Circuit for Tetrapolar Bioimpedance Measurement

A simple circuit for tetrapolar bioimpedance measurement (meaning that different electrodes are used for current injection and voltage measurement) is shown in figure 2.8. This circuit is similar to the one presented in figure 2.3 for classical ECG measurement, however it is limited to the measurement of two biopotentials (v_0 and v_1), and an additional branch is used to inject the current j_{IMP}. With this configuration, the j_{IMP} current loop is closed via the guard electrode and the ref. wire. Although not ideal, the tetrapolar method reduces the influence of the skin impedances on the bioimpedance measurement [8, 38]. After discussing the problem of leakage currents (see subsection 2.2.3), subsection 2.2.4 describes the influence of the surface skin impedance on the tetrapolar bioimpedance measurement.

2.2.3 High-Quality Bioimpedance Measurement with Double-Shielded Cables

In practice, the circuit of figure 2.8 has the problem of leakage currents along the wire that conveys j_{IMP} from the current source to the electrode. The same applies for the cable connecting the guard electrode. A part of this leakage current (j_{leak}) is due to the capacitive coupling between the cables and the body [46] (as illustrated in dashed red in figure 2.8). Other capacitive couplings are also possible with other cables or with the central unit. To solve this issue, the current-injecting cables must be shielded and the potential of the shield must follow the cable-core potential as shown in figure 2.9.

The driven shields allow the cables to entirely convey the currents originating from the cur-
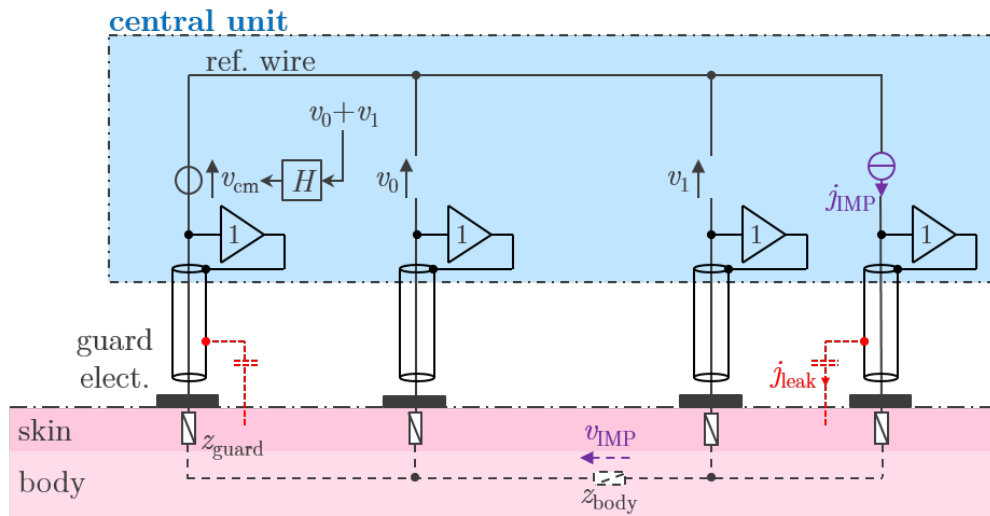
Figure 2.9 – Circuit for tetrapolar bioimpedance measurement comprising shielded cables. The leakage current j_{leak} is due to the capacitive coupling between the cable shields and the body.

rent sources to their respective electrodes. However the same currents as in the unshielded situation (j_{leak}) is still injected in the body since the shield has the same potential as the cable core. To avoid any current leaking in the body—which would induce undesired voltages drops on the measured bioimpedances—a second shield with a constant potential is used [25, 42]. The reciprocity theorem states that the same value is obtained if one makes a measurement with permuted cables [44, 64], i.e. connecting the cables normally used for current injection for voltage measurement, and the ones normally used for voltage measurement for current injection. Therefore, the cables used for voltage measurement must be double-shielded as well.

Figure 2.10 shows the final circuit with double-shielded cables allowing for high-quality bioimpedance measurement. This double-shielded approach is in line with bioimpedance measurement systems described in the literature [65, 70, 102]. Depending on the system requirements, unshielded cables may be used instead of thick and heavy triaxial cables. However it reduces performance to some extent [73]. The fully-parallel architecture shown in figure 2.10 allows adding an arbitrary number of voltage-sensing branches (such as the one used to measure v_1) and current-injection branches (such as the one used to inject j_{N+1}) to perform measurements with different tetrapolar configurations. The voltage-sensing branches are numbered from 0 to N and current-injection branches are numbered from $N+1$ to $N+M$.

It has to be noted that the more the skin impedance values are high (e.g., when dry electrodes are used), the more the double shielding is important [74]. Indeed, a measuring current j_{IMP} flowing through a high skin impedance induces a higher voltage variations on the cable that convey the current to the electrodes, and thus a potentially higher leakage current j_{leak}.
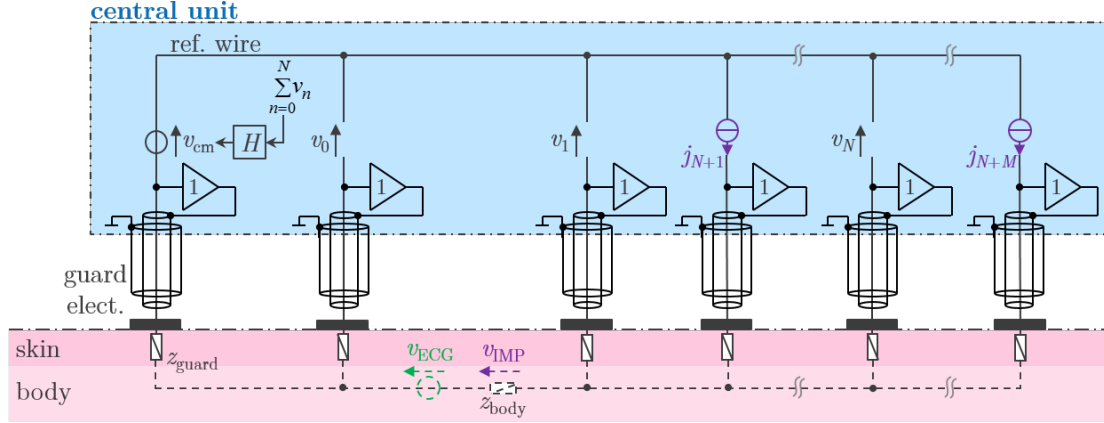
Figure 2.10 – Classical circuit for multichannel bioimpedance measurement of high quality with $N+1$ voltage-sensing branches (corresponding to the measured voltages v_0 to v_N) and M current-injection branches (corresponding to the injected currents j_{N+1} to j_{N+M}).

Although the circuit of figure 2.10 is presented for bioimpedance measurement only, the measured voltages (v_0 to v_N) can be used to simultaneously measure both ECG and bioimpedance. In this case, a clear separation between ECG and bioimpedance bandwidths must be guaranteed. Since the ECG frequencies hardly exceed 150 Hz [43, 51], the bioimpedance can be measured at higher frequencies (e.g., 50 kHz). This way, the bioimpedance circuit will not interfere with the ECG circuit.

2.2.4 Effect of the Surface Skin Impedance on the Bioimpedance Measurement

Even with the tetrapolar measurement technique, the bioimpedance measurement can be impacted by the impedance of the skin. Indeed, and as shown in figure 2.11, a part of the injected current j_m can flow via the impedance at the surface of the skin z_{surf} and the skin impedance z_{skin} under the voltage-sensing branch. Assuming that both skin impedances (z_{skin}) have approximately the same value, the current j_m induces an undesired voltage v_{skin} which is measured as v_n according to equation 2.2:

$$v_{\text{skin}} = j_m \frac{z_{\text{skin}}^2}{2z_{\text{skin}} + z_{\text{surf}}} \tag{2.2}$$

This equation shows that the effect of the tetrapolar bioimpedance measurement can be impacted if the impedance at the surface of the skin z_{surf} is small compared to z_{skin} (for instance while sweating).
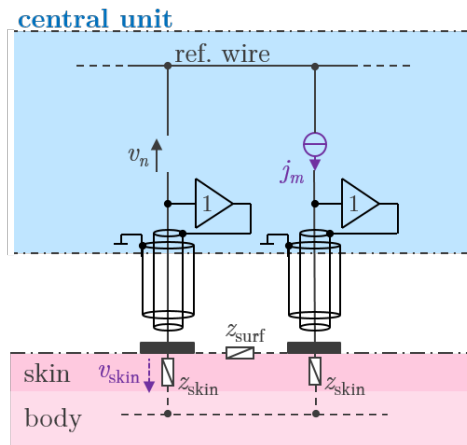
Figure 2.11 – Effect of the surface skin impedance on the bioimpedance measurement. Here, z_{skin} represent the skin impedances and z_{surf} the impedance at the surface of the skin between the two electrodes. The residual voltage measured by v_n is represented as v_{skin}.

2.2.5 High-Quality Bioimpedance Measurement with Active Electrodes

Figure 2.12 shows a first alternative to double-shielded cables which uses active electrodes and two-conductor cables. With this minimum number of conductors of two, one assumes that each active electrode has its own power supply. Otherwise, additional conductors are required. With this configuration, multi-conductor cables are connected to the central unit in a star arrangement, consequently, for a large number of leads, the size of the central unit might still be limited by the size of the cables and connectors.
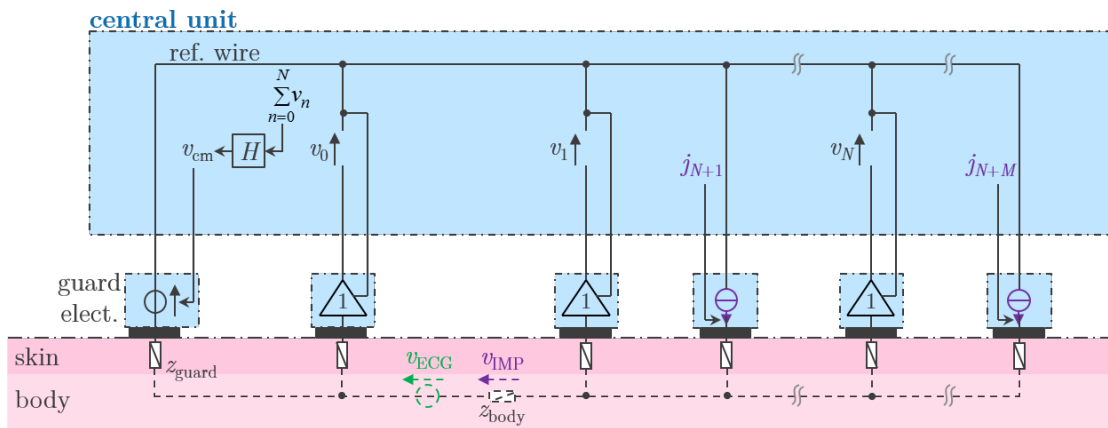
Figure 2.12 – Classical circuit for multichannel bioimpedance measurement using active electrodes and multi-conductor cables connected to the central unit in a star arrangement.

Another alternative for biopotential measurement was proposed by Degen *et al.* [28]. This approach uses a two-wire active buffer electrode that improves the immunity against power line interferences. By using a single transistor instead of the operational amplifier classically

used in buffer electrodes, this technique avoid the need of local power supply. The central unit to which all cables converge is, however, still required.

2.3   Classical Instrumentation for EIT Measurement

This section starts by introducing the concept of electrical impedance tomography (EIT), then classical hardware for EIT data acquisition is briefly reviewed.

2.3.1   EIT Basics

EIT is a non-invasive and low-cost medical imaging modality in which bioimpedance measurements are used to reconstruct images of the tissue impedance distribution [2, 46]. EIT is commonly used to monitor lung function [6], especially to prevent injury of mechanically ventilated patients [33, 104], or to assess other lung-related physiological parameters such as extravascular lung water [93]. Apart from ventilation, several studies have shown the feasibility of EIT to assess hemodynamics, such as systemic [90] and pulmonary [79] blood pressure, stroke volume [15, 97], or pulmonary perfusion [14, 72].

EIT systems are classically made of a belt of 16 to 32 electrodes distributed equidistantly on one transverse plane of the thorax. Stimulation currents are sequentially injected through the body between two of these electrodes, and the resulting voltages are measured between the other electrodes [12]. The electrodes used for current injection are called stimulation electrodes, whereas the others are called measurement electrodes. The combinations of electrodes chosen to inject stimulation currents and to measure the resulting voltages are known as stimulation and measurement patterns, respectively. Figure 2.13 (left) shows the first step of a typical pattern ("adjacent pattern") where a current j_{IMP} is injected between the first pair of electrodes ($\{1, 2\}$) and the resulting voltages (v_1 to v_{13}) are measured between the remaining pairs ($\{3, 4\}, \{4, 5\}, \ldots, \{15, 16\}$). The same process is repeated 16 times until each adjacent pair has been used as injecting pair. The second measurement step is represented in figure 2.13 (right) [78].

Due to the high impedance of the skin, stimulation electrodes are usually not used for voltage measurement, leading to a total of 13 measured voltages per injected current for a 16-electrode belt. The overall number of measurements N_{M} depends on the amount of electrodes N_{E} and is $N_{\mathrm{E}}(N_{\mathrm{E}} - 3)$, leading to a total of 208 measurements for $N_{\mathrm{E}} = 16$. However, the reciprocity theorem states that the same value is obtained if one makes a measurement with permuted pairs of electrodes [64], consequently, the maximum number of independent measurements becomes $\frac{1}{2} N_{\mathrm{E}}(N_{\mathrm{E}} - 1)$ [2], leading to a total of 120 independent measurements.

The electronic architecture of classical EIT systems usually uses cables to connect passive electrodes to a central unit in a star arrangement. With this configuration, high-quality measurement can only be obtained with double-shielded cables when passive electrodes are
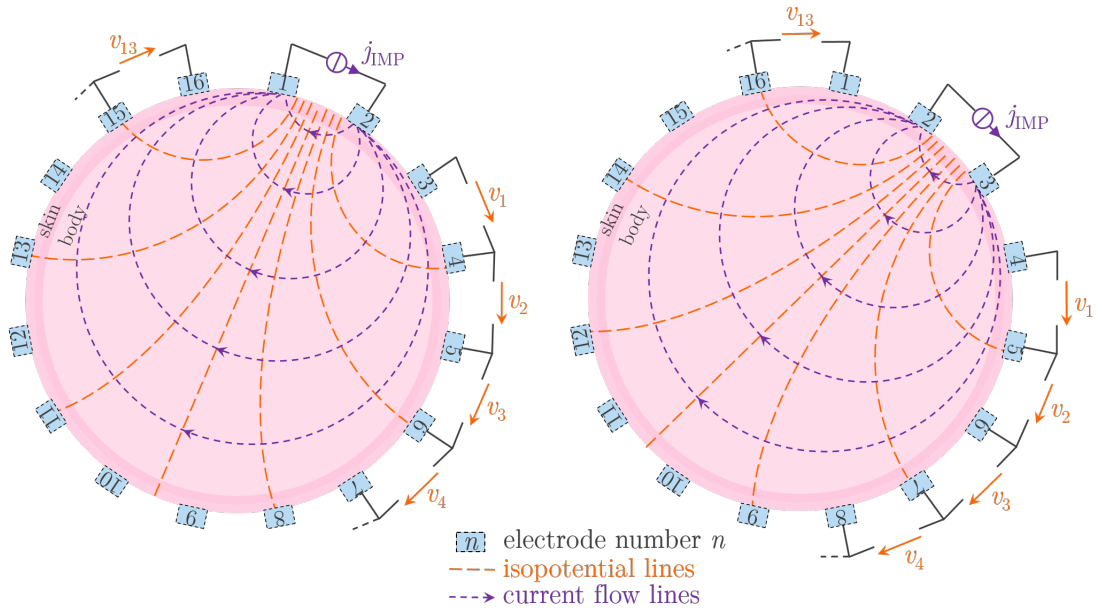
Figure 2.13 – Adjacent stimulation and measurement patterns: example for a 16-electrode configuration. Left: The stimulation current j_{IMP} is injected on the first pair of adjacent electrodes ($\{1, 2\}$) and the resulting voltages (v_1 to v_{13}) are measured on the remaining pairs ($\{3, 4\}, \{4, 5\}, \ldots, \{15, 16\}$). Right: The same process is repeated until each adjacent pair has been used as injecting pair. Adapted from [78].

used (see subsection 2.2.3), or with multi-conductor cables for active electrodes (see subsection 2.2.5). Consequently, increasing the number of electrodes increases cabling and connector complexity to the central unit, leading to EIT systems too bulky for wearables. The next section is a short review of instrumentation classically used for multichannel bioimpedance measurement in the context of EIT.

2.3.2 Overview of Classical EIT Instrumentation Systems

Many EIT instrumentation systems have been developed [46]. The most common approaches use a single current source and a single voltage measurement with analog multiplexing to sequentially select the stimulation and measurement electrodes [7, 35, 37, 47, 48, 54, 56, 63, 66, 116]. Though this approach reduces the hardware required, the imaging scan rate is limited, and the measurement performance is lower [2, 35, 65]. One reason is that all data are not acquired at the exact same time, which can impact the validity of reconstructions [109, 110]. Furthermore, analog multiplexers have undesirable effects due to parasitic input/output capacitances and limited on/off resistances of the switches [67, 88].

These limitations can be addressed by using frequency-division multiplexing, which allows for a simultaneous and continuous measurement of all EIT channels. Of course, frequency-

division multiplexing requires a fully-parallel EIT system with multiple current sources and voltage measurements. Parallel EIT instrumentations have already been developed [25, 40, 63, 73, 92, 102], but previous systems have used switched current sources. Moreover, none of these systems have been designed to be wearable.

In opposition to the classical star architecture, Gaggero *et al.* [35] showed an innovative way to address the current source and voltage measurement multiplexing, using daisy-chained active electrodes placed in a bus configuration, making the requirement for shielded cables unnecessary thanks to analog frontend buffers. However, they still use time multiplexing and the high number of wires required for the bus limits system integration.

Another important property of EIT systems is demodulation. EIT systems typically use current sources working in the range of tens to hundreds of kilohertz, and demodulate the measured voltages at this same frequency to measure the bioimpedance. Demodulation has been performed after [35, 56], or before [47] the analog-to-digital conversion. The latter requires more electronic circuits, but has the advantage of shifting the signal to lower frequencies, which reduces the analog-to-digital converter (ADC) sampling rate, which in turn reduces the data rate and the power consumption [47], both are critical parameters for wearable EIT systems.

Hong *et al.* [47] used this low-power demodulation approach and proposed an integrated circuit for portable lung-ventilation EIT system. This system uses a central unit to which all passive electrodes are connected. However, the use of unshielded cables in this configuration is prone to electromagnetic disturbances and crosstalk between the EIT channels, especially if dry electrodes are used.

The feature of synchronous acquisition of EIT and ECG data was offered already by the first commercially available EIT system, the Sheffield Mk 1 device [17]. It allowed a single lead ECG input that could be used for gated sampling of EIT data [31] but no multilead ECG. More recently, Guermandi *et al.* [39] developed an integrated circuit comprising the analog frontend for biopotential (in this application, the EEG) and EIT acquisition. This system uses active electrodes connected to a central unit via multi-conductor cables.

The limitations of the state of the art (e.g., the central electronic unit, double-shielded cables, time-multiplexing of the EIT currents, synchronous ECG acquisition) related to the integration of EIT and ECG in wearables can be reduced by using the cooperative-sensor architecture proposed in this thesis. The next chapter introduces this new architecture in the context of multilead ECG, whereas chapter 4 demonstrates its applicability for multichannel bioimpedance measurement in the context of EIT.

3 Cooperative Sensors for ECG Measurement

This chapter introduces the cooperative-sensor architecture developed in the frame of this thesis. For the sake of simplification, this chapter focuses on the measurement of ECG. Of course, any other biopotential can be measured with the same architecture. Moreover, a similar architecture can also be used for bioimpedance measurement (see chapter 4). Section 3.1 presents the concept of cooperative sensors and explains how this new electrical architecture differs from classical approaches used for ECG measurement. Section 3.2 details the communication and synchronization circuits allowing for cooperative sensors to work in concert. Section 3.3 shows the implementation of cooperative sensors in a wearable 12-lead ECG monitoring system. To assess the performance of the system and to demonstrate its reliability in real-life scenarios (at rest and during exercise stress test), different test setups were devised. Sections 3.4 and 3.5 show the testing hardware, procedures, and results. Finally, section 3.6 is a short discussion about the cooperative-sensor architecture. The content of this chapter is adapted from the postprint versions of [81] and [83].

3.1 From the Classical ECG Circuit to the Cooperative-Sensor Architecture

As detailed in the previous chapter (see section 2.1), the classical approach to measure ECG addresses electromagnetic disturbances either with carefully shielded cables connecting passive electrodes, or multi-conductor cables and active electrodes. Both approaches require a central electronic unit to which all cables converge. For a large number of leads, the miniaturization of the central unit is limited by the physical size of the cables and connectors. The classical circuit for multilead ECG measurement was shown in figure 2.3.

The cooperative-sensor architecture introduced in this section keeps the same underlying electrical architecture but the central unit is removed and the electronic circuits are placed directly onto the skin. The length of cables sensitive to electric-field disturbance is thus reduced to its minimum. The new circuit is composed of one master sensor (shown in the left of figure 3.1), and at least one voltage-measurement sensor (called type V sensors and
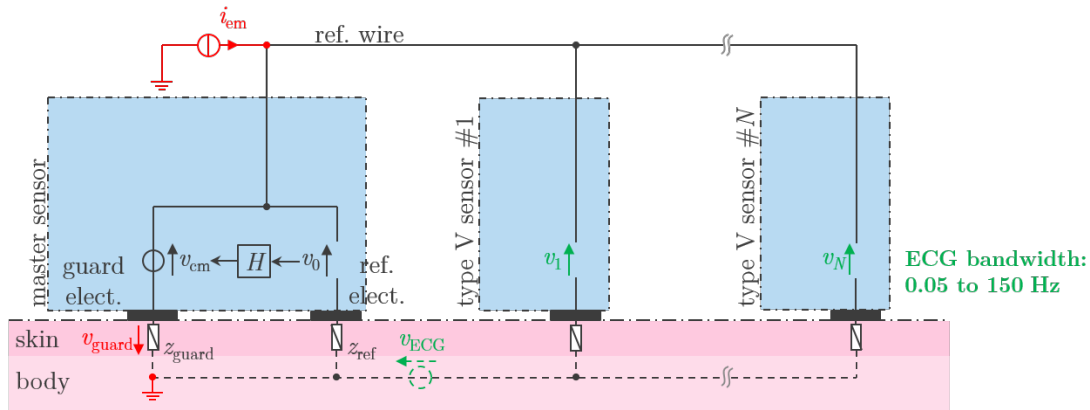
Figure 3.1 – Simplest circuit for multilead ECG measurement with cooperative sensors. The common-mode controller H is implemented in the master sensor and controls the voltage v_0 to zero via the voltage source v_{cm} to compensate for the voltage v_{guard} induced by the disturbance current i_{em} flowing through the skin impedance z_{guard}. The ECG voltages are measured as v_1 to v_N in each type V sensor.

shown in the middle and right of figure 3.1). All sensors are linked together with a unique external electrical connection called reference wire (ref. wire) which serves as a common analog reference potential to all sensors. Any sensor-site specific potential on the skin is therefore measured with respect to the ref. wire potential. The voltages v_1 to v_N are amplified, filtered, and digitized onsite by the electronic circuit embedded in each type V sensor.

The sensors are defined as cooperative in the sense that at least two independent sensors working in concert are required to measure a physiological signal (in this context, the ECG). In an etymological point of view, it means that the sensors must co– (i.e., together) –operate (i.e., perform a work or labor) to measure the targeted physiological signal.

A closer look at the circuit of figure 3.1 reveals that the condition of zero common mode is sufficient but not necessary (as a reminder, in figure 2.3, the sum of all measured voltages v_0 to v_N was used as an input by the common-mode controller H). Indeed, if one controls only the voltage v_0 to zero, the common mode is not exactly zero, but is proportional to the measured signal (i.e., the ECG signal). Consequently, it does not adversely affect the result. Such property allows feeding the controller H only with the measured voltage v_0. The advantage is that v_0 is readily available in the master sensor. Moreover, with v_0 controlled to zero, the potential of the ref. wire is close to the one in the body under the ref. electrode, consequently the ref. wire does not need to be insulated since the high impedance of the skin plays the role of insulation.

As the ref. wire is exposed to electromagnetic disturbance, a disturbance current i_{em} flows from this exposed wire to the earth ground via the skin impedance z_{guard} (which is seen as the only low-impedance path to the earth ground). The induced disturbance voltage v_{guard} is rejected by the controller H via the voltage v_{cm}. The specific architecture of the master sensor gives thus a low impedance path for the disturbance current i_{em}. Consequently, the ref. wire

does not need to be shielded to obtain high-quality ECG measurement.

With the architecture shown in figure 3.1, the cooperative sensors are placed in a bus arrangement and each sensor has only one connection with the ref. wire. Therefore, the number of leads no longer limits the sensor miniaturization. The price to pay for this reduction of the cabling and connecting complexity is that one power supply per sensor is now required. Moreover, to measure multilead ECG, at least two independent sensors working in concert are required, meaning that the sensors are cooperative and need to able to synchronously exchange information. The next section starts by showing a preliminary evaluation of classical body communication approaches in the context of cooperative sensors. Then, the extended cooperative-sensor architecture, including communication and synchronization, is detailed.

3.2 Communication and Synchronization in Cooperative-Sensor Systems

3.2.1 Overview of Classical Body Sensor Networks

Many body coupled communication (BCC) systems, wired, semi-wired, or wireless body sensor networks (BSN)—also called body area networks (BAN) or body area sensor networks (BASN)—have been reviewed in literature [22, 35, 41, 57, 68, 76, 89, 99, 106, 107, 108].

Even though wireless solutions have the advantage of not requiring any additional wire or electrical connection between the sensors, they are problematic in terms of power consumption, privacy, or interference with other wireless devices. Furthermore, biological tissues attenuate communication signals sent by sensors located on opposite side of the body, which is a limitation, especially in an open environment.

Xu *et al.* [106] and Yang *et al.* [108] developed active electrodes for multilead ECG measurement. Their active electrodes are linked together with a multi-conductor cable in a bus configuration. In both systems, the active electrodes are supplied via the multi-conductor cable and an I^2C interface is used to minimize the number of additional conductors for bidirectional communication between the active electrodes. An additional wire is required for measuring the ECG. Both systems use a five-conductor cable to connect all active electrodes.

Mercier and Chandrakasan [68] presented a two-wire BAN that communicates over electronic textile. The two wires are simultaneously used to supply sensors with power and for bidirectional communication. Even though this design only uses two wires, they are not used to set the potential reference for ECG measurement.

The BSN proposed in the next subsection is inspired by the classical wired communication bus. However, it is applied in the context of cooperative sensors and communicates through the same wire used for ECG measurement (i.e., the ref. wire) to reduce the cabling complexity. Only one additional wire in parallel to the ref. wire is required to allow full-duplex communication
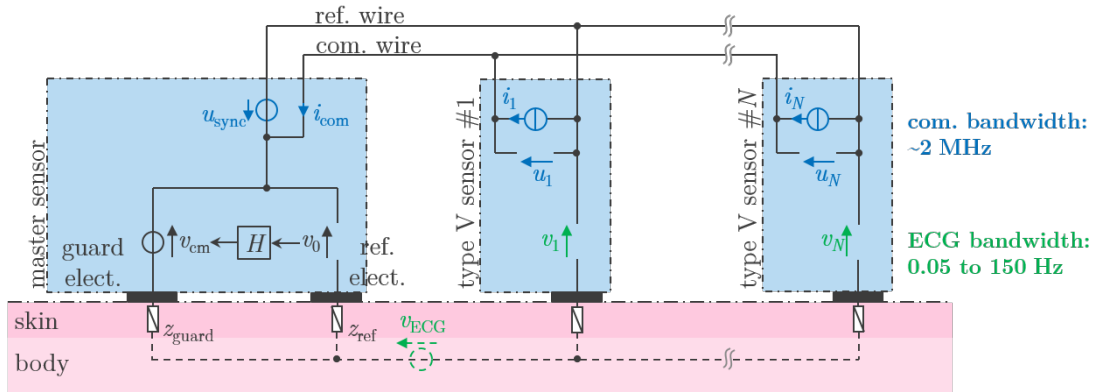
Figure 3.2 – Architecture for full-duplex communication with cooperative sensors. The synchronization signal u_{sync} is sent between the ref. and com. wires, and read as u_1 to u_N in the type V sensors. The communication from the type V sensors to the master sensor is performed via current impulses generated by the current sources i_1 to i_N, and read as i_{com} in the master sensor. The ECG signals are measured as v_1 to v_N.
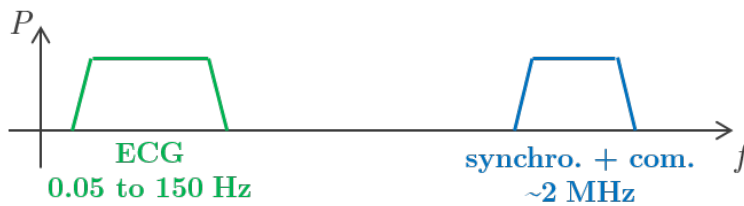
Figure 3.3 – Frequency band allocation for ECG and synchronization signals. The f axis represents the frequency, whereas the P axis represent the amplitude of the signal.

between the cooperative sensors. Since the communication and the measurement share the same unshielded wires, it is required that they do not interfere with each other.

3.2.2 Communication from the Master Sensor to the Type V Sensors

The communication from the master sensor to the type V sensors is based on the circuit of figure 3.1. A second wire, called communication wire (com. wire) is added in parallel to the ref. wire (see figure 3.2). The communication is performed via the voltage source u_{sync} which sends small voltage impulses between the ref. and com. wires. The voltage impulses are read by the type V sensors as u_1 to u_N and used by the master sensor to broadcast information to the type V sensors (e.g., to adjust the gain or other sensor parameters). Moreover, to shift the spectrum of the communication signals to higher frequencies and free the lower part of the spectrum for ECG, it is advantageous to use Manchester encoding [20]. As shown in figure 3.3, the synchronization signal u_{sync} is in a different frequency band than the measured ECG.

As illustrated in figure 3.4, the u_{sync} signal consists of a succession of alternatively positive
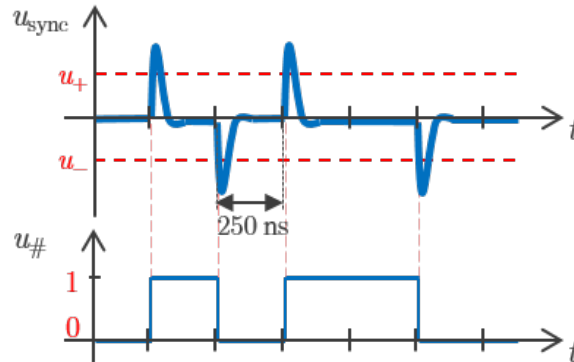
Figure 3.4 – Synchronization voltage signal u_sync and its corresponding digitized signal $u_\#$ recovered in each type V sensor. The signal $u_\#$ is set when u_sync reaches the u_+ threshold, and reset when u_sync reaches the u_- threshold.

and negative impulses. The minimal time between two positive (or two negative) impulses was chosen to 500 ns to have a communication throughput of 2 Mbit/s (the communication protocol is detailed in subsection 3.3.3). By setting two threshold voltages (u_+ and u_-), the signal received as u_1 to u_N can easily be digitized to get the signal $u_\#$. To do this, when the u_+ threshold is reached, the signal $u_\#$ is set, and when the u_- threshold is reached, $u_\#$ is reset. This digitized signal is then used by each type V sensor to recover the clock of the master sensor (in frequency and phase) via the clock data recovery mechanism described in the next subsection. Then, subsection 3.2.4 details a solution for full-duplex communication between the cooperative sensors allowing for gathering the measured data (v_1 to v_N) in the master sensor, which is a prerequisite for ECG visualization, recording, and signal processing.

3.2.3 Clock Data Recovery Mechanism

The proposed communication architecture allows broadcasting data from the master sensor to the type V sensors via the u_sync signal. The synchronization of the cooperative sensors is assured with a clock data recovery mechanism implemented in each type V sensor which recovers the master clock from the u_sync signal via a pulse lock loop (PLL). That way, the master sensor does not need to transmit an additional clock signal. The price to pay for this cabling simplification is that additional electronic circuits in each type V sensor are required.

There are many ways to realize a PLL [45, 85, 86]. Below, the proposed implementation is detailed. The PLL is based on a voltage-controlled oscillator (VCO) and its block diagram is shown in figure 3.5. The PLL recovers the 8 MHz clock of the master sensor (in frequency and phase) from the $u_\#$ signal. The VCO is driven by an analog voltage and its output frequency (*CLK_VCO*) is bounded between 7.7 and 8.3 MHz. Figure 3.6 shows signals *A* and *B* which are two 4 MHz clocks in quadrature generated from flip-flops clocked by the delayed *CLK_VCO*. At each edge of $u_\#$ (rising or falling) the last two states of signals *A* and *B* are memorized by four
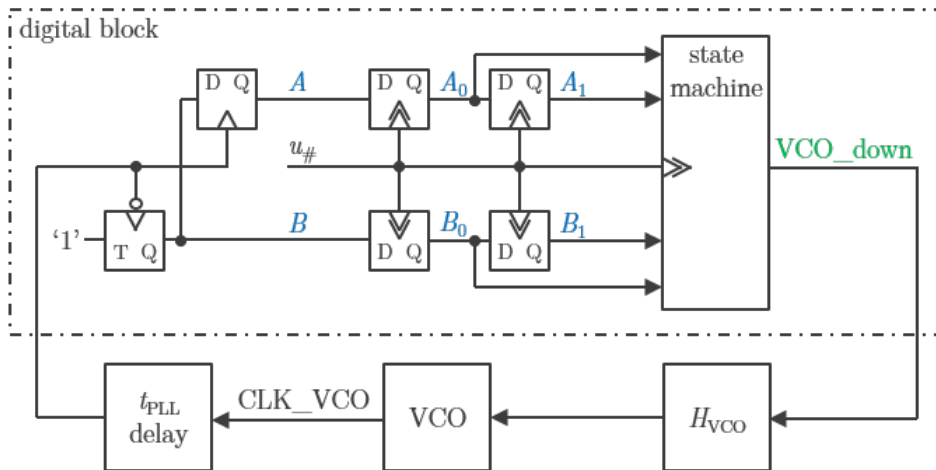
Figure 3.5 – Block diagram of the PLL implemented in each type V sensor.
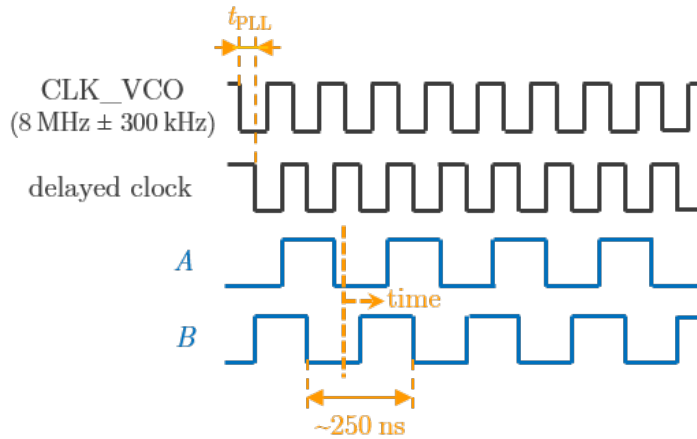
Figure 3.6 – Time diagram of the PLL clock signals.

double-edge D-type flip-flops (see A_0, B_0, A_1, and B_1 in figure 3.5). These four memorized values are then used in a state machine to determine if the logic signal *VCO_down* should be set to '0' (to increase the VCO clock frequency), or to '1' (to decrease the VCO clock frequency). *VCO_down* is thus a binary signal which is used as an input of the analog proportional-integral (PI) controller H_{VCO}. Since $u_\#$ is recovered via the signal u_{sync} and threshold comparators (see figure 3.4) there is a time delay t_{com} between the signal sent by the master sensor and the signal $u_\#$ recovered by a type V sensor. This time delay was measured and its value is approximately 60 ns (see measurement details in subsection 3.5.1, figure 3.19). It has to be noted that the phase of *CLK_VCO* can be adjusted by adding a time delay t_{PLL} in the PLL loop (see "t_{PLL} delay" in figure 3.5). As the PLL is in a closed-loop configuration, the *CLK_VCO* phase will be advanced proportionally to t_{PLL}. To compensate t_{com} and to anticipate a 40 ns time delay for the communication from a type V sensor to the master sensor, t_{PLL} is set to 100 ns ($= 40$ ns $+ 60$ ns).
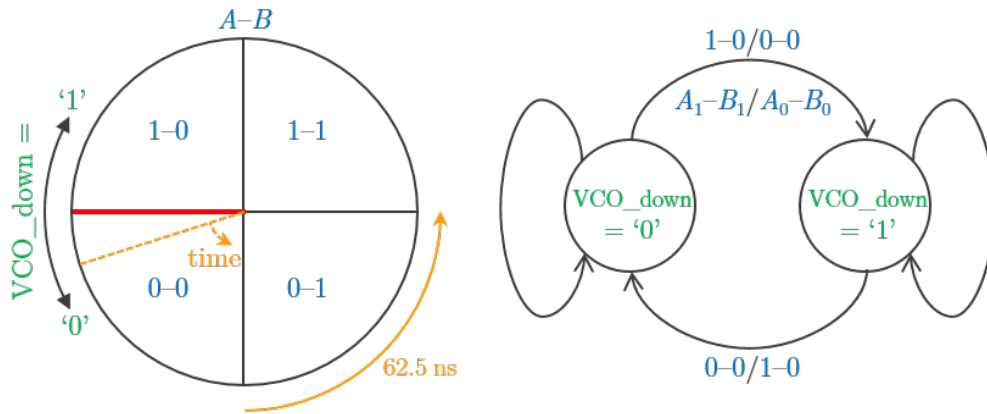
Figure 3.7 – Representation of the PLL state machine: four quadrant representation (left) and state diagram (right).
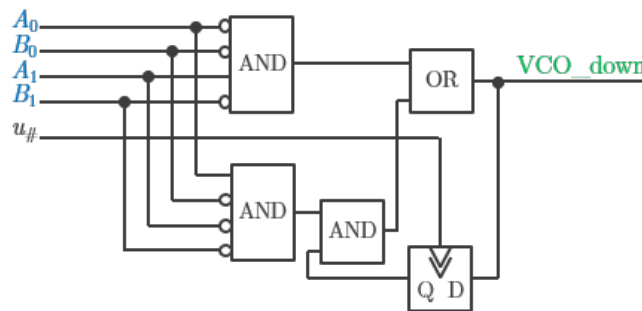
Figure 3.8 – PLL state machine implementation with logic gates and a double-edge D-type flip-flop.

Figure 3.7 (left) shows a four quadrant representation of the signals A and B. When time increases, the time vector turns anticlockwise and makes one full turn in 250 ns (i.e., 62.5 ns per quadrant). The last two states of A and B are memorized in "A_0–B_0" and "A_1–B_1" at each edge of $u_\#$. Since synchronization events (i.e., rising and falling edge of $u_\#$) occur every 250 or 500 ns (see figure 3.4), the time vector will have made approximatively one or two whole turns, respectively. As represented in figure 3.7 (right), if the state of "A–B" changes from "1–0" to "0–0", it means that the VCO clock is too fast, the *VCO_down* signal is thus set to '1'. And if the state of "A–B" changes from "0–0" to "1–0", it means that the VCO clock is too slow, *VCO_down* signal is thus set to '0'. All other states are ignored. Consequently, the PLL sets the VCO frequency in such a way that every $u_\#$ event happens close to the segment between the quadrants "1–0" and "0–0" (red segment in figure 3.7). The clock of each type V sensor is thus locked in frequency and in phase with respect to the master sensor clock. Figure 3.8 shows the state machine implementation with digital logic gates and a double-edge D-type flip-flop.

The digital block of the PLL is implemented with a Coolrunner II CPLD (Xilinx, San Jose, United States), the VCO block is based on a LTC6900CS5 (Linear Technology, Milpitas, United States), and the VCO controller H_{VCO} was implemented with an operational amplifier.
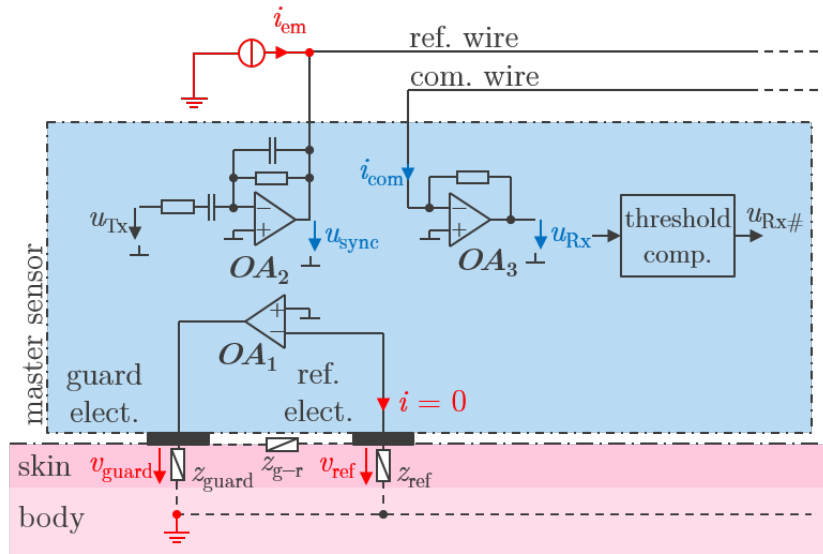
Figure 3.9 – Detailed electronic circuits of the master sensor. The synchronization signal u_sync is generated by the square wave signal u_Tx filtered by a bandpass filter implemented with OA_2. The communication current i_com is converted to the voltage u_Rx by the transimpedance operational amplifier OA_3 and then digitized to get $u_\text{Rx\#}$. The common-mode controller H is implemented with the operational amplifier OA_1. Impedances z_guard and z_ref model the skin impedance under the guard and the ref. electrodes, respectively. Finally, $z_\text{g–r}$ models the impedance at the surface of the skin between the guard and the ref. electrodes.

3.2.4 Communication from the Type V Sensors to the Master Sensor

The communication from the type V sensors to the master sensor is performed via the current sources i_1 to i_N (see figure 3.2). The signal is sent as current impulses with a similar shape as the voltage signal u_sync and in the same frequency band. These impulses are read as i_com in the master sensor. Since all current sources work in parallel, each type V sensor transmits its digitized measured signal (i.e., the ECG signals measured as v_1 to v_N) during a predefined time slot to avoid communication overlap (the communication protocol is detailed in subsection 3.3.3).

Figure 3.9 shows the detailed electronic circuits of the master sensor. The synchronization signal u_sync is generated by the square wave signal u_Tx filtered by a first-order bandpass filter with a central cutoff frequency of 6 MHz. This bandpass filter is implemented with the operational amplifier OA_2. The communication current i_com is converted to the voltage u_Rx by the operational amplifier OA_3 which is mounted in a transimpedance configuration. A similar threshold comparator method as for the voltage signal (see figure 3.4) is used to get $u_\text{Rx\#}$ (digitized value of u_Rx).

Assuming that the chosen transfer function for the controller H is an integrator, it can be implement with a simple operational amplifier (see OA_1 in figure 3.9). In this case, OA_1

implements a follower and its output plays the role of the voltage v_{cm} of figure 3.2. Since the current flowing through the skin impedance z_{ref} is theoretically null, the voltage v_{ref} is equal to zero. Moreover, the voltage between the operational amplifier inputs is controlled to zero since OA_1 is in closed loop. Consequently, the voltage inside the body under the ref. electrode is "copied" to the master sensor ground. Here, the unit gain bandwidth (UGBW) of the operational amplifier must be chosen in such a way that the disturbance current induced on the ref. and com. wires can freely flow through the guard electrode in the ECG bandwidth. As the typical frequency bandwidth of the ECG signal goes from 0.05 to 150 Hz [51], a minimal UGBW of 1500 Hz is advised.

A first limitation of this communication architecture resides in the impedance between the ref. and the com. wires (impedance seen by the voltage source u_{sync}). This impedance depends on two main factors: 1) the stray capacitance between the two wires, and 2) the input impedances of the type V sensors connected to the ref. and com. wires. The voltage between the two external wires varies with respect to u_{sync} and results in a leakage current flowing through the transimpedance amplifier OA_3. Since this impedance is mainly capacitive, the shape of the disturbance current is proportional to the first derivative of the u_{sync} signal. To avoid overlapping between the communication and the disturbance impulses, the communication currents are delayed by half of the period between two successive u_{sync} communication impulses (i.e., 125 ns). Figure 3.10 shows a time diagram of these signals with the resulting disturbances on u_{Rx}. It has to be noted that the disturbance impulses originate from u_{sync}, the moment when they occur is thus well known by the master sensor and can easily be masked if a disturbance crosses the threshold voltages u_{Rx+} and u_{Rx-}.

With this architecture, only two unshielded wires connecting all cooperative sensors in a bus arrangement are required. This new cooperative-sensor approach significantly reduces the cabling complexity of the sensor system since the same wires are used for both measurement and communication purpose.

3.3 Common-Mode Rejection with Single Skin-Contact Sensors

Although the circuit presented in section 3.2 allows eliminating shielded or complex multi-conductor cables, the common-mode rejection requires the master sensor to be equipped with two contacts with the skin. Consequently, the sensor miniaturization is limited. This section details the common-mode rejection model and explains why it is problematic to have both the guard and the ref. electrodes implemented in the same sensor. Then, a solution is presented to split the two-electrode master sensor into two single-electrode sensors.

3.3.1 Common-Mode Rejection Model

As a first approximation, we can model the skin impedance under the guard and the ref. electrodes as z_{guard} and z_{ref}, respectively, and the impedance at the surface of the skin between
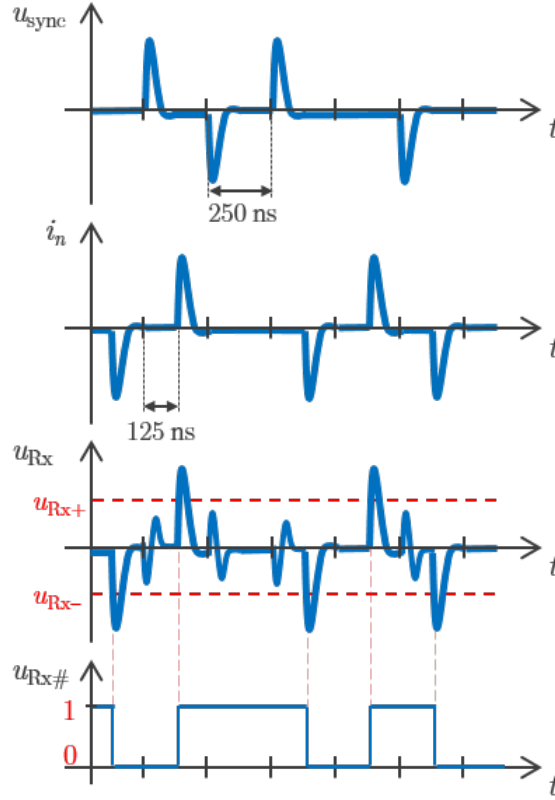
Figure 3.10 – Time diagram of the synchronization voltage u_{sync}, the nth communication current i_n ($n \in \{1, \dots, N\}$), the voltage u_{Rx} resulting from the communication currents i_n and disturbance impulses induced by u_{sync}, and the signal $u_{\text{Rx\#}}$ which is digitized from u_{Rx} and the threshold voltages $u_{\text{Rx}+}$ and $u_{\text{Rx}-}$.

these two electrodes as $z_{\text{g-r}}$ (see figure 3.9). From this model, it is possible to compute the disturbance voltage v_{ref} due to i_{em} flowing through the resistor network modeled by z_{guard}, z_{ref}, and $z_{\text{g-r}}$ (see equation 3.1). Indeed, since the ref. and com. wires are not shielded, they are exposed to electromagnetic disturbances and a current i_{em} flows toward the earth ground via the operational amplifier output of the master sensor (OA_1) which is seen as a low impedance path. Equation 3.1 shows that the disturbance voltage v_{ref} tends to zero if $z_{\text{g-r}}$ tends to infinity. That way, the potential inside the body under the ref. electrode is equal to the potential of the master sensor's ground and the common-mode voltage between the body and the ref. wire (within the bandwidth of the operational amplifier) is close to zero.

$$v_{\text{ref}} = z_{\text{ref}} \frac{z_{\text{guard}}}{z_{\text{guard}} + z_{\text{g-r}} + z_{\text{ref}}} i_{\text{em}} \tag{3.1}$$

In the current implementation of the master sensor, the guard and the ref. electrodes are both
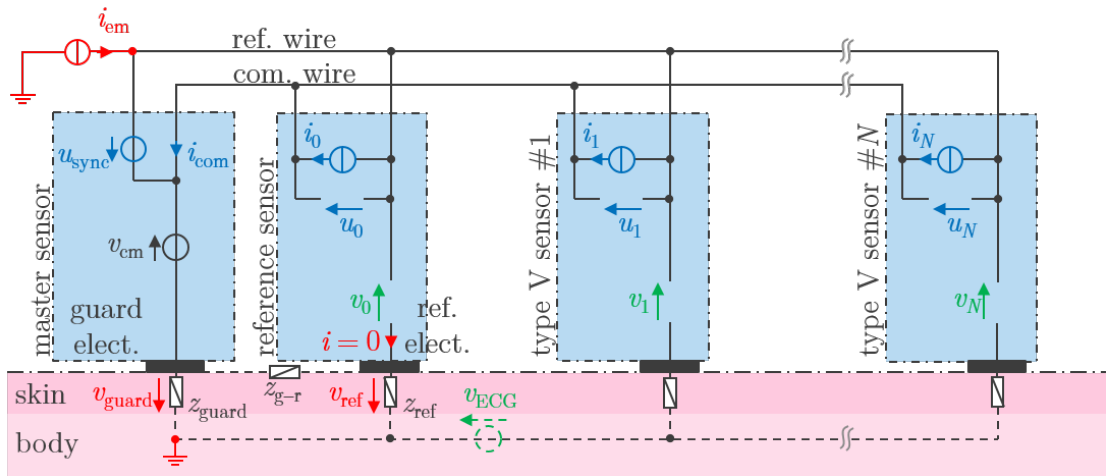
Figure 3.11 – Architecture for common-mode rejection with separate guard and ref. electrodes. The master sensor has now only one skin contact. The reference sensor has a similar architecture as the type V sensors. The voltage v_0 measured by the reference sensor is sent to the master sensor and controlled to zero via the voltage source v_{cm}.

implemented in the master sensor. Consequently, a miniaturization of the master sensor implies a reduction of the distance between these two electrodes, and thus a diminution of the impedance z_{g-r}. A downsizing of the master sensor results thus in a higher common-mode voltage on v_{ref}. Implementing the guard and the ref. electrodes into two separate cooperative sensors would make it possible to place these two electrodes at different locations onto the body, and thus significantly increasing z_{g-r} without any limitations on the size reduction of the sensors. A solution to address this issue is detailed in the next subsection.

3.3.2 Single Skin-Contact Architecture

Figure 3.11 shows an alternative architecture for common-mode rejection with single skin-contact sensors. The guard and the ref. electrodes are now implemented in two separate cooperative sensors, namely the master sensor (which has now only one skin contact) and the reference sensor (which has a similar architecture as a type V sensor). Consequently, it is possible to place them at different locations onto the body to increase z_{g-r}, thus improving the global common-mode rejection according to equation 3.1. In the prior configuration (see figure 3.9) the common-mode controller was realized via the feedback loop of the operational amplifier OA_1. In the new architecture, the voltage v_0 is measured in the reference sensor, its digitized value is sent to the master sensor, and controlled to zero via the voltage source v_{cm}. Consequently, the disturbance voltage v_{guard} induced by i_{em} is compensated via the common-mode controller which controls v_{cm}. The difference with respect to the prior configuration is that the feedback loop of the new common-mode rejection approach also includes the digital communication bus. Consequently, the sampling frequency of v_0 needs to be fast enough to allow a good rejection of the common-mode voltage.

With this configuration, the best open-loop transfer function is $(z-1)^{-1}$, resulting in the rejection of the disturbance voltage v_{guard} by $\|1 - z^{-1}\|$, or by $\|1 - e^{-j2\pi f/f_s}\|$. Here, z corresponds to the z-transform variable, f_s is the sampling frequency of v_0, and f any frequency to be rejected. As an example, for $f_s = 50\,\text{kHz}$, one gets a maximal rejection factor of 159 for mains disturbances (i.e., $f = 50\,\text{Hz}$), which corresponds to an attenuation of the common mode (CMRR$_{\text{FB}}$) of 44 dB [84]. Even if this attenuation prevents the saturation of the amplifier used to measure v_0 to v_N, a residual common-mode voltage is present on the measured voltages. This common-mode voltage is further attenuated when computing the final ECG leads which are defined as the differences (or a linear combination) between the measured voltages. In the cooperative-sensor architecture, the voltages v_0 to v_N are amplified, filtered, and digitized by different analog chains implemented in each sensor. Consequently, the matching between the transfer functions of each measuring sensor impacts the common-mode rejection. The common-mode attenuation of the differential stage (CMRR$_{\text{D}}$) is defined by equation 3.2.

$$\text{CMRR}_{\text{D}} = -20log((1 + P_{\text{G}}) - (1 - P_{\text{G}})) = -20log(2P_{\text{G}}) \tag{3.2}$$

where P_{G} is the precision of the gain of an analog chain at a given frequency. As an illustration, for a gain accuracy of $\pm 1\,\%$ ($P_{\text{G}} = 0.01$), the CMRR$_{\text{D}}$ is equal to 34 dB (in the worst case). This results in a total CMRR of the cooperative-sensor system of 78 dB (= CMRR$_{\text{FB}}$ + CMRR$_{\text{D}}$).

3.3.3   Communication Protocol

The current implementation of the cooperative-sensor system is designed for a maximum of 25 type V sensors. Each type V sensor receives data broadcasted from the master sensor at a rate of 2 Mbit/s. For the communication from the type V sensors to the master sensor, each of the 25 type V sensors has a predefined time slot of 20 µs. This means that any type V sensor can transmit 5 bytes to the master sensor every 500 µs. The upper part of figure 3.12 shows the 25 predefined 20 µs slots corresponding to the 25 type V sensors, whereas the middle part of this figure shows a zoom in on the 5 bytes transmitted by the first type V sensor (slot #1). The lower part shows the transmitted signal u_{Tx} encoded in a Manchester code.

With a resolution of the digitized ECG values of 16 bits, the communication bit rate required for the reference sensor is 800 kbit/s (16 bits at 50 kHz), whereas the bit rate for each type V sensor for a chosen sampling rate of 500 samples/s is 8 kbit/s (16 bits at 500 Hz). The minimal bit rate required for a system with N type V sensors is thus $(800 + N \cdot 8)$ kbit/s.

3.4   Testing Hardware

This section describes the integration of the cooperative-sensor circuit detailed in figure 3.11, as well as the hardware used for its assessment and testing.
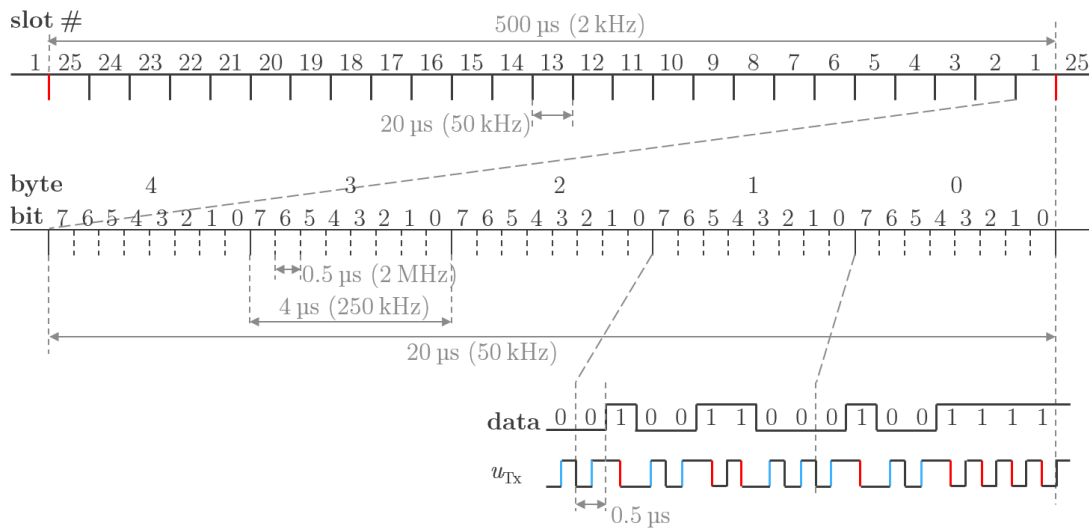
Figure 3.12 – Diagram of the data format for the communication from the type V to the master sensor. The upper part shows the 25 predefined slots corresponding to the 25 type V sensors, the middle part shows a zoom in on the 5 bytes transmitted by the first type V sensor (slot #1), and the lower part shows data encoded in Manchester code. A '0' is expressed as a high-to-low transition (blue) of the u_{Tx} signal, whereas a '1' is expressed as a low-to-high transition (red).

3.4.1 Integration of Sensors

Figure 3.13a shows the physical realization of the master sensor including the electronic circuits and a battery. According to figure 3.11, this sensor has only one electrical contact with the skin implemented as a stainless steel dry electrode. The ref. and com. wires are connected to the sensor via snap buttons inserted in the plastic cover. The master sensor also contains a Bluetooth (BT) module for communication with external devices. Its diameter is about 40 mm.

The reference and the type V sensors have the same shape and the same diameter as the master sensor (see figure 3.13b). They also have a single skin contact and two snaps buttons for ref. and com. wires connections. Since they do not need wireless communication, the reference and type V sensors are thinner than the master sensor.

3.4.2 Test Bench for Communication Testing and Noise Performance Assessment

To validate the cooperative-sensor communication principle and to assess the noise performances of the system, a test bench was built containing one master, one reference, and two type V sensors (type V sensors #1 and #2), see figure 3.14. Cooperative sensors are contacted via dedicated printed circuit boards (PCBs). A resistance-capacitance (RC) circuit that mimics the skin impedance (4.7 kΩ resistance in parallel to a 10 nF capacitance) is placed in series with each cooperative sensor skin electrode. The RC circuits are connected together via an external wire (see yellow wire in figure 3.14). Two unshielded wires corresponding to the ref. and com. wires connect all sensors together according to the architecture shown in figure 3.11.

a) Master sensor

b) Reference or type V sensor
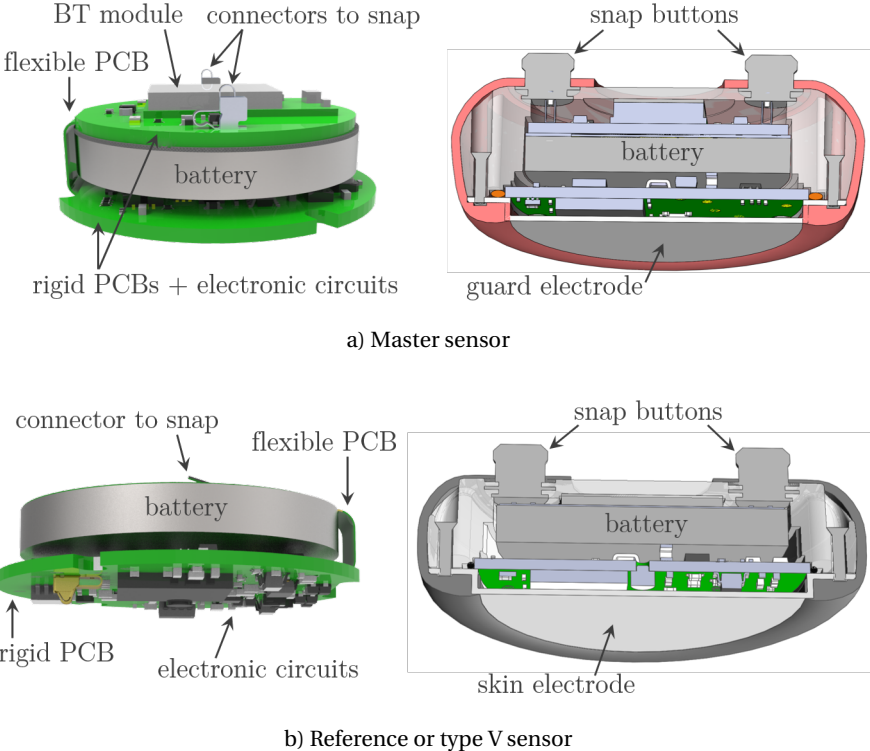
Figure 3.13 – 3D drawing of a) the master sensor, and b) a type V sensor, including the electronic circuits and a battery. For both sensors, the ref. and com. wires are connected via snap buttons and the electrical contact with the skin is made via a stainless steel dry electrode.
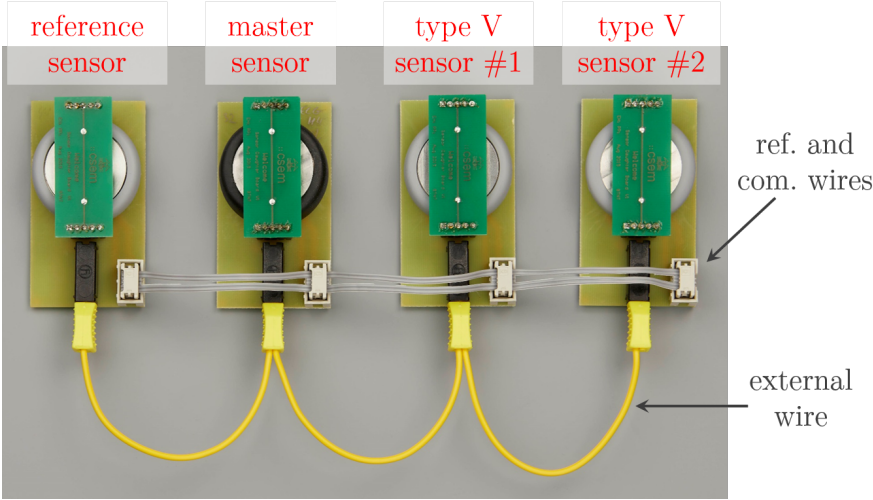
Figure 3.14 – Test bench for testing the sensor-to-sensor communication and assessing the noise performance. One master, one reference, and two type V sensors are connected together via dedicated PCBs and wires.
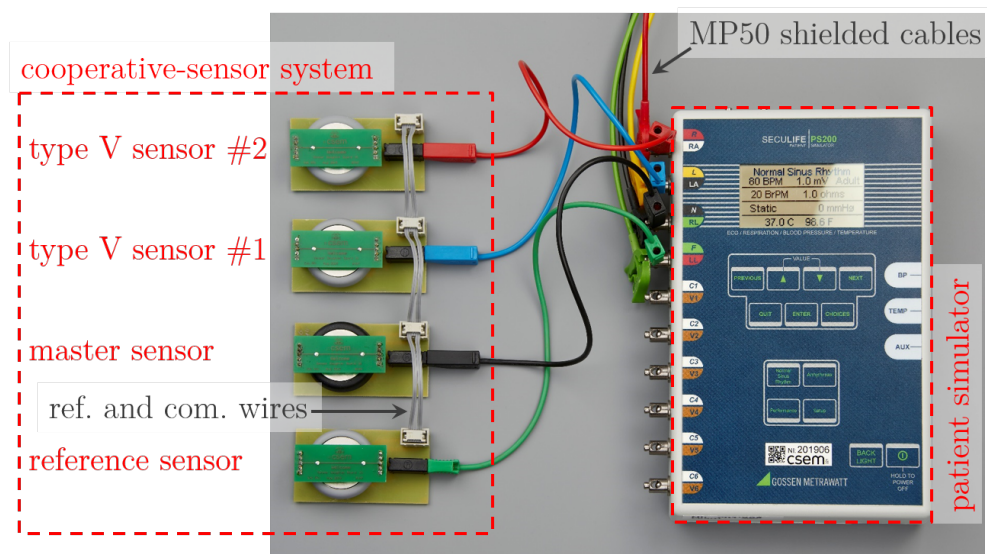
Figure 3.15 – Test bench for system verification with a patient simulator. Both, the cooperative-sensor system and the gold-standard medical device (the MP50) are connected to the patient simulator (the Seculife PS200).

3.4.3 Verification with a Patient Simulator

The goal of this test setup is to compare the cooperative-sensor system with a gold-standard medical device—the IntelliVue MP50 bedside patient monitor (Philips, Dublin, Ireland). The ECG filter of the MP50 is set to diagnostic mode and the ixTrend software (Ixellence GmbH, Wildau, Germany) is used to record signals from the MP50. As shown in figure 3.15, a patient simulator Seculife PS200 (Gossen Metrawatt, Nürnberg, Germany) is used. Both, the MP50 and the cooperative-sensor system are connected in parallel to the patient simulator. For this measurement, four cooperative sensors are connected: the master sensor (at the right leg (RL) connection), the reference sensor (at the left leg (LL) connection), and two type V sensors (at the left arm (LA) and right arm (RA) connections). The cooperative sensors are contacted via dedicated PCBs and linked to the patient simulator with unshielded test leads. Two other unshielded wires corresponding to the ref. and com. wires are used to connect the cooperative sensors together (cf. figure 3.11). The MP50 leads are connected to the patient simulator via their dedicated shielded cables.

3.4.4 System Integration in a 12-Lead ECG Holter

A wearable 12-lead ECG monitoring system (an ECG Holter) based on the cooperative-sensor circuit presented in figure 3.11 was integrated in a vest (see figure 3.16). It is made of one master, one reference, and eight type V sensors. The ECG voltages are measured as v_0 in the reference sensor, and as v_1 to v_8 in the type V sensors. The sensors are attached to the vest using their two snap buttons. The ref. and com. wires are two unshielded wires integrated in
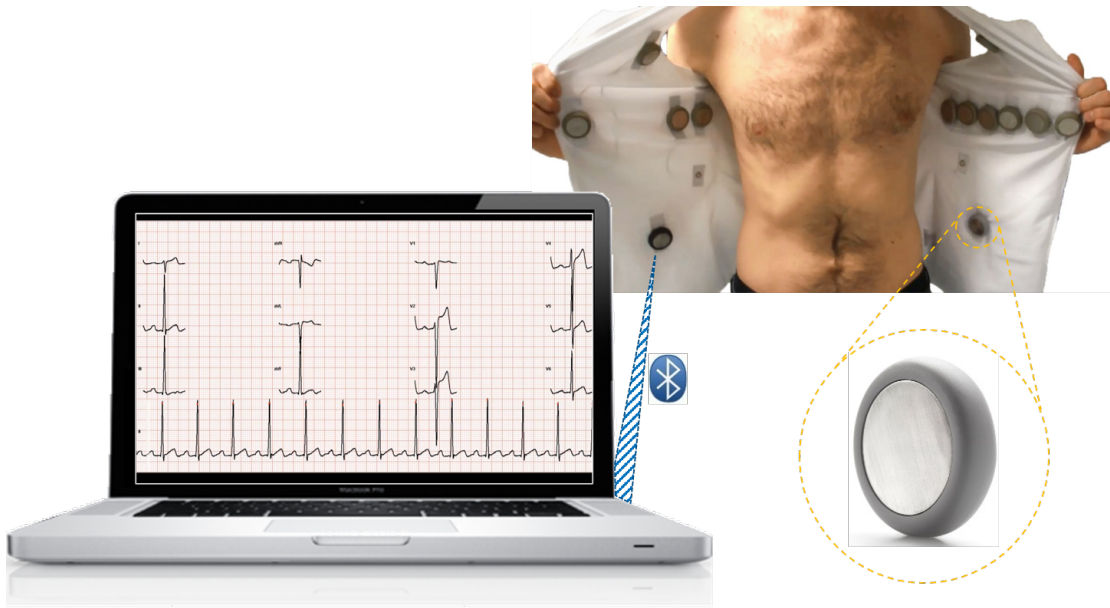
Figure 3.16 – Realization of a 12-lead ECG Holter with cooperative sensors. The ECG signals are measured by the reference sensor (as v_0), and by the eight type V sensors (as v_1 to v_8). The measured data are gathered in the master sensor via the two-wire communication bus and transferred in real time via a Bluetooth communication to a smart device for processing, recording, and monitoring purpose.

the textile of the vest. To comply with the Mason-Likar configuration for modified 12-lead ECG monitoring systems [91, 101], the master sensor is placed onto the skin at the RL location, the reference sensor at the LL location, and the eight type V sensors are placed at the RA, LA, and the six precordial locations (*V1* to *V6*). To comply with the international standard for ECG measurement [51], the sampling rate of the measured ECG is 500 Hz and its bandwidth is limited between 0.05 and 150 Hz.

In the cooperative-sensor architecture, any sensor-site specific potential on the skin is measured with respect to the ref. wire. The digitized ECG signals are then gathered in the master sensor and digital data processing is required to extract clinically relevant 12-lead information. The bipolar extremity leads (leads *I*, *II*, and *III*) and augmented leads (leads *aVR*, *aVL*, and *aVF*) are computed according to table 3.1, and the six precordial leads (leads *V1* to *V6*) are computed by the difference between the ECG signals digitized by sensors located at the six precordial locations and the central terminal (*CT*, defined in table 3.1).

To compare the signals measured with the cooperative-sensor system and the gold-standard medical device (the MP50), both systems were simultaneously placed on a healthy volunteer (see figure 3.17). The MP50 was connected via its dedicated shielded cables to four gel electrodes placed at the RL, LL, LA, and RA locations.

Table 3.1 – ECG leads and their identifications, adapted from [51].

Lead code	Definition[1]	Name of the lead
I	$I = LA_\# - RA_\#$	
II	$II = LL_\# - RA_\#$	Bipolar extremity leads
III	$III = LL_\# - LA_\#$	
aVR	$aVR = RA_\# - (LA_\# + LL_\#)/2$	
aVL	$aVL = LA_\# - (RA_\# + LL_\#)/2$	Augmented leads Goldberger
aVF	$aVF = LL_\# - (LA_\# + RA_\#)/2$	
CT	$CT = (LA_\# + RA_\# + LL_\#)/3$	Central terminal according to Wilson [103]

[1] $LA_\#$, $RA_\#$, and $LL_\#$ correspond to the ECG values digitized by the cooperative sensors located at the left arm, right arm, and left leg locations, respectively.
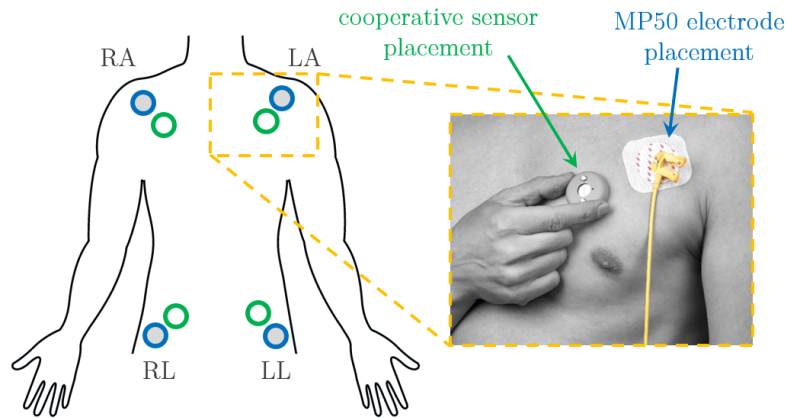
Figure 3.17 – Electrode placement for comparing the cooperative-sensor system (dry electrodes) with the MP50 gold-standard medical device (gel electrodes).

3.5 Testing Procedures and Results

3.5.1 Communication Testing and Noise Performance Assessment

Communication Signals This test consists of measuring different communication signals with the test bench described in figure 3.14. The first signal to measure is the synchronization signal u_{sync} to verify if its shape corresponds to the expected signal shown in figure 3.10. This signal was measured with a differential probe connected between the two external wires (ref. and com. wires). Figure 3.18 shows that its peak-to-peak amplitude is about 300 mV.

Then, the binary signal u_{Tx} transmitted by the master sensor and the signal $u_\#$ recovered by a type V sensor were measured to verify the correctness of the recovered signal and to measure the time delay induced by OA_2 (see figure 3.9) and the threshold comparators used to recover $u_\#$ (see figure 3.4). Figure 3.19 shows that the time delay between the signal u_{Tx} and the recovered signal $u_\#$ is about 60 ns.
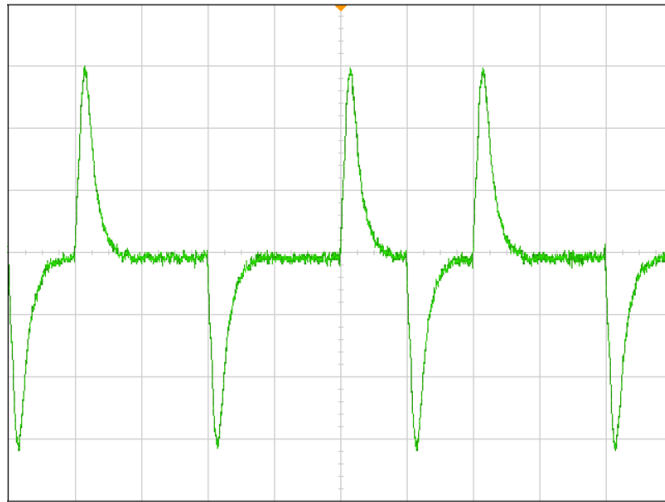
Figure 3.18 – Synchronization signal u_{sync} measured between the ref. and com. wires. (50 mV/div. and 250 ns/div.).
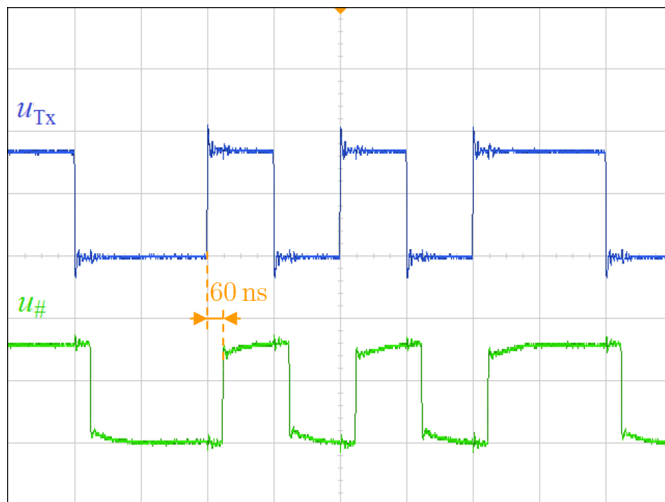
Figure 3.19 – Binary signal u_{Tx} transmitted by the master sensor and the signal $u_{\#}$ recovered in a type V sensor. The time delay between the transmitted and recovered signals is about 60 ns. (2 V/div. and 250 ns/div.).

Finally, the signal u_{Rx} recovered by the master sensor (see figure 3.9) was measured to ensure that the communication signal induced by communication currents (i_0, i_1, and i_2) can properly be discriminated from the disturbance signal induced by u_{sync} (cf. figure 3.10). As a reminder, this disturbance signal is induced by u_{sync} and results from the leakage current between the two external wires. In figure 3.20, the impulses originating from the communication current are marked with green arrows pointing downwards, and the impulses originating from the disturbance current are marked with red arrows pointing upwards. The u_{Rx} signal is digitized via the two threshold voltages $u_{\text{Rx+}}$ and $u_{\text{Rx-}}$ to get $u_{\text{Rx\#}}$. When the $u_{\text{Rx+}}$ threshold is reached, $u_{\text{Rx\#}}$ is set, and when the $u_{\text{Rx-}}$ threshold is reached, $u_{\text{Rx\#}}$ is reset. The red cross in
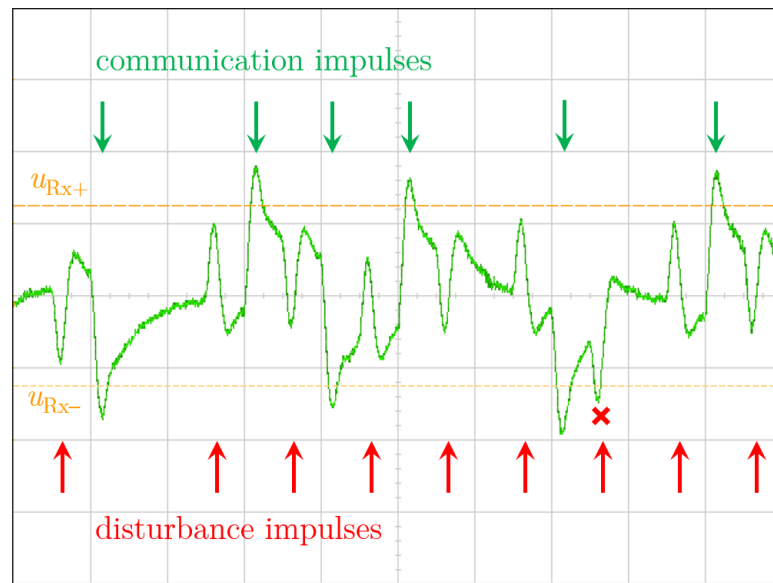
Figure 3.20 – Signal u_{Rx} at the output of the transimpedance amplifier OA_3 of figure 3.9. The impulses on u_{Rx} originate from the communication currents and the disturbance currents induced by u_{sync}. (100 mV/div. and 250 ns/div.).

figure 3.20 shows that the disturbance impulses may cross the threshold voltages. However, since the time when these disturbance impulses occurs is well known by the master sensor (as they result from u_{sync}), they are easily masked.

Jitter Measurement   For this test, the jitter between the 8 MHz clock of the master sensor and the 8 MHz clock recovered by the PLL of a type V sensor was measured by using the test bench shown in figure 3.14. Figure 3.21 shows that this jitter is approximately ±15 ns. During this recording, the display persistence time of the oscilloscope was set to 10 s. This figure also shows that there is a phase shift between the master clock and the recovered clock. This phase shift was described in subsection 3.2.3 and is used to compensate the communication delay of the signal $u_{\text{Rx\#}}$.

Noise Performance Assessment   In the cooperative-sensor architecture, the communication and the measurement share the same unshielded wires. The goal of this test is to ensure that they do not interfere with each other and that the impact on the ECG measurement noise is reasonable. For this purpose, two different measurements were performed with the test bench described in figure 3.14: 1) an absolute measurement, which corresponds to the digitized value measured by each cooperative sensor, and 2) a differential measurement, which corresponds to the difference between the values measured by two different type V sensors.

Figure 3.22 shows the absolute noise (upper plot), and differential noise (lower plot). The absolute peak-to-peak noise over a 10 s period is about 40 µV (standard deviation of 5.5 µV for
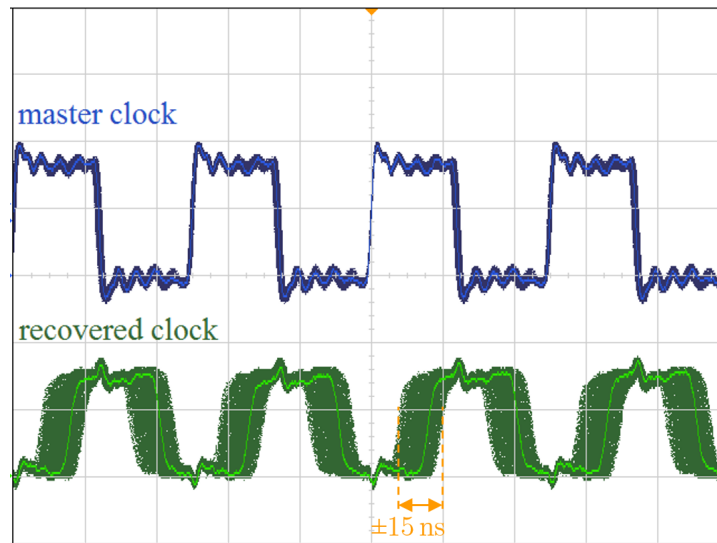
Figure 3.21 – Jitter between the 8 MHz master clock and the 8 MHz clock recovered by a type V sensor. (2 V/div. and 50 ns/div.).

the type V sensor #1, and 6.9 µV for the type V sensor #2), whereas the differential peak-to-peak noise between these two sensors is approximately 30 µV (standard deviation of 4.4 µV).

3.5.2   Verification with a Patient Simulator

For this verification, the test setup shown in figure 3.15 was used. Figure 3.23 shows a portion of the signal acquired at lead *II*—which corresponds to the difference between ECG voltages measured between type V sensors placed at the LL and RA locations—and measured by both the medical device (the MP50) and the cooperative-sensor system.

3.5.3   Verification on a Healthy Volunteer

This test was performed on one healthy male subject and aims at demonstrating, in a real-life scenario, the proper operation of a wearable 12-lead ECG monitoring system based on cooperative sensors (see hardware presented in subsection 3.4.4). For this recording, the subject was lying in supine position. Figure 3.24 shows a portion of lead *II* compared with the MP50 medical device, whereas figure 3.25 and figure 3.26 show the 12 ECG leads measured with the cooperative-sensor system and computed according to table 3.1.

3.5.4   Exercise Stress Test on a Healthy Volunteer

The goal of this test is to qualitatively assess the ECG performance of the dry-electrode cooperative-sensor system during exercise stress test performed on a stationary bicycle er-goselect200 (ergometer from Ergoline, Bitz, Germany). This exercise stress test was made on
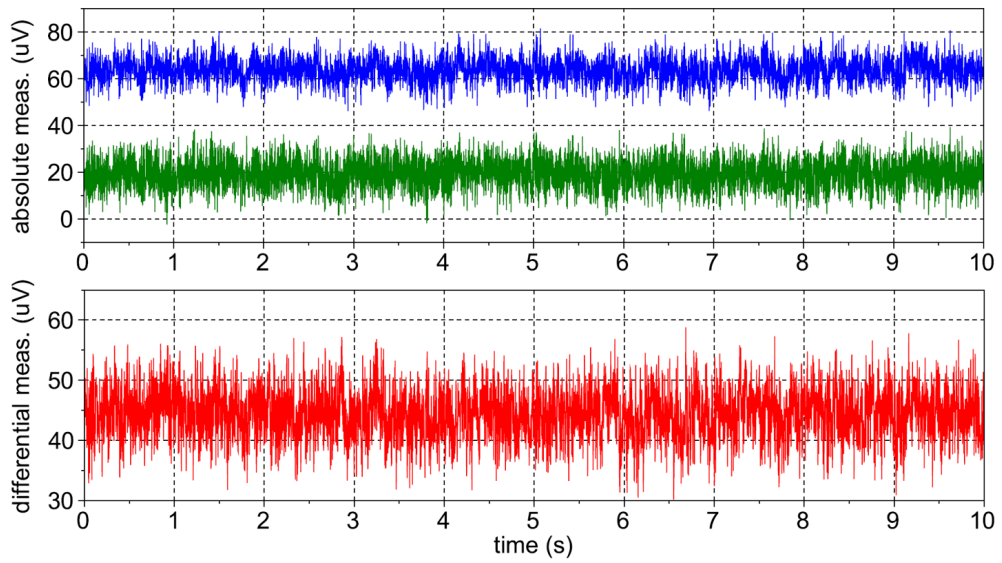
Figure 3.22 – Absolute noise (upper plot) and differential noise (lower plot) measured with cooperative sensors over a 10 s period.
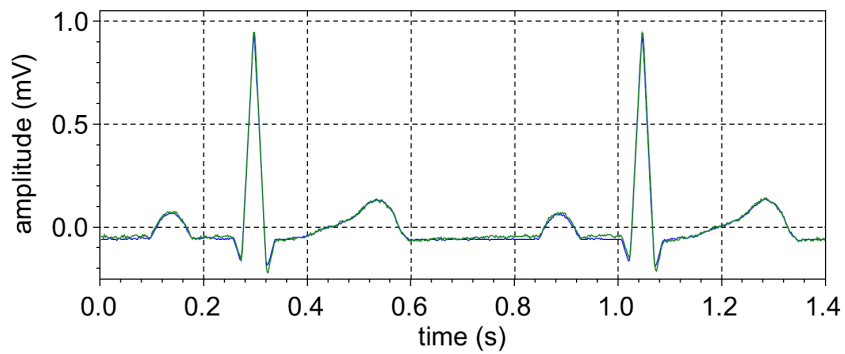
Figure 3.23 – Verification with a patient simulator. Portion of lead *II* measured by both the MP50 (blue signal) and the cooperative-sensor system (green signal).
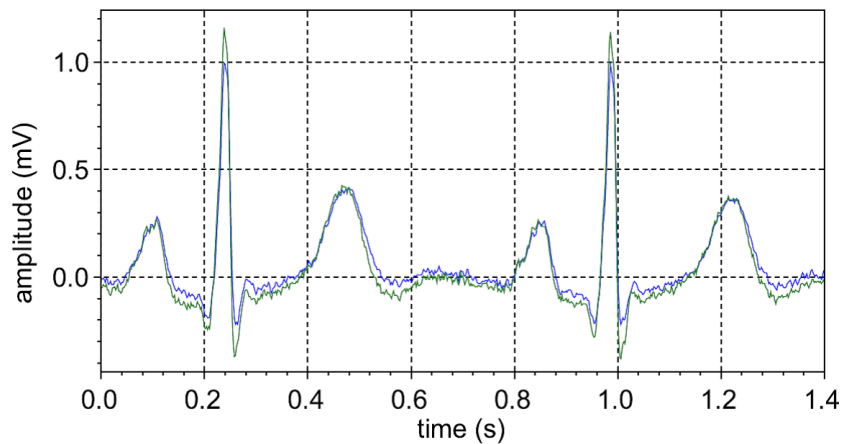
Figure 3.24 – Verification on a healthy subject. Portion of lead *II* measured by both the MP50 (blue signal) and the cooperative-sensor system (green signal).
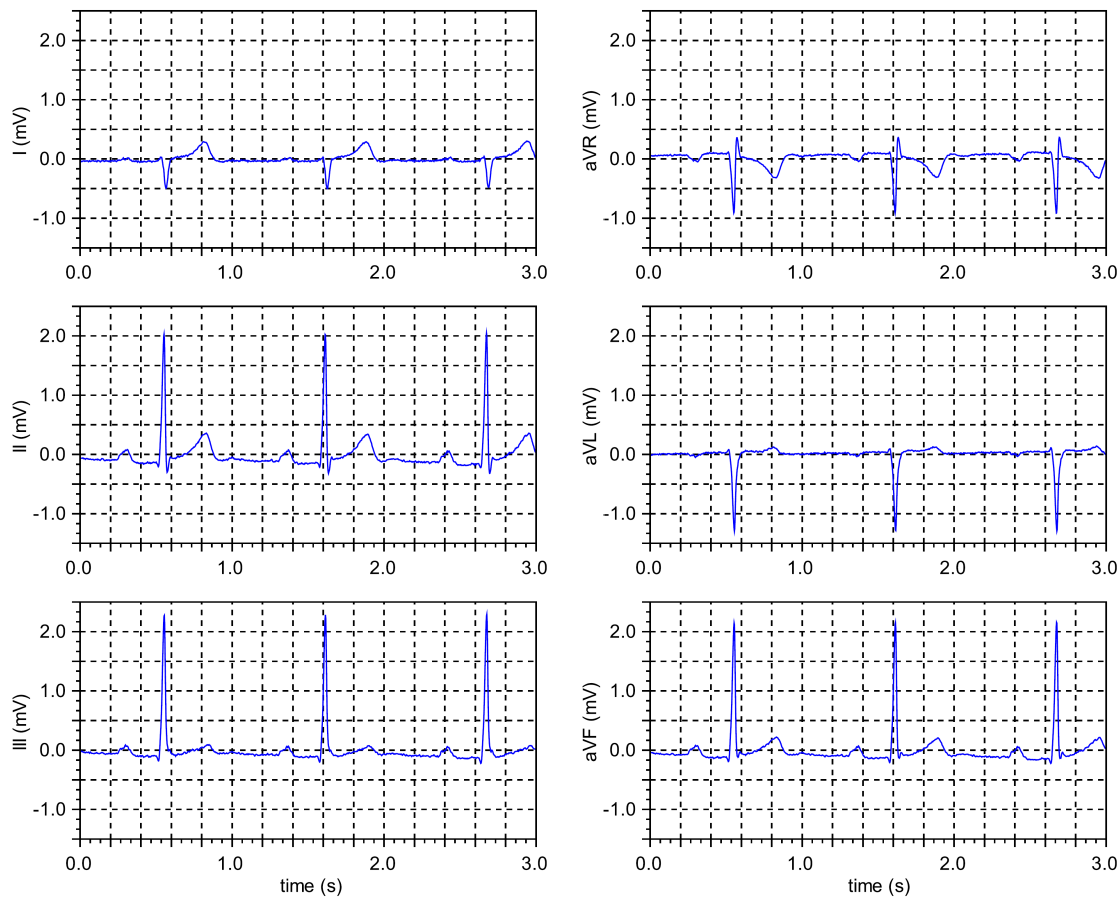
Figure 3.25 – 12-lead ECG measured with cooperative sensors on one healthy subject. Left column represents leads *I*, *II*, and *III*, and right column represents leads *aVR*, *aVL*, and *aVF*.

one healthy male subject with the setup shown in figure 3.27. A gold-standard 12-lead ECG system—the Cardiovit CS–200 (Schiller, Baar, Switzerland)—was used as a reference and replace the MP50 used in the previous subsection. The limb electrodes (LA, RA, LL, and RL) were placed at locations as close as possible to those of cooperative sensors. The subject underwent a protocol of three steps: 1) a few minutes in resting (in supine position), 2) exercise stress test on the ergometer (25 W–steps, each 2 min long, from 50 W and up to subject's capability), and 3) recovery in supine position.

Figure 3.28a to figure 3.28c show ECG signals (measured on lead *II*) obtained from the medical device (black signals) and from the dry-electrode cooperative sensors (red signals) during the three phases of the protocol. As a first qualitative observation, these figures show that the signals acquired from the two systems are very similar. When there is some noise on the signals, it appears on both of them simultaneously (which means that the electrical artifact is already present on the body). Figure 3.28d shows a ventricular ectopic beat captured during the recovery phase. Finally, figure 3.28e shows that the baseline wandering is similar for both systems. It has to be noted that the baseline of the data acquired with the Cardiovit CS–200 may
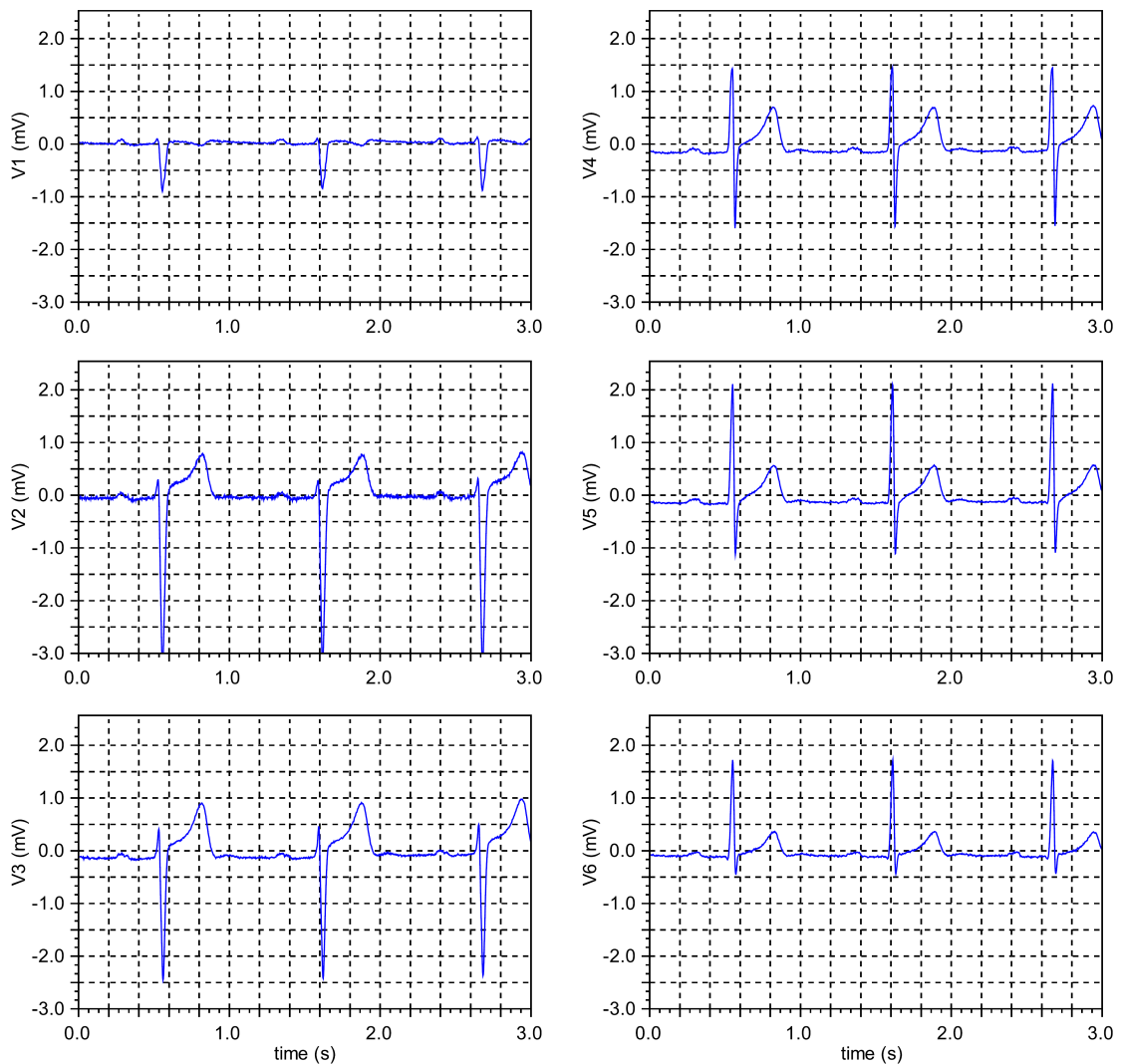
Figure 3.26 – 12-lead ECG measured with cooperative sensors on one healthy subject representing leads *V1* to *V6*.

be improved via signal processing with their baseline stabilizer. This filter aims at reducing the baseline fluctuations without changing the measurement values.

3.6 Discussion

This chapter presents a novel sensing architecture based on active sensors (so-called cooperative sensors) for multilead ECG measurement. The active sensors are directly applied onto the skin and connected together in a bus arrangement via two unshielded wires. The elimination of the shielded cables and of the central unit classically used for high-quality ECG measurement make the cabling of the measurement system simple and easy to integrate. The herein presented architecture allows gathering the measured data in one single location (in
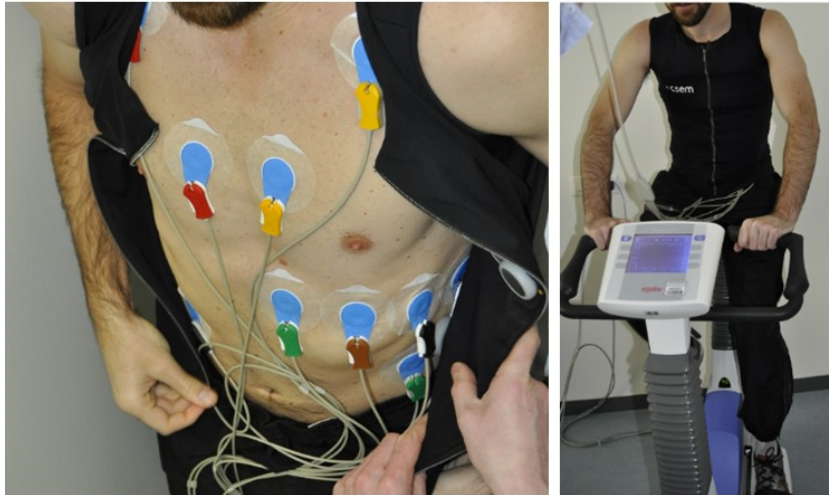
Figure 3.27 – Left: test setup with both the cooperative-sensor system and the gold-standard medical device (Cardiovit CS–200) connected to the subject. Right: subject performing the exercise stress test.

the master sensor) via the full-duplex communication bus with a throughput of 2 Mbit/s.

The synchronization mechanism and its underlying PLL allow recovering the master clock with a jitter of about ±15 ns. This jitter is far below the ±20 ms requirement set to guarantee the temporal alignment for an ECG according to the international standard [52]. The measurement of figure 3.21 also shows that the frequency and phase of the recovered clock are stable compared to the master clock.

One limitation of the presented architecture is the impedance between the two external wires which impacts on the maximal number of sensors in the system. Indeed, if this impedance decreases (e.g., by increasing the number of type V sensors in parallel), the amplitude of the disturbance impulses shown in figure 3.10 and figure 3.20 increases. Consequently, higher disturbances may induce communication errors. In the current implementation, the system works with up to 25 type V sensors.

As shown in figure 3.22, the absolute noise is approximately 40 μV peak-to-peak (noise measured by each individual type V sensor), whereas the differential noise is approximately 30 μV peak-to-peak (noise measured between two type V sensors). The absolute noise is on one hand due to the noise contribution of the type V sensor analog chain, and on the other hand due to the noise induced by the master sensor on the ref. wire. Indeed, the detailed electronic circuit of the master sensor (see figure 3.11) shows that the ref. wire potential is set via the voltage source v_{cm} which has its intrinsic noise. Moreover, the master sensor contains other digital circuits (e.g., microcontroller, memory) and wireless modules that may have an impact on the ref. wire noise. Consequently, the noise induced by the master sensor impacts the absolute noise measured by the type V sensors. However, since this common-mode noise is

a) Protocol phase 1: at rest (supine position)

b) Protocol phase 2: during the exercise stress test

c) Protocol phase 3: during recovery (supine position)

d) Example of ventricular ectopic beat during recovery

e) Comparison of baseline wandering during the exercise stress test (measurement time = 160 s)
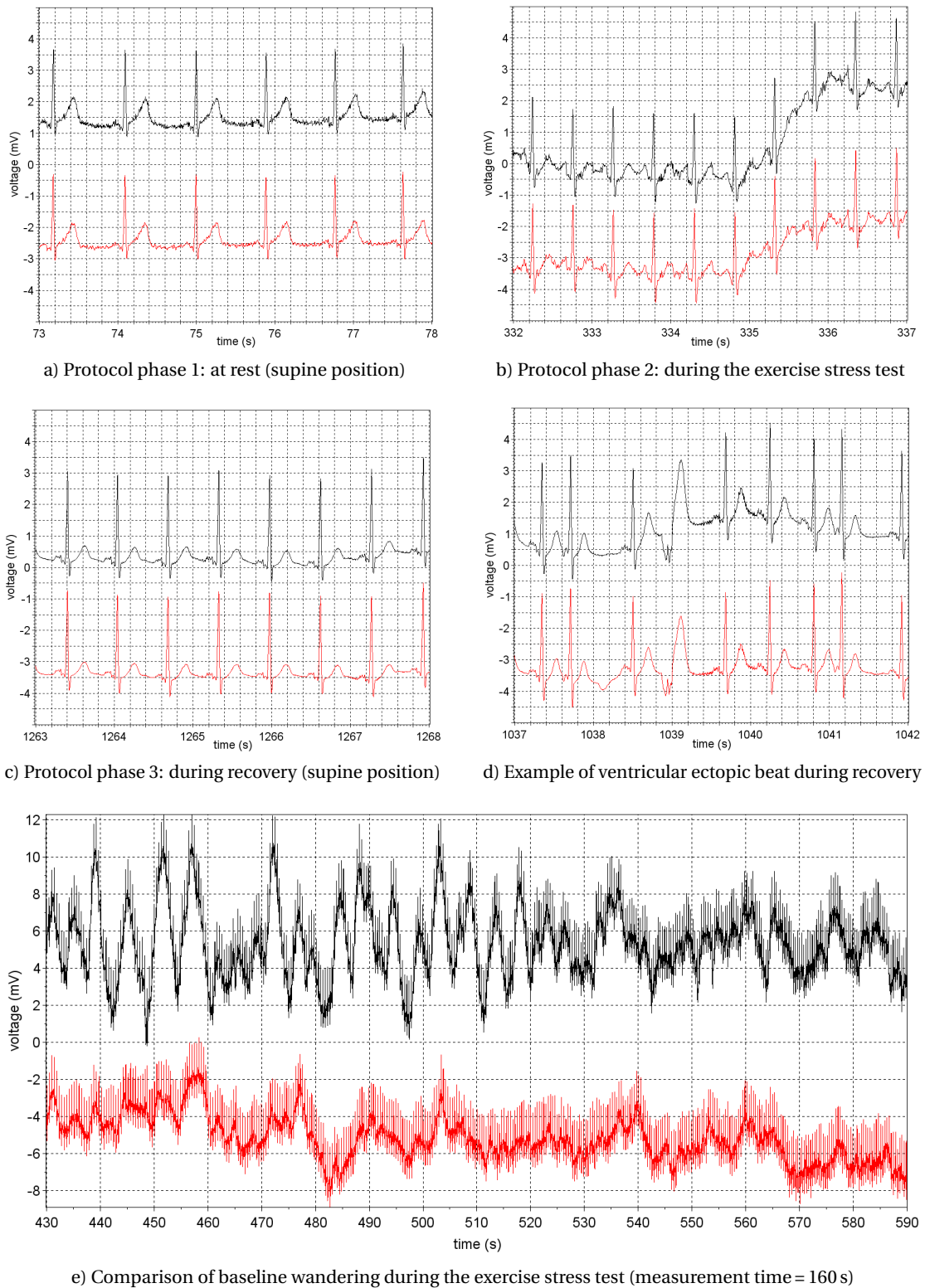
Figure 3.28 – Comparison of typical ECG signals measured on lead *II* with the Cardiovit CS–200 (black signals) and the dry-electrode cooperative-sensor system (red signals).

measured by all type V sensors, it is attenuated when differential measurements are performed. Measurements made in subsection 3.5.1 confirmed that the differential noise ($30\,\mu V$) is lower than the absolute noise ($40\,\mu V$). This property of the proposed architecture implies that the noise resulting from the wireless communication modules and the digital processing in the master sensor are attenuated by performing differential measurements between the type V sensors.

The differential noise measured with the cooperative-sensor system is compliant with the essential performance of ECG systems according to the international standard [51] which states that the input referred noise shall not exceed $30\,\mu V$ peak-to-peak over any $10\,s$ period. It has to be noted that this requirement is less restrictive for ambulatory ECG systems where the maximal peak-to peak noise is $50\,\mu V$ [52].

This chapter also demonstrates the feasibility of measuring a 12-lead ECG with cooperative sensors in a real-life scenario. The system contains one master, one reference, and eight type V sensors connected via the proposed two-wire bus. The ECG signals are synchronously acquired and their digitized values are gathered in the master sensor. Even though the wires that link all sensors are not shielded, they do not interfere with each other and there is no mains disturbance visible in the ECG signals (see figure 3.24). Moreover, measurements showed that the dry-electrode cooperative-sensor technology provides signals—at rest and during exercise stress tests—of quality at least equivalent to gold-standard medical devices.

Another important aspect of the developed system is the use of dry electrodes. Indeed, compared to adhesive gel electrodes which are classically used in clinical applications, dry electrodes are usually characterized by a higher skin-contact impedance [23]. Consequently, the input impedance of the voltage-sensing electronic circuit must to be higher to guarantee a high common-mode rejection ratio (CMRR) [27]. Moreover, due to this high skin-contact impedance, a low bias current is also required to limit motion artifacts [115]. With the cooperative-sensor architecture, the analog frontend of each sensor is directly applied onto the skin. Consequently, the input impedance of the voltage-sensing circuit is optimal since the input parasitic capacitance is minimum (in opposition to classical star-arrangement architectures where the input impedance is impacted by the parasitic capacitance of the shielded cables).

The current implementation of the system is designed with off-the-shelf discrete components (including a CPLD). Consequently, the system is not fully optimized in terms of size and power consumption. The development of an application-specific integrated circuit (ASIC) would improve the power consumption and allow a significant miniaturization of the sensor system. Moreover, the throughput of the proposed system is 2 Mbit/s which is oversized in view of a 12-lead ECG system, however, it allows adding more signals in further developments, paving the way towards more complex wearable systems requiring the measurement of a higher numbers of physiological signals.

Although this chapter focuses on the application of cooperative sensors for ECG measurement,

the same architecture is fully applicable to the assessment of other biopotentials (e.g., EMG, EEG, etc.), or other physiological signals such as bioimpedance. The next chapter details the analog frontend adaptations necessary for multichannel bioimpedance measurement.

4 Cooperative Sensors for Synchronous ECG and EIT Measurement

The present chapter demonstrates the feasibility of cooperative sensors for multichannel bioimpedance (i.e., EIT) and synchronous multilead ECG measurement. Based on the circuit presented in figure 3.2, section 4.1 details the extensions of the cooperative-sensor architecture necessary for fully-parallel EIT with simultaneous current injection and parallel voltage measurement via a frequency-division multiplexing approach. Section 4.2 and section 4.3 show the testing hardware, procedures, and results allowing for the calibration of the proposed EIT system, as well as the assessment of its noise performance. Section 4.3 also shows preliminary measurements on a healthy volunteer demonstrating the ability of the proposed system to simultaneously measure EIT data and multilead ECG. Finally, section 4.4 is a short discussion about the use of the cooperative-sensor architecture in the context of EIT. The content presented in this chapter is adapted from the postprint version of [82].

4.1 System for Synchronous ECG and EIT Measurement

4.1.1 System Architecture

The enhanced system architecture is based on the initial cooperative-sensor design presented in figure 3.2. The two-wire communication bus continues its function for sensor synchronization and gathering of the measured data in the master sensor. To enable bioimpedance measurement, a new type of sensor (a current-injecting sensor, a "type I" sensor) is added, allowing the injection of a current at a frequency of 50 kHz. Also, the analog frontends of the type V sensors were extended to measure and demodulate the resulting 50 kHz components of the measured voltage signal. Figure 4.1 shows the enhanced architecture which consists of three types of sensors: 1) the master sensor, 2) the type I sensors for EIT current injection, and 3) the type V sensors for biopotential measurement. This system has a fully-parallel architecture—meaning that all measuring currents and all resulting voltages are simultaneously injected and measured—with a variable number of voltage measurements (the type V sensors numbered from 1 to N in figure 4.1) and current sources (the type I sensors numbered from $N+1$ to $N+M$). The type V sensors are equipped with communication current sources
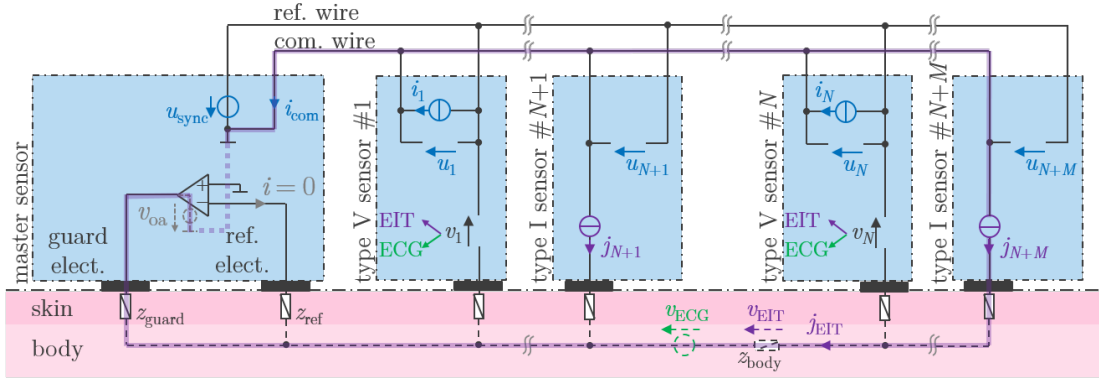
Figure 4.1 – Architecture for multichannel bioimpedance (EIT) and multilead ECG measurement with cooperative sensors. In addition to the abbreviations defined in figure 3.2, j_{N+1} to j_{N+M} are the EIT currents injected by the type I sensors number $N+1$ to $N+M$ (the current loop of j_{N+M} is highlighted in violet). The EIT voltage v_{EIT} results from the 50 kHz current j_{EIT} flowing through the bioimpedance z_{body}. The biopotentials v_1 to v_N are measured in the ECG and EIT bandwidths, and v_{oa} is the output voltage of the operational amplifier.
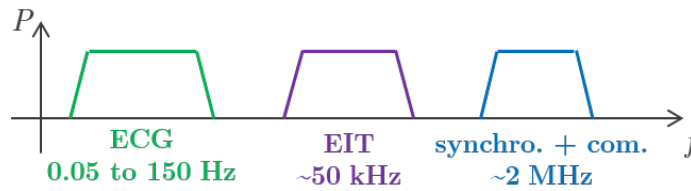
Figure 4.2 – Frequency band allocation for ECG, EIT, and communication signals. The f axis represents the frequency, whereas the P axis represent the amplitude of the signal.

(i_1 to i_N) to communicate the measured data (or any other information) to the master sensor.

With this configuration, the supply voltage of each sensor is floating with respect to the other sensors. The ground voltage of the master sensor is fixed to the body potential (measured at the ref. electrode) via its operational amplifier. The voltage difference between the operational amplifier inputs is controlled to zero via its feedback loop which is closed through the body (via the ref. and guard electrodes and their respective skin impedances).

Figure 4.2 shows the frequency separation of data on the two-wire bus: communication operates at frequencies around 2 MHz, ECG signals are measured between 0.05 and 150 Hz, and bioimpedance (i.e., EIT) signals around 50 kHz.

4.1.2 Bioimpedance Measurement Principle

Bioimpedance signals are acquired by injecting electrical currents with the type I sensors at a carrier frequency of 50 kHz and measuring the resulting voltages with the type V sensors. The

50 kHz carriers are synchronous (in frequency and in phase) thanks to the synchronization and communication bus detailed in subsection 3.2.2. The carrier amplitudes of each current (j_{N+1} to j_{N+M}) is individually controlled by the master sensor and refreshed at a frequency of 2 kHz, thus allowing for amplitude modulation.

To make the path of the current loop more evident, we refer to the superposition theorem which states that the electrical response of linear systems equals to the sum of the responses caused by each independent source acting alone, where the voltage sources are replaced by a short circuit and the current sources by an open circuit (or by their internal impedance in the non-ideal case). By considering the effect of one type I current source, the path between the guard electrode of the master sensor and the com. wire is thus short-circuited via the voltage source v_{oa}. Consequently, any EIT current is injected in the body from its skin electrode and the current loop is closed via the skin impedance, the body, the master sensor (via the guard electrode), and the com. wire (see the j_{N+M} loop highlighted in figure 4.1).

It has to be noted that the voltage induced by the EIT currents flowing through z_{guard} is readily compensated for by the master sensor operational amplifier. Indeed, since this operational amplifier is in closed loop, the voltage difference between its inputs is controlled to zero. The voltage on z_{guard} is thus directly compensated by the voltage v_{oa}. Consequently, any EIT current can freely flow through the master sensor [19]. Note that the EIT currents are injected via the com. wire and the resulting voltages are measured with respect to the ref. wire. This way, bioimpedance measurements are not affected by the resistance of the wires.

With this architecture it is also possible to inject a current between two specific type I sensors—without any current flowing through the master sensor—by injecting two opposite currents with two chosen type I sensors. For instance, the impedance z_{body} of figure 4.1 can be measured by injecting the current j_{EIT} between the type I sensors number $N + M$ (via j_{N+M}) and $N + 1$ (via j_{N+1}). The value j_{EIT} is sent to the sensor $N + M$ and the value $-j_{EIT}$ to the sensor $N + 1$. A negative current specifies a 180° phase-shift of the bioimpedance measurement frequency with respect to a positive current. The resulting voltage on z_{body} (v_{EIT}) is measured via the difference between the voltages measured by the type V sensors 1 and N. In this context, the cooperation between the sensors is critical since the type I and the type V sensors need to work in concert to measure a targeted bioimpedance channel.

By choosing different combinations of type I and type V sensors, this fully-parallel architecture allows for multichannel bioimpedance measurement. The maximal number of linearly independent currents that can be injected between the different type I sensors is equal to M (the number of type I sensors), and the maximal number of linearly independent voltages is N (the number of type V sensors). Thus, $M \times N$ linearly independent bioimpedance measurements are possible. While most classical EIT systems sequentially select the current channels via time multiplexing, the approach chosen in this work uses frequency-division multiplexing to differentiate the M current channels. The next subsection describes this approach.
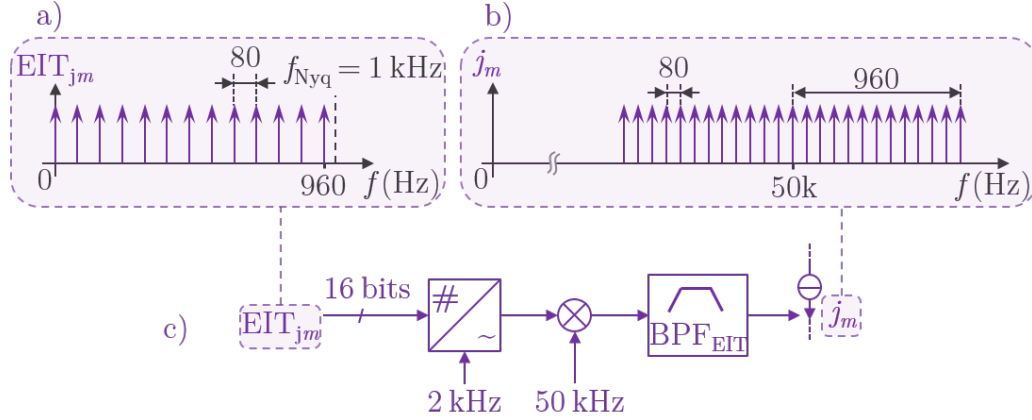
Figure 4.3 – Current injection with the frequency-division multiplexing approach: a) baseband frequency spectrum of the mth type I sensor with 25 orthogonal subcarriers, b) frequency spectrum of the current j_m injected by the mth type I sensor, and c) block diagram of the mth type I sensor.

4.1.3 Current Injection Approach via Frequency-Division Multiplexing

The fully-parallel current-injection architecture together with a frequency-division multiplexing approach are used to differentiate the M current channels. In the following, we will consider a system with 25 type V and 25 type I sensors (i.e., $N = M = 25$). Orthogonal subcarriers in a baseband frequency are generated as $\text{EIT}_{\text{j}m}$ (see figure 4.3a), where $\text{EIT}_{\text{j}m}$ sets the current amplitude of the mth type I sensor ($m \in \{N+1, \ldots, N+M\}$). The first subcarrier is at $0\,\text{Hz}$ (DC signal), and the 12 other subcarriers are set from 80 to $960\,\text{Hz}$, with a frequency spacing f_0 of $80\,\text{Hz}$ between two successive subcarriers. Each baseband modulation subcarrier can be generated in both cosine and sine wave (except for the first subcarrier at DC). The maximal number of orthogonal subcarriers is thus 25 ($= 12 \times 2 + 1$). The amplitude of the mth current ($\text{EIT}_{\text{j}m}$) can also be expressed as a trigonometric function according to equation 4.1:

$$\text{EIT}_{\text{j}m} = a_0 + \sum_{k=1}^{12} \left(a_k \cos k 2\pi f_0 t + b_k \sin k 2\pi f_0 t \right) \tag{4.1}$$

where a_k and b_k are the amplitudes of the kth cosine and sine subcarriers, respectively (with $k \in \{1, \ldots, 12\}$), a_0 is the amplitude of the DC subcarrier, and t is time. In this case, a minimal sampling frequency of $2\,\text{kHz}$ is required to have all subcarriers shown in figure 4.3a below the Nyquist frequency ($f_{\text{Nyq}} = 1\,\text{kHz}$). The $\text{EIT}_{\text{j}m}$ signal is then modulated at $50\,\text{kHz}$ to shift the baseband frequency spectrum to a range around the carrier frequency. Figure 4.3b shows that the frequency spectrum of the current j_m injected in the body by the mth type I sensor is comprised between $49.04\,\text{kHz}$ and $50.96\,\text{kHz}$ (i.e., $50\,\text{kHz} \pm 960\,\text{Hz}$).
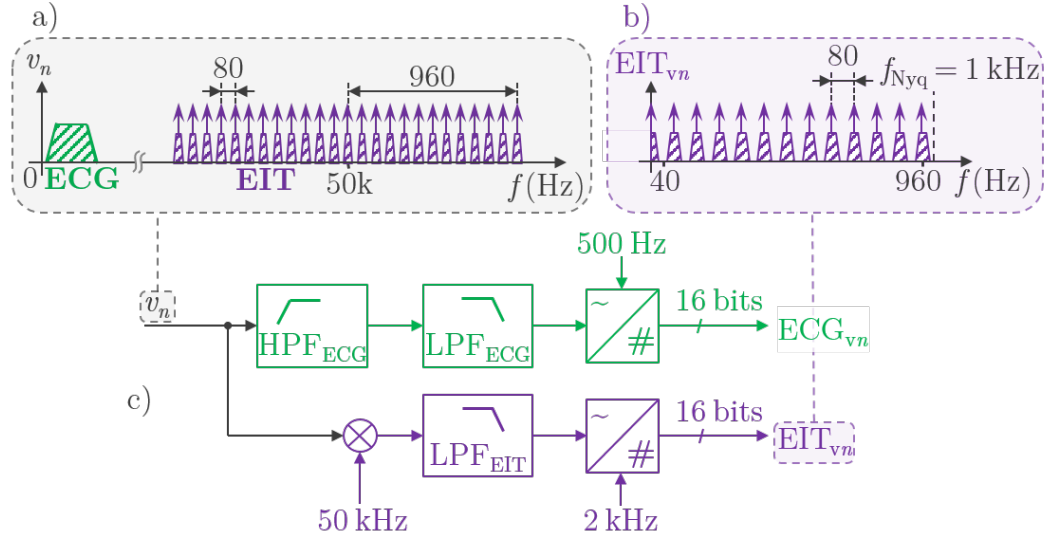
Figure 4.4 – Voltage measurement with the frequency-division multiplexing approach: a) frequency spectrum of the voltage v_n measured by the nth type V sensor, b) frequency spectrum of the demodulated EIT signal $\text{EIT}_{\text{v}n}$ measured by the nth type V sensor, and c) block diagram of the nth type V sensor.

The frequency-division multiplexing block diagram shown in figure 4.3c is implemented in each type I sensor. To have a flexible and reconfigurable system, the amplitude of the current j_m is controlled by the setpoint value $\text{EIT}_{\text{j}m}$ sent by the master sensor via the communication bus and refreshed at 2 kHz via a 16-bit digital-to-analog converter (DAC). The DAC output is then modulated by a 50 kHz square wave signal. To attenuate the harmonics magnitude, the signal is bandpass-filtered around 50 kHz (second-order analog filter) by BPF_{EIT} before being converted to a current and injected in the body as j_m. In the current implementation, the maximal root mean square (rms) amplitude of j_m is 159 µA (450 µA peak-to-peak).

4.1.4 Voltage Measurement Approach via Frequency-Division Multiplexing

Figure 4.4a shows the frequency spectrum of the voltage v_n measured by the nth type V sensor ($n \in \{1, \ldots, N\}$). This voltage is composed of the ECG signal (at lower frequencies), and the EIT signal (around 50 kHz). The signal envelope around each EIT subcarrier is due to bioimpedance variations over time. In the thorax, the impedance varies mainly due to respiration (10 to 40 breaths per minute), and cardiosynchronous activity (30 to 200 heartbeats per minute). The resulting EIT signal measured at v_n is the convolution product between the injected current spectrum (see j_m in figure 4.3b) and the frequency spectrum of the bioimpedance variations. The signal v_n is demodulated before digitization to shift the EIT signal to lower frequencies. The frequency spectrum of the digitized signal $\text{EIT}_{\text{v}n}$ is shown in figure 4.4b. Its sampling frequency must be at least 2 kHz so that all subcarriers are below the Nyquist frequency f_{Nyq}.

Figure 4.4c illustrates the function of the nth type V sensor. The ECG signal is filtered by a first-order high-pass filter (HPF$_{\text{ECG}}$) at 0.05 Hz followed by a second-order low-pass filter (LPF$_{\text{ECG}}$) at 150 Hz. The purpose of these filters is to comply with the international standard for diagnostic ECG monitoring [51], and also to properly filter out the 50 kHz signal induced by EIT circuits. The ECG signal is then digitized at 500 samples/s by a 16-bit analog-to-digital converter (ADC). Regarding the EIT signal, the voltage v_n is demodulated by a 50 kHz square wave signal, low-pass filtered at 1 kHz (LPF$_{\text{EIT}}$), and digitized by a 16-bit ADC at 2000 samples/s.

In this design, bioimpedance variations of more than 40 Hz (half of the distance between two successive subcarriers) would induce crosstalk between nearby subcarriers. However, only low-frequency bioimpedance variations are expected physiologically. In a context where faster impedance variations are expected, the distance between subcarriers can be increased, by increasing the sampling frequency or reducing the number of subcarriers.

After EIT$_{\text{v}n}$ digitalization, the 25 baseband subcarriers are isolated by digital processing. The EIT$_{\text{v}n}$ signal is demodulated over a period of 12.5 ms (= 1/80 Hz) by multiplication of EIT$_{\text{v}n}$ by a cosine (or sine) wave corresponding to the subcarrier frequency (80 to 960 Hz as depicted in figure 4.4b). Then the digitally demodulated signals are averaged by an antialiasing filter over this 12.5 ms period (corresponding to 25 samples at 2 kHz) and down-sampled at 80 Hz. Consequently, the image frame rate of the EIT system is 80 Hz.

4.1.5   Communication Protocol

A communication protocol was defined in subsection 3.3.3 for a total of 25 type V sensors. To comply with the enhanced cooperative-sensor architecture, this protocol is extended to 25 additional type I sensors. Each type V and type I sensor receives data sent from the master sensor at a rate of 2 Mbit/s. For the communication from the type V sensors to the master sensor, each type V sensor has a predefined time slot of 20 µs, i.e., every 500 µs each type V sensor can transmit 5 bytes to the master sensor.

In the current implementation of the protocol, the setpoint values of the type I sensors (EIT$_{\text{j}1}$ to EIT$_{\text{j}25}$) are sent at a rate of 2 kHz. Data are sequentially transmitted via the communication bus and the DAC output of every type I sensor is synchronously updated at the end of each communication frame (see "DAC & ADC sync. signal" in figure 4.5). In order to have a simultaneous sampling time in every type V sensor, each ADC samples and holds its corresponding analog signal (v_1 to v_N) synchronously with the "DAC & ADC sync. signal". The sampled values are then digitized and sequentially sent to the master sensor.

4.1.6   Electrical Circuits for Battery Charging

With the proposed cooperative-sensor architecture, one battery per sensor is required. Figure 4.6 shows the electrical circuit used to recharge the battery of the master sensor. Similar circuits are used to recharge the batteries of the type I and type V sensors. As shown for the
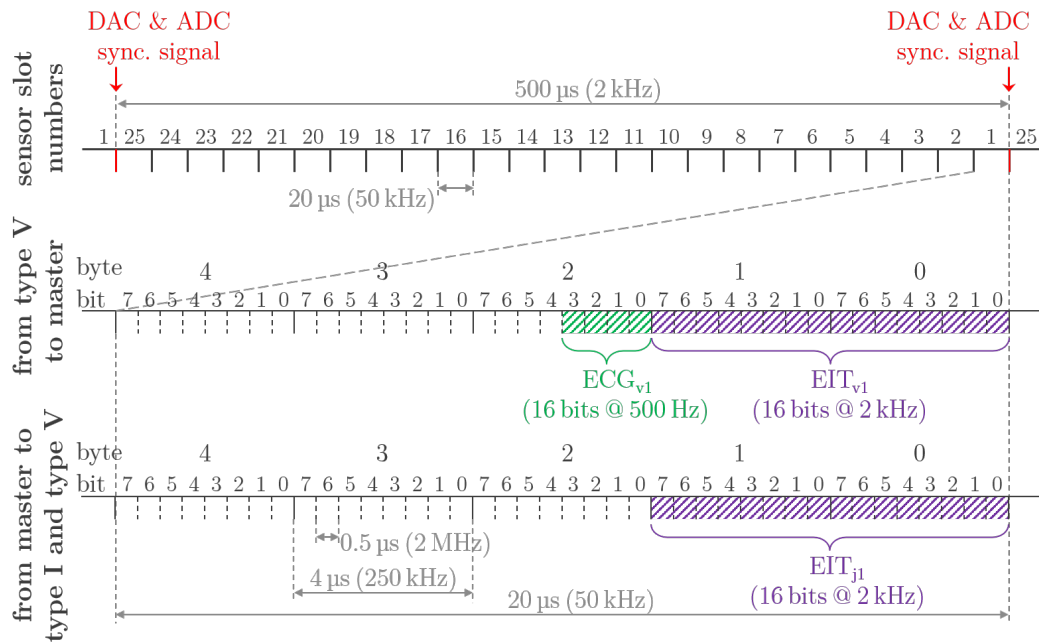
Figure 4.5 – Communication protocol for EIT and ECG measurement. The upper part shows the 25 predefined 20 µs time slots corresponding to the slots of the 25 sensors. The middle and lower parts represent the data transferred via the communication bus.

master sensor, the battery is recharged by applying a voltage u_{ext} between the snaps buttons corresponding to the ref. and com. wires. Thanks to the diode rectifier implemented with the diodes D_1 to D_4, a positive voltage is seen at the input of the battery charger (independently of the u_{ext} polarity). The battery charger is based on a BQ24232 (Texas Instruments, Dallas, United States) and its operating voltage is defined between 4.35 and 10.2 V.

It has to be noted that all sensors can be recharged in parallel by applying a voltage u_{ext} between the ref. and com. wires. To avoid any safety issue (cf. [50]), the sensor system shall be removed from the skin before applying the external voltage u_{ext}.

Regarding to the electronic circuit protections, when the voltage u_{ext} is applied between the ref. and com. wires, an important voltage (i.e., in the range of 10 V) is seen by the electronic circuits used to generate u_{sync} and to sense i_{com} (see figure 4.6). Consequently, the inputs and outputs of the electronic circuits exposed to this relatively high voltage must be protected during the charging process, for instance with a serial resistor. During a measurement (i.e., while the sensors are not charging), the diode D_5 is used to polarize diodes D_2 and D_4 in their blocking state. This way, the battery charging circuit does not influence the sensing circuit.

4.2 Testing Hardware

This section describes the hardware developed for calibrating and testing of the system.
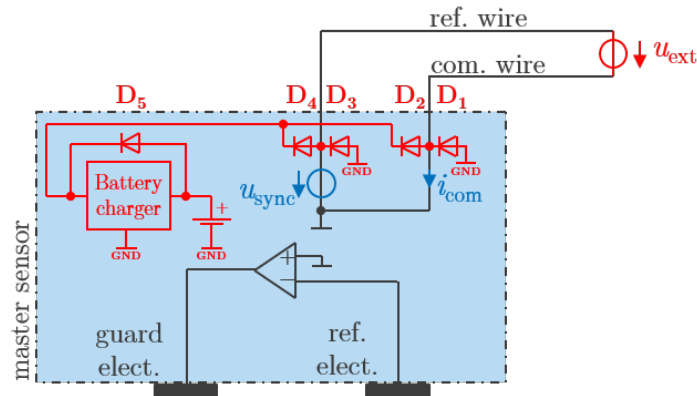
Figure 4.6 – Electrical circuit used to recharge the battery of the master sensor. The diodes D_1 to D_4 implement a rectifier for the external voltage u_{ext} to apply a positive voltage at the input of the battery charger. The diode D_5 is used to polarize diodes D_2 and D_4 in their blocking state during a measurement (i.e., while the sensor is not charging).

4.2.1   Integration of Sensors

Figure 4.7 (left) shows the embodiment of the master sensor, with two contacts with the skin, implemented as a central pad for the ref. electrode and an external ring for the guard electrode. The ref. and com. wires are connected via two snap buttons placed on the back of the sensor. The master sensor has additional sensing functionalities[1], for measuring body movements via a 3D accelerometer, and the blood oxygen saturation (SpO_2) via an optical system [21, 98]. In contrast to the master sensor, the type V and type I sensors only have one contact with the skin (see the right of figure 4.7), which makes their packaging simpler. The connections to the ref. and com. wires are also implemented via snap buttons. Each measuring sensor contains a 100 mAh coin-type lithium-ion battery and the master sensor a 600 mAh lithium-polymer battery, allowing for a continuous recording during for at least 12 h (wireless communication modules disabled).

4.2.2   Calibration Test Bench

Figure 4.8 shows a tailor-made calibration test bench allowing to connect up to 32 cooperative sensors to a resistor mesh network. The ref. and com. wires are implemented as two copper tracks routed on the printed circuit boards (PCBs) and link all sensors in a bus configuration via their snap buttons. The skin electrodes are connected to the central resistor mesh network via additional PCBs placed on the top of each sensor. The resistor mesh network placed in the center of the test bench can be adapted depending on the values to be tested.

---

[1]Although the monitoring of these additional body signals is meaningful in the context of chronic diseases, their description is beyond the scope of this thesis. The interested reader can refer to [21, 98] for more information.

Figure 4.7 – Integration of the master sensor (left) and the type V sensor (right).
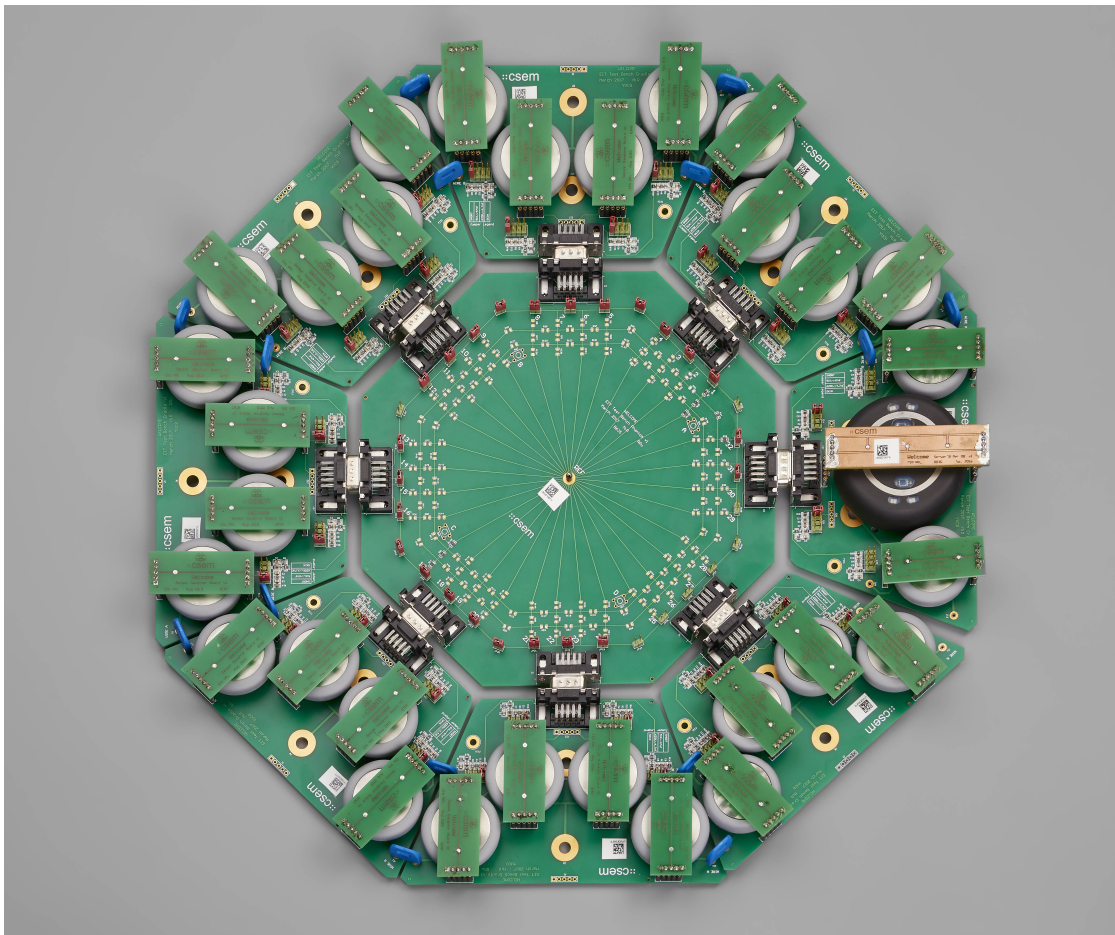
Figure 4.8 – Calibration test bench allowing for different configuration tests with up to 32 cooperative sensors. The central resistor mesh network can be adapted depending on the values to be tested.

4.2.3 Integration of the System in a Vest

The proposed system was integrated in a vest (see figure 4.9). The 8 type V and 8 type I sensors are distributed equidistantly on one transverse plane and connected to an elastic belt ensuring a tight fit and thus a good contact with the skin. The master sensor is placed above the belt on the right ventral part of the thorax. All sensors are attached using their two snap buttons. The ref. and com. wires are two unshielded wires integrated in the textile of the vest and soldered to their respective snap buttons. The system includes four additional type V sensors placed in the infraclavicular regions to measure additional ECG leads. More type V sensors may be added (for instance midway between the costal margin and the iliac crest) to measure additional ECG leads according to the Mason-Likar electrode placement [91].

For ease of use, the sensors automatically turn on when they contact the skin, thus a measurement starts when the patient puts on the vest. Continuous measurements are then performed until the patient takes off the vest. During a measurement, data are stored in the master sensor and transmitted to an external unit (e.g., a computer) via Wi-Fi at the end of the measurement session. A Bluetooth low energy (BLE) module allows real-time monitoring of the measured data and system configuration.

4.2.4 Stimulation and Measurement Patterns

Different stimulation (or current-injection) patterns have been studied in the literature [5, 29, 61, 62, 113]. The present system is versatile and allows either pair-driven or trigonometric stimulation patterns. In the following, a pair-driven stimulation pattern with a skip 5 is represented—where "skip" is the number of sensors (either type I or type V) between two current-injection sensors. Figure 4.10 shows the 8 type V sensors (V_1 to V_8) and the 8 type I sensors (I_9 to I_{16}), together with a representation of the stimulation and measurement patterns. The 8 EIT currents (ch_1 to ch_8) are simultaneously injected in the body via the frequency-division multiplexing method described in subsection 4.1.3. The subcarriers of the 8 channels are set from 80 Hz (for ch_1) to 640 Hz (for ch_8) and are uniformly distributed every 80 Hz for the other channels. For instance, the type I sensor #10 (see I_{10} in figure 4.10) simultaneously injects a current in both ch_1 (80 Hz subcarrier) and ch_4 (320 Hz subcarrier). The current of each channel has an rms amplitude of 50 μA.

Providing a simultaneous use of 8 orthogonal current channels, the total auxiliary current used for this pattern is equal to 141 μA (= $\sqrt{8} \times 50$ μA, rms value). The maximum current accepted by the IEC 60601–1 standard at 50 kHz in normal condition is 500 μA (or 5 mA depending on the type of applied part, c.f. [50]). Therefore, we have a safety margin factor exceeding 3.5.

Note that in normal use, all EIT currents flow between the type I sensors only (i.e., no desired current flows through the master sensor). This is easily understood with the superposition theorem, since there is always a type I sensor to inject the current of one channel and another type I sensor to drain (= negative injection) the current of the same channel.

Figure 4.9 – Wearable EIT system integrated in a vest with the master sensor (black), the type V sensors (orange), and the type I sensors (grey).
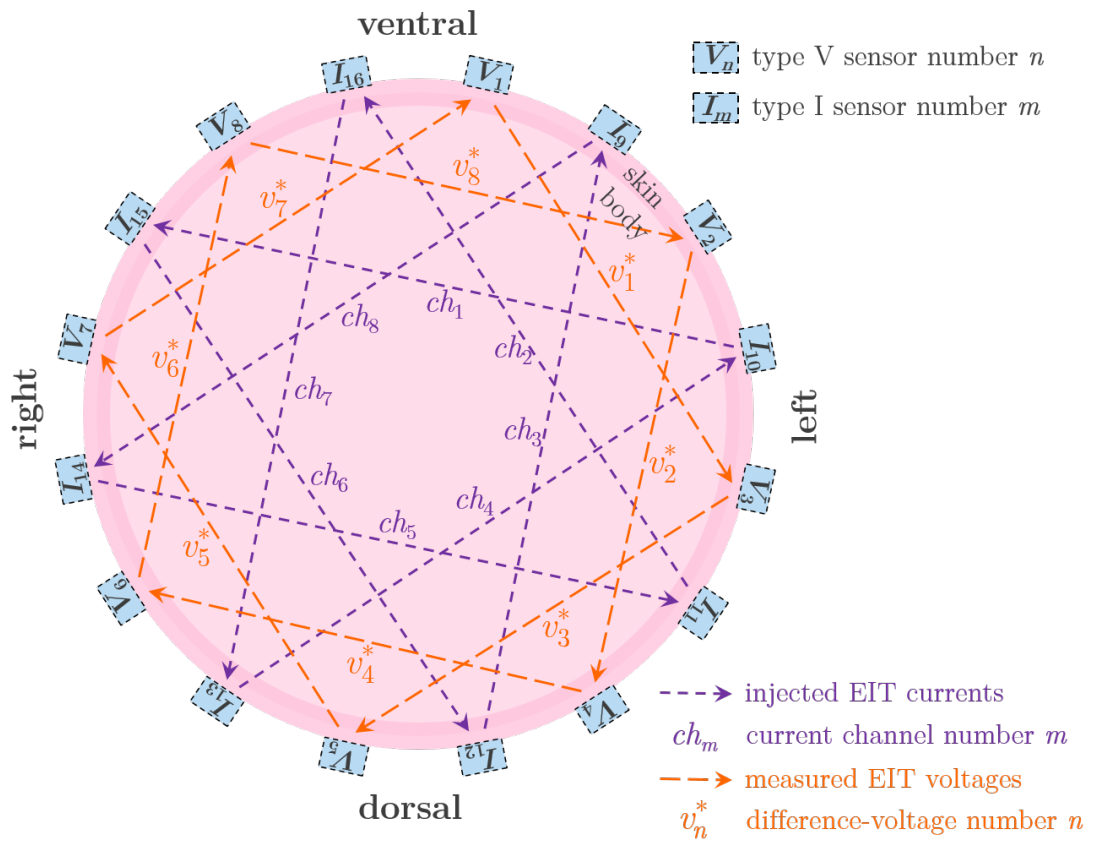
Figure 4.10 – Two-dimensional representation of the EIT stimulation and measurement patterns. Here, V_1 to V_8 are the 8 type V sensors and I_9 to I_{16} the 8 type I sensors. The 8 current-injection channels are represented by ch_1 to ch_8, and the 8 difference-voltage measurements by v_1^* to v_8^*.

The voltages v_1 to v_8 are measured by type V sensors V_1 to V_8 with respect to the same common analog reference potential (the ref. wire). This potential depends on the master sensor placement. To make the measurement independent from the master sensor, voltage measurements (v_1 to v_8) are transformed into difference-voltage measurements v_1^* to v_8^*, where $v_1^* = v_1 - v_3, v_2^* = v_2 - v_4, \ldots, v_8^* = v_8 - v_2$. This transformation is illustrated in figure 4.10 and corresponds to a pair-driven measurement pattern with a skip 3. The system allows a flexible selection of different stimulation and measurement patterns, illustrated by the use of skip 5 for the stimulation pattern, and skip 3 for the measurement pattern. With this configuration, each difference-voltage (v_1^* to v_8^*) measures the contribution of each current-injection channel (ch_1 to ch_8) resulting in 64 ($= 8 \times 8$) independent bioimpedance measurements.

4.2.5 EIT Image Reconstruction

Using the 64 bioimpedance measurements, time-difference EIT images were reconstructed. The bioimpedance measurements are concatenated into a 64×1 vector $\mathbf{v}$, which is sampled at the sampling rate. Thus $\mathbf{v}_k$ is the measurement vector at sample k. Time-difference EIT requires the selection of a reference measurement $\mathbf{v}_{ref}$, which is an averaged $\mathbf{v}$ during a physiologically relevant period, such as end-expiration. Image reconstruction is then performed using the GREIT algorithm [4] using the 2.5D model of an adult human thorax available in the EIDORS toolbox [3]. The algorithm is configured to use the pair-driven stimulation and measurement patterns shown in figure 4.10, and the recommended settings: noise figure = 0.5 , and uniformly distributed small (0.03) training targets. At each sample, k, an image $\mathbf{x}_k$ is reconstructed from the difference voltage $\mathbf{v}_k - \mathbf{v}_{ref}$, and this image projected onto a 32×32 pixels grid.

4.3 Testing Procedures and Results

This section presents the testing procedures and results obtained with the hardware described in section 4.2 to 1) calibrate the EIT system, 2) assess the noise performance of the impedance measurement, and 3) perform tests on a healthy volunteer.

4.3.1 Calibration of the EIT System

Calibration aims at measuring and correcting the mismatch between the current sources (j_9 to j_{16}) and between the voltage measurements (v_1 to v_8). Using the circuit of figure 4.11, each type I sensor sequentially injects a current in each of the 25 subcarriers (see figure 4.3a), resulting in 200 different injected currents (8 type I sensors × 25 subcarriers). Consequently, each current sequentially flows via the calibration resistor R_{cal}, and the resulting voltage is simultaneously measured by each type V sensor and in each measurement channel, resulting in 200 voltage measurements per injected current (8 type V sensors × 25 channels). The total number of measurements is 40 000 (200 currents × 200 voltages). A baseline measurement
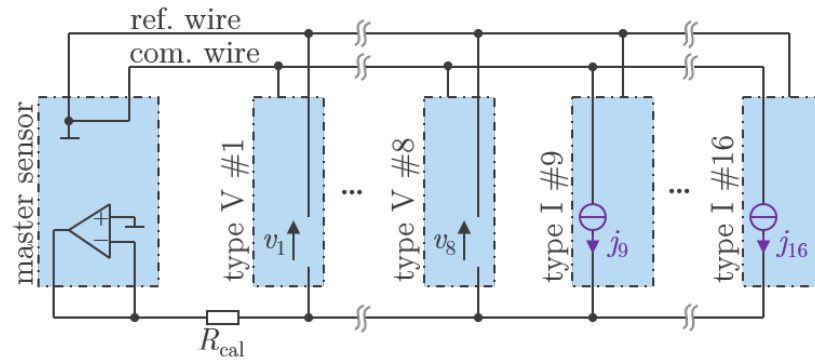
Figure 4.11 – Circuit used for the calibration procedure with the master sensor, 8 type V, and 8 type I sensors. The currents injected by the type I sensors (j_9 to j_{16}) flow through the calibration resistor ($R_{cal} = 150\,\Omega$) and the resulting voltage is measured by the type V sensors as v_1 to v_8.

without any current is also performed to measure the analog chain offset of the type V sensors.

From these measurements, four correction matrices are computed: 1) the offset correction matrix, allowing for type V analog chain offset compensation, 2) the type I gain correction matrix, allowing for type I gain mismatch compensation, 3) the type V gain correction matrix, allowing for type V gain mismatch compensation, and 4) the type V crosstalk correction matrix, which allows to compensate the crosstalk between two subcarriers which are at the same baseband frequency (e.g., crosstalk of the 80 Hz sine subcarrier in the 80 Hz cosine measurement channel, and vice versa).

Once the four correction matrices computed, two more measurements were performed with the test setup of figure 4.11. The first one consists of a simultaneous injection of 8 currents via 8 different subcarriers (one per type I sensor injected as j_9 to j_{16}). These subcarriers are set at the first four baseband frequencies (i.e., 80, 160, 240, and 320 Hz) and in the sine and cosine channels. The second measurement consists of a current injection with the same channels, but with the current injection correction (i.e., with the type I gain correction matrix). These two measurements allow evaluating the performance of the calibration procedure in a situation close to the final system setup (i.e., 8 current injection channels injected at the same time, cf. figure 4.10).

Figure 4.12 shows the calibration results. Since each channel is injected by a different type I sensor, any gain error on a type I sensor can directly be observed. As an illustration, the red diamonds show that measurements made with the type I sensor number 13 render too high impedance values, meaning that the gain of this type I sensor should be reduced. The blue circles illustrate the results of the type I calibration. The 8 values measured for each type I sensor correspond to the measurements made by the 8 type V sensors. The mismatch between these type V sensors can also be compensated, and green crosses show that the absolute measurement accuracy after both type I and type V mismatch corrections is $150\,\Omega\pm0.67\,\%$.
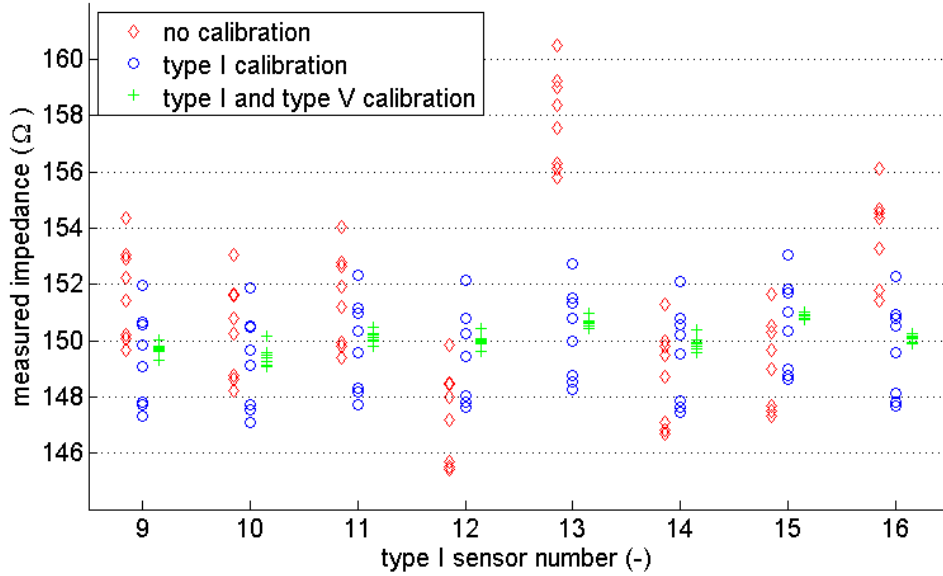
Figure 4.12 – Results of the calibration procedure showing the impedances measured with currents injected with the 8 type I sensors (j_9 to j_{16}). For each configuration, the values measured by the 8 type V sensors are shown. Red diamonds represent the initial measurement (no calibration), blue circles show measurements with the type I calibration only, and green crosses show measurements with type I and type V calibration.

4.3.2 Impedance Noise Performance Assessment

Many EIT systems define their noise performance via the signal-to-noise ratio (SNR) which corresponds to the mean value of a measured bioimpedance channel divided by its standard deviation (std), as $\text{SNR}[x] = \text{mean}[x]/\text{std}[x]$ [16]. However, the SNR not only depends on the hardware performance, but also on the chosen stimulation and measurement patterns [5]. Here, we used the test bench shown in figure 4.13 to focus on the assessment of the electronic circuits (i.e., the current sources and the voltage measurements). The setup contains one master sensor, two current injecting (type I) sensors, and two voltage measuring (type V) sensors. In each measurement, a current of 50 µA (rms value) is injected between the type I sensor #1 (via j_1) and the type I sensor #2 (via j_2). This current flows through the calibration resistor R_{cal} and the resulting voltage is measured by computing the difference between the voltages measured at v_1 and v_2 (measured in the type V sensors #1 and #2). For this measurement, R_{cal} is set to three different values: 0 Ω (short circuit), 75 Ω, and 150 Ω.

Figure 4.14 shows a typical impedance measurement (with $R_{\text{cal}} = 150\,\Omega$) during a 10 s period. The maximal peak-to-peak noise is 51.9 mΩ and the standard deviation over the same period is 8.73 mΩ. It has to be noted that the bandwidth of the impedance measurement goes from DC to 20 Hz (first-order filter).

Table 4.1 shows the absolute value, the peak-to-peak noise, and the standard deviation mea-
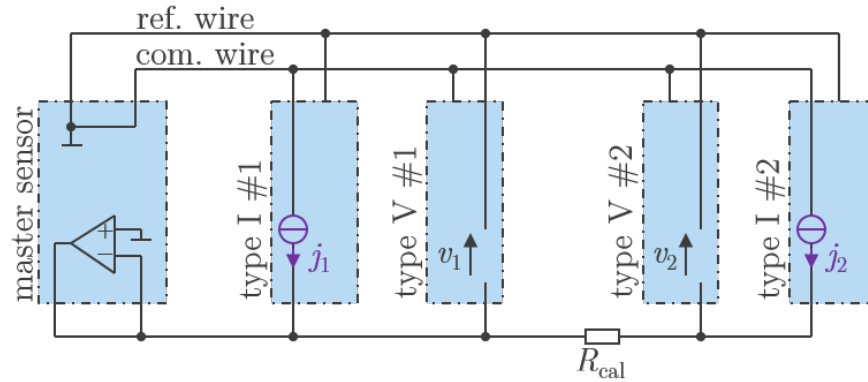
Figure 4.13 – Circuit used for noise performance assessment with the master sensor, two type V, and two type I sensors. A current is injected between the two type I sensors and the resulting voltage on the calibration resistor R_{cal} is measured between the two type V sensors.
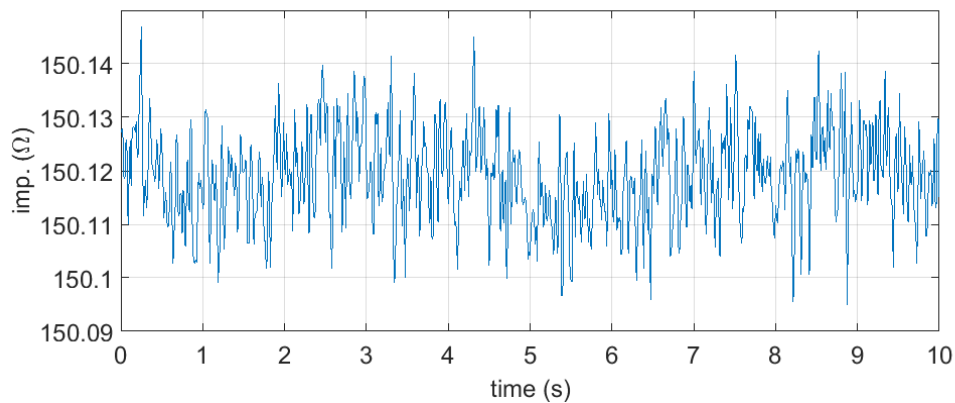
Figure 4.14 – Noise of the cooperative-sensor system measured on a $150\,\Omega$ calibration resistor.

sured for the three values of R_{cal}. The measured noise does not significantly depend on R_{cal}. Therefore, the noise primarily comes from the voltage measurement of the type V sensors.

4.3.3   Experimental Protocol and Tests on a Healthy Volunteer

The goal of this experimental protocol is to verify the feasibility of simultaneously measuring multilead ECG and multichannel bioimpedance for EIT image reconstruction with the cooperative-sensor system. To that end, the hardware described in section 4.2 was tested on a healthy male subject. The subject put on the vest shown in figure 4.9, and then lay in supine position during five minutes. Next, he underwent a protocol of four steps: 1) resting period (normal quiet breathing), 2) inspiratory apnea, 3) four normal breathing cycles, and 4) four deep breathing cycles. Next, the subject removed the vest and data were wirelessly transmitted to a computer for further processing.

Table 4.1 – Absolute value, peak-to-peak noise, and standard deviation measured on three different values of the calibration resistor R_{cal}.

R_{cal} value (Ω)	measured value (Ω)	peak-to-peak noise (mΩ)	standard deviation (mΩ)
0	0.0388	56.9	8.84
75	75.75	48.7	8.58
150	150.12	51.9	8.73

Figure 4.15a shows 8 raw bioimpedance signals measured during this testing procedure. Figure 4.15b shows one ECG lead and one raw bioimpedance signal measured by injecting the EIT current in ch_4 and measuring the resulting voltage on v_8^* ($v_8^* = v_8 - v_2$, see the stimulation and measurement patterns in figure 4.10). Figure 4.15c shows EIT images resulting from ventilation-related impedance changes during a normal breathing cycle, and Figure 4.15d shows heartbeat-related EIT signals obtained via ECG-gated ensemble averaging during 75 s in the initial normal breathing period (79 heartbeats).

4.4 Discussion

This chapter presents a wearable and easy-to-use system for fully-parallel EIT and synchronous multilead ECG measurement. The system was designed by extending the dry-electrode cooperative-sensor architecture presented in chapter 3 with multichannel bioimpedance measurement capabilities. The fully-parallel EIT measurement structure avoids the use of multiplexers by the application of multiple current sources (one per type I sensor) and multiple voltage measurements (one per type V sensor) and allows for flexible and adjustable stimulation and measurement patterns via a frequency-division multiplexing approach.

The matching between the sensors was measured on a calibration test bench with an accuracy (after correction) of 150 Ω±0.67 %. The assessment of the noise performance of the cooperative-sensor system shows that the standard deviation measured on three different resistances (0 Ω, 75 Ω, and 150 Ω) was between 8.58 mΩ and 8.84 mΩ (with a measurement bandwidth between DC and 20 Hz). Since the noise is essentially the same for all resistance values, it mainly comes from the voltage-measurement (type V) sensors. Therefore, the global system performance can be enhanced by further improving the type V sensor electronics. It has to be noted that for many EIT applications, the required bandwidth can be reduced, resulting in reduced noise amplitude.

Examples of raw bioimpedance signals measured with the proposed wearable system are shown in figure 4.15a. In the normal breathing phase, tidal breathing is clearly visible, whereas heartbeat-related variations are more pronounced during the apnea period. As expected, bioimpedance variations during deep breathing are larger than during quiet breathing. Figure 4.15b shows an example of synchronous acquisition of both bioimpedance and ECG
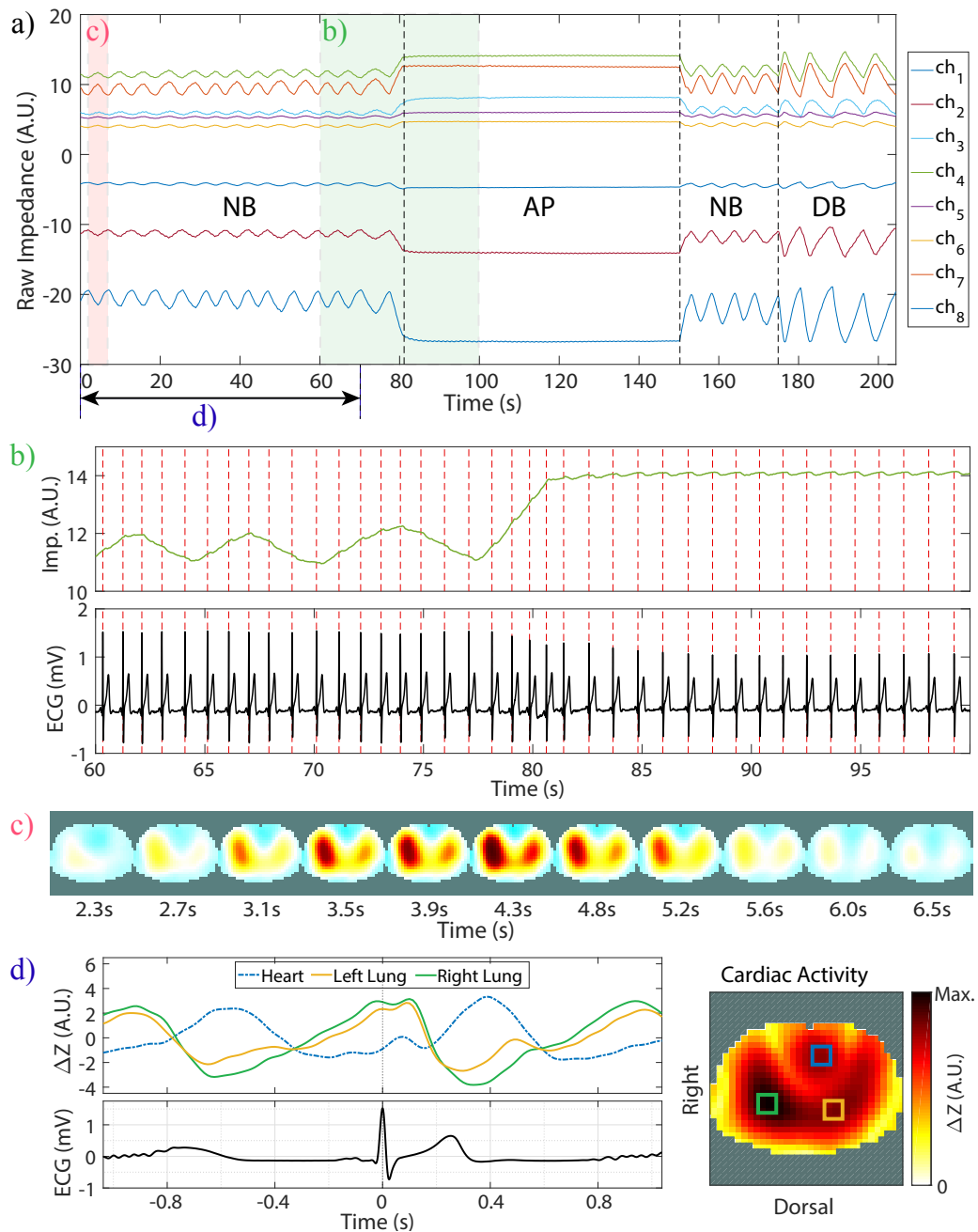
Figure 4.15 – EIT signals and data from a subject: a) the 8 raw signals measured on v_8^* for the current channels ch_1 to ch_8 (**NB** normal breathing; **AP** inspiratory apnea; **DB** deep breathing). b) One bioimpedance channel (current injected in ch_4 and voltage measured on v_8^*) and one ECG lead (measured between sensors V_6 and V_2) displayed with the red vertical lines indicating the ECG R-peak locations. c) Reconstructed EIT images during one representative normal breathing cycle (these images are relative to the start of inspiration). d) Heartbeat-related EIT signals obtained via ECG-gating during the initial normal breathing period. The image in the right represents heartbeat-related activity (by means of the temporal standard-deviation) during the averaged cardiac cycles. The signals on the top left represent the temporal bioimpedance change in the heart (blue), right lung (green), and left lung (orange) regions during two averaged cardiac cycles. The signal in the bottom left is the averaged ECG.

signals, underpinning the correlation between heartbeat-related bioimpedance variations and the ECG signal. The EIT images in figure 4.15c show that the signal intensity in the left lung is lower than in the right lung. This behavior is in line with anatomy (i.e., the left lung has a smaller volume than the right lung). From the ECG-gated images of figure 4.15d, the signal in the heart region (blue) is in opposite phase with respect to the signals in the lung regions (green and orange). More specifically, shortly after the ECG R-peak, the impedance decreases in the lung regions and increases in the heart region, which is consistent with previous observations [72, 79].

In the current implementation of the system, only the type V sensors are equipped with full-duplex communication capabilities and the type I sensors cannot send information to the master sensor. In a future implementation, equipping the type I sensors with full-duplex communication capabilities would enable these sensors to transmit helpful information such as skin-contact quality, saturation of the current source, or battery level alert.

These measurements show the ability of the proposed system to synchronously measure high-quality multilead ECG and multichannel bioimpedance signals, paving the way towards a new generation of wearable and flexible EIT systems for noninvasive cardiovascular monitoring with variable electrode position/number, versatile stimulation patterns, fully-parallel stimulations/measurements, and synchronous ECG acquisition. A first qualitative evaluation on one healthy volunteer already showed promising and physiologically meaningful results.

5 Synthesis

The aim of the present thesis was to investigate wearable solutions offering the possibility to closely monitor physiological parameters in a patient's everyday environment with a particular focus on the measurement of multilead electrocardiogram (ECG) and multichannel bioimpedance for electrical impedance tomography (EIT) imaging. To maximize the system's ease of use and to facilitate its integration in a garment, a new electrical architecture—so-called cooperative sensors—was developed and evaluated.

The main novelties of the proposed system are: 1) the electrical architecture of the system allowing for a minimal wiring complexity between sensors, 2) the simultaneous measurement of high-quality multilead ECG and multichannel bioimpedance for EIT imaging, and 3) the unswitched fully-parallel EIT measurement via frequency-division multiplexed current stimulations.

In the following, the key findings of the present thesis are further detailed. Then the limitations of the proposed system are described, and the aspects deserving further research are finally provided.

5.1 Summary of Achievements

The Cooperative-Sensor Architecture

The first main achievement of this thesis is the definition of the electrical architecture of the so-called cooperative-sensor system. When classical approaches usually require (double) shielded cables with passive electrodes (or multi-wire cables with active electrodes) in a star arrangement to acquire ECG and EIT signals of high quality, the cooperative-sensor architecture uses only one unshielded cable linking all active sensors in a bus arrangement.

This cooperative-sensor architecture significantly reduces the wiring complexity (neither shielded, nor multi-wire cable), and eliminates the presence of the central unit to which all cables classically converge. This results, without any impact on the signal quality, in systems

which are easier to integrate in wearables. The price to pay is that one power supply per sensor (e.g., a battery) is required and all sensors need to be synchronized to allow them to work in concert.

This cooperative-sensor architecture was introduced in section 3.1 (see figure 3.1) and published in [80].

Full-Duplex Body Sensor Network with Cooperative Sensors

The next achievement is related to the synchronization and communication mechanism allowing cooperative sensors to synchronously exchange information. This full-duplex communication between the sensors is provided by simply adding a second wire in parallel to the wire required for the initial architecture, allowing for a full-duplex communication at a rate of 2 Mbit/s and making it possible to gather the measured data in one single location (in the master sensor). Wires do not require to be shielded to get high-quality measurements, thus making the cabling of the measurement system simple and easy to integrate.

The synchronization mechanism and its underlying PLL are implemented in each measuring sensor (type I and type V sensors) and allow to accurately recover the frequency and phase of the master sensor clock with a measured jitter of approximately ± 15 ns.

This body sensor network (BSN) allowing for synchronization and full-duplex communication between the cooperative sensors was detailed in section 3.2 (see electrical architecture in figure 3.2) and published in [83].

Wearable 12-lead ECG Holter with Cooperative Sensors

To demonstrate the reliability of the cooperative-sensor architecture in a real-life scenario, a wearable 12-lead ECG monitoring system (an ECG Holter) was designed and compared to a gold-standard medical device. Moreover, the architecture of the master sensor was improved to facilitate its integration. Indeed, even if the cooperative-sensor architecture significantly reduces cabling complexity, it initially required the master sensor to be equipped with two contacts with the skin for proper common-mode rejection, thus making its miniaturization problematic. An alternative common-mode rejection principle was implemented with the guard and the ref. electrodes implemented in two separate sensors, each with one skin-contact only. The suggested approach was implemented in a 12-lead ECG monitoring system made of one master sensor (now with one single skin-contact), one reference sensor, and eight type V sensors. ECG signals are synchronously acquired and their digitized values are gathered in the master sensor for further processing, recording, and/or monitoring purpose.

Since the communication and the measurement share the same unshielded wires, it is required that they do not interfere with each other. Measurements on a test bench showed that the system is able to measure a voltage between two cooperative sensors with a peak-to-peak

noise of approximately $30\,\mu V$, which is in line with the requirements of international standards for ECG systems [51, 52]. Another important aspect of the developed system is the use of dry electrodes. A comparison with gold-standard medical devices (at rest and during an exercise stress test) showed that the noise level and the baseline wandering of the signal measured with the cooperative-sensor system (using dry electrodes) is similar to the one measured with the gold-standard medical devices (using gel electrodes).

The approach allowing for compensating the common-mode disturbance with one skin-contact per sensor, as well as the tests demonstrating the reliability of cooperative sensors for multilead ECG measurements were reported in section 3.3 (see electrical architecture in figure 3.11). These results have also been published in [81].

Synchronous ECG and Fully-Parallel EIT Measurement via Frequency-Division Multiplexing

A wearable and easy-to-use system for EIT and synchronous multilead ECG measurement was designed by extending the previous cooperative-sensor architecture with multichannel bioimpedance measurement capabilities. A first challenge was the integration of the EIT system in a vest. Furthermore, dry electrodes were preferred to maximize the system's ease of use. This way, the monitored patient only has to put on the vest without other inconveniences (electrodes placement, skin preparation, etc.). The fully-parallel EIT measurement architecture avoids the use of multiplexers by the simultaneous injection of multiple currents and parallel measurement of the resulting voltages, allowing for flexible and adjustable stimulation and measurement patterns via a frequency-division multiplexing approach.

The fully-parallel architecture together with a frequency-division multiplexing method were detailed and the matching between the current sources and voltage measurements was measured with a calibration test bench. The accuracy of the impedance measurement after correction is $150\,\Omega \pm 0.67\%$. Moreover, a noise performance assessment showed a standard deviation of $8.73\,m\Omega$ (measured on a $150\,\Omega$ resistor with a bandwidth limited to $20\,Hz$).

Measurements on a healthy volunteer showed the ability of the proposed system to synchronously measure multilead ECG and multichannel bioimpedance signals, paving the way towards a new generation of wearable and easy-to-use EIT/ECG systems for noninvasive cardiovascular monitoring. This first qualitative evaluation already showed promising and physiologically meaningful results.

The detailed design and performance assessment of the system (including the frequency-division multiplexing approach) were described in chapter 4 and published in [82].

Summary of the Cooperative-Sensor System Specifications

The main specifications of the cooperative-sensor systems described in subsection 3.4.4 (for ECG) and subsection 4.2.3 (for EIT) are summarized in table 5.1.

Table 5.1 – Summary of the cooperative-sensor systems specifications.

System	Specification	Value
ECG	Number of independent leads[1]	12
	Measurement bandwidth[1]	0.05 Hz (1st order) to 150 Hz (2nd order)
	Input referred noise (peak-to-peak)[2]	30 µV
	Sampling frequency[1]	500 Hz
	Measurement resolution[3]	16 bit
EIT	Nbr of voltage-sensing electrodes[4]	8
	Nbr of current-injection electrodes[4]	8
	Measurement bandwidth[5]	DC to 20 Hz (1st order)
	Measurement noise (standard dev.)[5]	< 9 mΩ
	Image frame rate[6]	80 Hz

[1] cf. subsection 3.4.4;   [2] cf. subsection 3.5.1;   [3] cf. subsection 3.3.3;
[4] cf. subsection 4.2.3;   [5] cf. subsection 4.3.2;   [6] cf. subsection 4.1.4;

Beyond ECG and EIT, the system also includes sensing functionalities for measuring body movements via a 3D accelerometer and blood oxygen saturation (SpO_2) via an optical system (cf. subsection 4.2.1).

Scientific Contributions

A list of publications related to this thesis is available in the curriculum vitae at the end of this document. The more substantial publications are listed below:

- "Cooperative Dry-Electrode Sensors for Multi-Lead Biopotential and Bioimpedance Monitoring," published in *Physiol. Meas.*, doi:10.1088/0967-3334/36/4/767, ref. [80]

- "Two-Wire Bus Combining Full Duplex Body-Sensor Network and Multilead Biopotential Measurements," published in *IEEE Trans. Biomed. Eng.*, doi:10.1109/TBME.2017.2696051, ref. [83]

- "Electromagnetic Disturbances Rejection with Single Skin Contact in the Context of ECG Measurements with Cooperative Sensors," published in *EMBC*, doi:10.1109/EMBC.2017.8037838, ref. [81]

- "Wearable Sensors for Frequency-Multiplexed EIT and Multilead ECG Data Acquisition," published in *IEEE Trans. Biomed. Eng.*, doi:10.1109/TBME.2018.2857199, ref. [82]

5.2 Limitations and Future Work

Miniaturization and Power Consumption

In the current implementation of the cooperative-sensor system, off-the-shelf discrete components were used. Consequently, the system is not fully optimized in terms of size and power consumption. The development of an application-specific integrated circuit (ASIC) would allow to improve the power consumption and to reduce the system size.

Moreover, the current communication throughput of the cooperative-sensor system (2 Mbit/s) is oversized in view of the applications proposed in this thesis, which is therefore not optimal in terms of power consumption. However, it allows adding more signals in further developments, paving the way towards more complex wearable systems requiring higher numbers of physiological signal measurements.

Number of Independent Measurements

Classical EIT image-reconstruction algorithms usually exclude measurements made with stimulation electrodes. Therefore, with the proposed fully-parallel architecture, half of the sensors (i.e., the type I sensors) are not used for image reconstruction. As a consequence, for a given number of electrodes (N_E), the number of independent measurements (N_M) is lower with the proposed approach when compared to a classical system. As an example, for a 16-sensor belt, the number of independent measurements with the proposed architecture is equal to 64 ($N_M = 8 \times 8$, cf. subsection 4.2.4). In the classical approach, however, the number of independent measurements is $^1/_2 N_E (N_E - 1)$ [2], which equals to 120 for $N_E = 16$.

Two approaches would allow increasing the number of independent measurements with the cooperative-sensor approach: 1) increasing the number of sensors, which would be possible after a significant effort in sensor miniaturization, or 2) equipping all cooperative sensors with both current injection and voltage measurement capabilities. The second strategy would however require the use of the classical time-multiplexing approach to sequentially inject each current channel (since stimulation electrodes are usually not used for measurements), therefore limiting the imaging scan rate and decreasing the measurement performance of the data acquisition system, especially for EIT signals of higher frequencies [110] (e.g., heartbeat-related signals).

Simulations with Separated Type I and Type V Sensors

Classical EIT systems use time multiplexing to select the stimulation and measurement electrodes. Consequently, the electrodes are sequentially selected and alternately used for both stimulation or measurement. With the fully-parallel EIT architecture proposed in this thesis, the stimulation (type I) and the measurement (type V) sensors are predefined and cannot be exchanged. Since the cooperative-sensor architecture is somewhat different from classical

EIT systems, simulations should be performed to evaluate the impact of this constraint on the reconstructed EIT images. Although unlikely, if the impact is significantly negative, equipping cooperative sensors with both current injection and voltage measurement capabilities, and using the classical time-multiplexing approach, would allow to get around this issue.

Tests on More Subjects

The proposed ECG/EIT measurement system was qualitatively evaluated on one single healthy volunteer to illustrate the capacity of the system to trace physiological changes associated with breathing and heart action. A systematic description of these results is beyond the scope of this thesis, which primarily describes the technical innovations of the cooperative-sensor architecture. In order to systematically analyze the detected physiological phenomena, as well as their repeatability and reliability, tests on more subjects must be performed. This has been carried out within the framework of the European Union-funded project WELCOME (http://www.welcome-project.eu) in two clinical studies on patients suffering from COPD and one study on healthy subjects [34] using the wearable system described in chapter 4.

Multi-Frequency Bioimpedance Measurement

For some EIT applications multi-frequency bioimpedance measurements are desired [7, 73]. In the current implementation of the cooperative-sensor system, bioimpedance is measured at 50 kHz only. Even though the cooperative-sensor architecture does not limit the bioimpedance measurement to this unique frequency, the lower and higher bioimpedance measurement frequencies are limited by the highest biopotential measurement frequency (i.e., 150 Hz for ECG), and the communication signal frequency (i.e., around 2 MHz), respectively. With the current implementation of the system, and assuming a bandwidth separation of one decade, a multi-frequency bioimpedance measurement between 1.5 kHz and 200 kHz is foreseeable by means of significant adaptations of the analog frontends of both the type I (to enable the current injection at different frequencies) and the type V sensors (to measure the resulting voltage at these same frequencies). It has to be noted that the complexity of the adaptations will also depends on the number of different frequencies to be measured and if these frequencies are time-multiplexed or simultaneously injected in the body.

Complex Bioimpedance Measurement

Several EIT applications also require the measurement of complex bioimpedance [53, 65]. In the current implementation of the system, only the real part is acquired. However, complex bioimpedance can be measured by adapting the analog frontend of the type V sensors with a replication of the branch used to acquire EIT_{vn} (see figure 4.4c). The resulting block diagram is shown in figure 5.1. Here, the 50 kHz square wave signal used to demodulate the v_n signal is generated once in-phase to get $\text{EIT}_{vn,\,\text{I}}$, and once in quadrature (i.e., with a 90° phase-shift) to
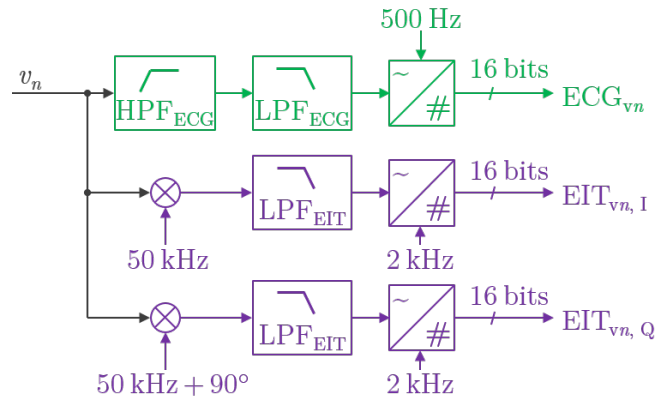
Figure 5.1 – Block diagram for complex EIT voltage measurement in the nth type V sensor. The signals $\text{EIT}_{vn,\text{I}}$ and $\text{EIT}_{vn,\text{Q}}$ represent the real (in-phase) and imaginary (quadrature) components of the measured EIT voltage.

get $\text{EIT}_{vn,\text{Q}}$. This solution however requires additional electrical circuits in each type V sensor (including an ADC), and the amount of data to be transmit to the master sensor is higher as well.

Enhanced Calibration Procedure

While the fully-parallel EIT measurement structure avoids the use of multiplexers (see figure 4.1), it requires multiple current sources (one per type I sensor) and multiple voltage measurements (one per type V sensor). Therefore, the matching between the sensors has a direct impact on the measurement accuracy.

A first calibration procedure was described and successfully tested in subsection 4.3.1. This calibration procedure can be enhanced by means of a hardware modification of the master sensor. Indeed, in the current implementation of the system, the current flowing through the master sensor is measured as i_{com} (measured in the communication bandwidth only). By measuring this current in the EIT bandwidth as well (i.e., at 50 kHz), it would be possible to measure the mismatch between the stimulation EIT currents during the measurement process. Furthermore, since the amplitude of each current is continuously sent to the type I sensors (via $\text{EIT}_{\text{j}1}$ to $\text{EIT}_{\text{j}25}$), the current mismatch could be compensated in real time, allowing for a continuous calibration of the type I sensors during the measurement process.

Another source of error that can be rectified is related to the bandpass filter used to treat the EIT signal (see BPF_{EIT} in figure 4.3c) which induces a phase shift in the 50 kHz injected current. A phase correction of the injected current is possible by replicating the branch used to modulate $\text{EIT}_{\text{j}m}$. The resulting block diagram is shown in figure 5.2. Here, a 50 kHz square wave signal (in-phase) is used to modulate $\text{EIT}_{\text{j}m,\text{I}}$, and another 50 kHz square wave signal with a 90° phase-shift (quadrature) is used to modulate $\text{EIT}_{\text{j}m,\text{Q}}$. The two modulated signals
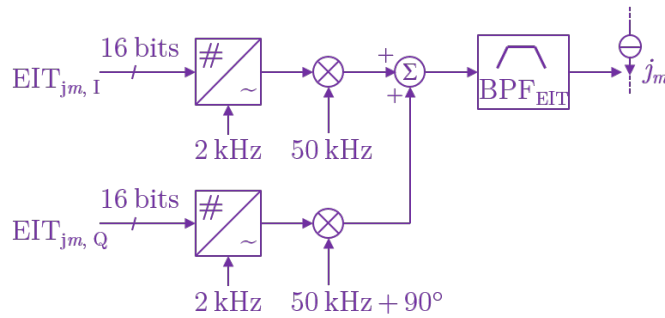
Figure 5.2 – Block diagram for complex EIT current injection in the mth type I sensor. The signals $\text{EIT}_{\text{j}m,\text{I}}$ and $\text{EIT}_{\text{j}m,\text{Q}}$ represent the real (in-phase) and imaginary (quadrature) amplitudes of the injected EIT current j_m.

are then summed and bandpass filtered before being injected in the body as j_m. This solution however requires additional electronic circuits in each type I sensor (including a DAC).

While this procedure allows compensating the mismatch between the type I sensors (in amplitude and in phase), the mismatch between the type V sensors must also be compensated to maximize the global system accuracy. In the current implementation of the system (see figure 4.1), the master sensor sends a voltage signal to all measuring (type I and type V) sensors via u_{sync}, but in the communication bandwidth only. By extending the electronic circuits of the master sensor to generate this signal in the EIT bandwidth as well, it would permit the calibration of the voltage measurements in real time during the measurement process. In this case, a common-mode calibration signal would be measured by all type V sensors as v_1 to v_N, allowing for an individual identification of the transfer function of each type V sensor.

In the same way as for the calibration of the type V sensors in the EIT bandwidth, a low-frequency calibration signal would allow identifying the transfer function of each type V sensor in the ECG bandwidth. Since these calibration signals are identically measured by all type V sensor, they are cancelled from the final signals by computing the difference between the absolute measured voltages.

The quantification of the current and voltage mismatches and the fully-automated calibration procedure is part of future work necessary to improve the global system performance. This enhanced calibration approach will not only require more electronic circuits in the master, type I, and type V sensors, but also require more processing time of the microcontroller embedded in the master sensor. Further investigations should be carried out to determine if a continuous-time calibration is foreseeable or if a sporadic calibration procedure is preferable.

Single Wire Communication with Cooperative Sensors

The reduction of the cabling complexity is one of the main features of the cooperative-sensor architecture. The current implementation (see figure 4.1) uses a two-wire bus combining
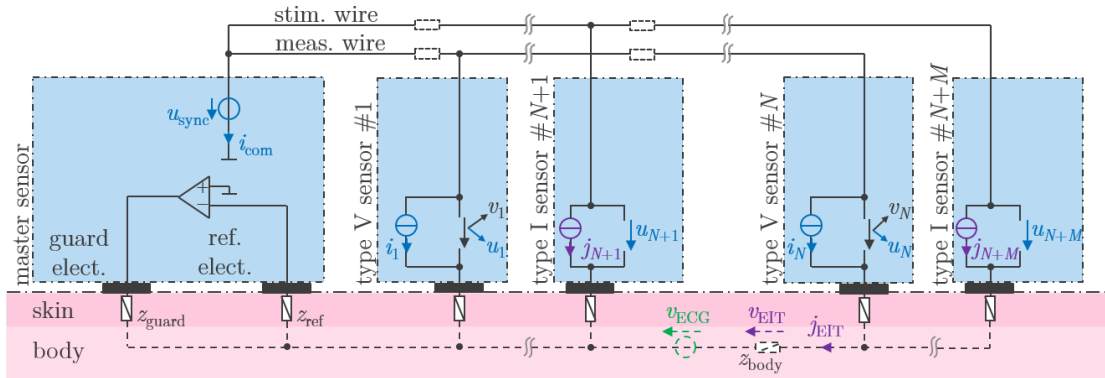
Figure 5.3 – Single wire communication between cooperative sensors. With this configuration, cooperative sensors have only one contact with the external galvanic link implemented as the stim. wire (for type I sensors), and the meas. wire (for type V sensors). The dashed resistances represents the intrinsic resistance of the wire segments.

full-duplex communication, as well as fully-parallel EIT and ECG measurement. In this configuration, the communication signal u_{sync} is broadcasted by the master sensor to all measuring (type I and type V) sensors between the two external wires.

Figure 5.3 shows an alternative architecture that may further reduce the cabling complexity of the sensor system. With this architecture, the cooperative sensors only have one connection with a unique external galvanic link. This cabling is considered as minimum, since at least one wire is required to serve as a voltage reference for ECG/EIT measurement and to convey the currents necessary for EIT. This electrical connection may however be split into two separate wires: 1) the stimulation wire (stim. wire) which links all type I sensors together, and 2) the measurement wire (meas. wire) which links all type V sensors together. The reason for the separation between the stim. and the meas. wires is that the stimulation current used for EIT measurement may induce a significant voltage drop on the intrinsic wire resistance. If this resistance is low enough to be neglected, the stim. and meas. wires can be merged.

The development of the housing is a critical challenge for the system miniaturization, especially for systems that require to be watertight. This new wiring configuration not only reduces the cabling complexity, but also significantly simplifies the sensor housing since it reduces the number of connection to two (one skin electrode and one contact to the external wire).

In opposition to the initial architecture (with the communication signal u_{sync} sent between the two external wires), the architecture proposed in figure 5.3 uses the body potential as a ground reference to transmit u_{sync}. Consequently, the cooperative sensors must be in contact with the skin to enable the communication. This communication approach is thus potentially less robust towards motion artifacts. However, since the communication works at relatively high frequencies (typically around 2 MHz), a capacitive coupling with the body might be sufficient. Practical tests must be performed to further validate this conceptual approach.

Cooperative Sensors Architecture with One Centralized Battery

In the current implementation of the cooperative-sensor architecture (see figure 4.1), one battery per sensor is required, limiting the system integration and miniaturization. Moreover, the batteries also limit the autonomy of the sensor system and require to be regularly recharged. Supplying the measuring (type I and type V) sensors via the ref. and com. wires is thus desirable. That way, the master sensor would be the only sensor to have a battery and every measuring sensor would have voltage controllers to generate their local supply voltages.

To supply the measuring sensors, the master sensor has to apply a significant voltage (typically 2 or 3 V) between the two external wires. This can be an issue since the device shall be safe according to international standard IEC 60601–1 [50], even if soaked with sweat. In particular, any leakage current over the maximum allowed current for type CF (i.e., 10 µA) shall be detected and the device shall be switched off in safe mode.

A possible strategy to actively check that such low leakage current is not exceeded is to control the current consumption of every measuring sensors to a constant value. The idea is that the master sensor can then make a change of the power-supply voltage via a superimposed frequency and check if this results in an alternating leakage current. As all sensors have a constant current consumption, if there is an alternating current, it cannot be something else than a leakage current flowing, in the worst case, through the body.

Another advantage to control the consumption current to a constant value is related to the voltage drop on the ref. and meas. wires. Indeed, the supply current will induce voltage drops on the intrinsic resistances of the wires, and any variation of this supply current may induce a significant variation on the voltage measured by the type V sensors. This constant supply current strategy is thus advantageous to limit the disturbance on the measured voltages. Here as well, practical tests must be performed to further validate this conceptual approach.

5.3 Conclusion

In conclusion, the present thesis investigated a novel electrical architecture, called cooperative sensors, offering the possibility to closely monitor multilead ECG and multichannel bioimpedance with a wearable and easy-to-use system. This system is intended to be used for remote continuous telemonitoring, and can enable novel clinical strategies for patients suffering from chronic diseases (such as CHF, COPD, or poorly controlled hypertension). The developed system is highly integrated to monitor patients' vital signs during their daily life with minimal inconvenience (the sensors are integrated in a vest with dry electrodes).

The cooperative-sensor system showed its ability to measure multilead ECG and multichannel bioimpedance for EIT imaging, paving the way towards a new generation of wearable EIT systems for noninvasive cardiovascular monitoring with variable electrode position/number, versatile stimulation/measurement patterns, fully-parallel stimulations/measurements, and

synchronous high-quality multilead ECG measurement. A first qualitative evaluation on one human subject already showed promising and physiologically meaningful results.

In future, the newly-developed system can be substantially improved by implementing the hardware changes proposed in section 5.2 in paragraphs *Enhanced Calibration Procedure* and *Complex Bioimpedance Measurement*. Especially, a mechanism shall be implemented to send a calibration signal from the master sensor enabling a continuous and automatic calibration procedure. These hardware changes would also enable the measurement of complex bioimpedance which is desirable for some EIT applications.

Another promising research direction to be further investigated is the application of the cooperative sensor technology for ECG imaging via body surface potential mapping [36, 87, 111]. This application requires a large number of sensors (typically more than a hundred) measuring each one ECG lead. Here, the simplified cabling of the cooperative-sensor architecture is a clear advantage for the integration of such a system. Moreover, since each sensor only has to measure a single biopotential, it will consume less power. For such an approach, the use of one centralized battery (see section 5.2, paragraph *Cooperative Sensors Architecture with One Centralized Battery*) should be evaluated.

Bibliography

[1] U. R. Acharya, *Advances in Cardiac Signal Processing*, B. Technologies, S. Jasjit, J. A. E. Spaan, and S. M. Krishnan, Eds. Berlin Heidelberg: Springer-Verlag, 2007.

[2] A. Adler and A. Boyle, "Electrical Impedance Tomography: Tissue Properties to Image Measures," *IEEE Trans. Biomed. Eng.*, vol. 64, no. 11, pp. 2494–2504, Nov. 2017.

[3] A. Adler and W. R. B. Lionheart, "Uses and abuses of EIDORS: An extensible software base for EIT," *Physiol. Meas.*, vol. 27, no. 5, p. S25, Apr. 2006.

[4] A. Adler, J. H. Arnold, R. Bayford, A. Borsic, B. Brown, P. Dixon, T. J. C. Faes, I. Frerichs, H. Gagnon, Y. Gärber, B. Grychtol, G. Hahn, W. R. B. Lionheart, A. Malik, R. P. Patterson, J. Stocks, A. Tizzard, N. Weiler, and G. K. Wolf, "GREIT: A unified approach to 2D linear EIT reconstruction of lung images," *Physiol. Meas.*, vol. 30, no. 6, pp. S35–S55, Jun. 2009.

[5] A. Adler, P. O. Gaggero, and Y. Maimaitijiang, "Adjacent stimulation and measurement patterns considered harmful," *Physiol. Meas.*, vol. 32, no. 7, pp. 731–744, Jul. 2011.

[6] A. Adler, M. B. Amato, J. H. Arnold, R. Bayford, M. Bodenstein, S. H. Böhm, B. H. Brown, I. Frerichs, O. Stenqvist, N. Weiler, and G. K. Wolf, "Whither lung EIT: Where are we, where do we want to go and what do we need to get there?" *Physiol. Meas.*, vol. 33, no. 5, pp. 679–694, May 2012.

[7] S. Aguiar Santos, A. Robens, A. Boehm, S. Leonhardt, and D. Teichmann, "System Description and First Application of an FPGA-Based Simultaneous Multi-Frequency Electrical Impedance Tomography," *Sensors*, vol. 16, no. 8, p. 1158, Jul. 2016.

[8] C. Aliau-Bonet and R. Pallas-Areny, "On the Effect of Body Capacitance to Ground in Tetrapolar Bioimpedance Measurements," *IEEE Trans. Biomed. Eng.*, vol. 59, no. 12, pp. 3405–3411, Dec. 2012.

[9] N. Bashi, M. Karunanithi, F. Fatehi, H. Ding, and D. Walters, "Remote Monitoring of Patients With Heart Failure: An Overview of Systematic Reviews," *J Med Internet Res*, vol. 19, no. 1, pp. 1–14, Jan. 2017.

[10] R. Bayford and A. Tizzard, "Bioimpedance imaging: An overview of potential clinical applications," *Analyst*, vol. 137, no. 20, pp. 4635–4643, Sep. 2012.

[11] L. Beckmann, D. van Riesen, and S. Leonhardt, "Optimal electrode placement and frequency range selection for the detection of lung water using Bioimpedance Spectroscopy," in *2007 29th Annual International Conference of the IEEE Engineering in Medicine and Biology Society*, Aug. 2007, pp. 2685–2688.

[12] T. K. Bera, "Bioelectrical Impedance Methods for Noninvasive Health Monitoring: A Review," *J Med Eng*, vol. 2014, pp. 1–28, Jun. 2014.

[13] A. Boehm, X. Yu, W. Neu, S. Leonhardt, and D. Teichmann, "A Novel 12-Lead ECG T-Shirt with Active Electrodes," *Electronics*, vol. 5, no. 4, p. 75, Nov. 2016.

[14] J. B. Borges, F. Suarez-Sipmann, S. H. Bohm, G. Tusman, A. Melo, E. Maripuu, M. Sandstrom, M. Park, E. L. V. Costa, G. Hedenstierna, and M. Amato, "Regional lung perfusion estimated by electrical impedance tomography in a piglet model of lung collapse," *J. Appl. Physiol.*, vol. 112, no. 1, pp. 225–236, Jan. 2012.

[15] F. Braun, "Noninvasive Stroke Volume Monitoring by Electrical Impedance Tomography," Ph.D. dissertation, EPFL, Jan. 2018. [Online]. Available: https://infoscience.epfl.ch/record/233710

[16] F. Braun, M. Proenca, J. Sola, J.-P. Thiran, and A. Adler, "A Versatile Noise Performance Metric for Electrical Impedance Tomography Algorithms," *IEEE Trans. Biomed. Eng.*, vol. 64, no. 10, pp. 2321–2330, Oct. 2017.

[17] B. H. Brown and A. D. Seagar, "The Sheffield data collection system," *Clin. Phys. Physiol. Meas.*, vol. 8, no. 4A, pp. 91–97, Nov. 1987.

[18] B. G. Celler and R. S. Sparks, "Home Telemonitoring of Vital Signs - Technical Challenges and Future Directions," *IEEE J. Biomed. Health Inform.*, vol. 19, no. 1, pp. 82–91, Jan. 2015.

[19] O. Chetelat, R. Gentsch, J. Krauss, and J. Luprano, "Getting rid of the wires and connectors in physiological monitoring," in *2008 30th Annual International Conference of the IEEE Engineering in Medicine and Biology Society*, Vancouver, BC, Canada, Aug. 2008, pp. 1278–1282.

[20] O. Chételat, R. Schmid, O. Grossenbacher, M. Rapin, J. A. Porchet, C. Meier, and R. Abächerli, "Standalone dry electrode-sensors for multilead ECG monitoring in mobile patients," in *2014 8th Conference of the European Study Group on Cardiovascular Oscillations (ESGCO)*, May 2014, pp. 27–28.

[21] O. Chételat, D. Ferrario, M. Proença, J. A. Porchet, A. Falhi, O. Grossenbacher, R. Delgado-Gonzalo, N. D. Ricca, and C. Sartori, "Clinical validation of LTMS-S: A wearable system for vital signs monitoring," in *2015 37th Annual International Conference of the IEEE Engineering in Medicine and Biology Society (EMBC)*, Aug. 2015, pp. 3125–3128.

[22] Y. M. Chi and G. Cauwenberghs, "Wireless Non-contact EEG/ECG Electrodes for Body Sensor Networks," in *2010 International Conference on Body Sensor Networks*, Jun. 2010, pp. 297–301.

[23] Y. M. Chi, T. P. Jung, and G. Cauwenberghs, "Dry-Contact and Noncontact Biopotential Electrodes: Methodological Review," *IEEE Rev. Biomed. Eng.*, vol. 3, pp. 106–119, Oct. 2010.

[24] K. S. Cole, "Permeability and Impermeability of Cell Membranes for Ions," *Cold Spring Harb. Symp. Quant. Biol.*, vol. 8, no. 1, pp. 110–122, Jan. 1940.

[25] R. D. Cook, G. J. Saulnier, D. G. Gisser, J. C. Goble, J. C. Newell, and D. Isaacson, "ACT3: A high-speed, high-precision electrical impedance tomograph," *IEEE Trans. Biomed. Eng.*, vol. 41, no. 8, pp. 713–722, Aug. 1994.

[26] J. Cruz, D. Brooks, and A. Marques, "Home telemonitoring in COPD: A systematic review of methodologies and patients' adherence," *Int. J. Med. Inf.*, vol. 83, no. 4, pp. 249–263, Apr. 2014.

[27] T. Degen and H. Jäckel, "Continuous Monitoring of Electrode–Skin Impedance Mismatch During Bioelectric Recordings," *IEEE Trans. Biomed. Eng.*, vol. 55, no. 6, pp. 1711–1715, Jun. 2008.

[28] T. Degen, S. Torrent, and H. Jäckel, "Low-Noise Two-Wired Buffer Electrodes for Bioelectric Amplifiers," *IEEE Trans. Biomed. Eng.*, vol. 54, no. 7, pp. 1328–1332, Jul. 2007.

[29] E. Demidenko, A. Hartov, N. Soni, and K. Paulsen, "On Optimal Current Patterns for Electrical Impedance Tomography," *IEEE Trans. Biomed. Eng.*, vol. 52, no. 2, pp. 238–248, Feb. 2005.

[30] G. Demiris, S. M. Finkelstein, and S. M. Speedie, "Considerations for the Design of a Web-based Clinical Monitoring and Educational System for Elderly Patients," *J Am Med Inform Assoc*, vol. 8, no. 5, pp. 468–472, Sep. 2001.

[31] B. M. Eyuboglu, B. H. Brown, and D. C. Barber, "In vivo imaging of cardiac related impedance changes," *IEEE Eng. Med. Biol. Mag.*, vol. 8, no. 1, pp. 39–45, Mar. 1989.

[32] I. Frerichs, Z. Zhao, T. Becher, P. Zabel, N. Weiler, and B. Vogt, "Regional lung function determined by electrical impedance tomography during bronchodilator reversibility testing in patients with asthma," *Physiol. Meas.*, vol. 37, no. 6, pp. 698–712, May 2016.

[33] I. Frerichs, M. B. P. Amato, A. H. van Kaam, D. G. Tingay, Z. Zhao, B. Grychtol, M. Bodenstein, H. Gagnon, S. H. Böhm, E. Teschner, O. Stenqvist, T. Mauri, V. Torsani, L. Camporota, A. Schibler, G. K. Wolf, D. Gommers, S. Leonhardt, and A. Adler, "Chest electrical impedance tomography examination, data analysis, terminology, clinical use and recommendations: Consensus statement of the TRanslational EIT developmeNt stuDy group," *Thorax*, vol. 72, no. 1, pp. 83–93, Jan. 2017.

[34] I. Frerichs, B. Vogt, J. Wacker, R. Paradiso, F. Braun, M. Rapin, O. Chételat, and N. Weiler, "Wearable chest electrical impedance tomography system – a validation study in healthy volunteers," in *19th International Conference on Biomedical Applications of Electrical Impedance Tomography (EIT 2018)*, Edinburgh, UK, Jun. 2018.

[35] P. O. Gaggero, A. Adler, J. Brunner, and P. Seitz, "Electrical impedance tomography system based on active electrodes," *Physiol. Meas.*, vol. 33, no. 5, pp. 831–847, May 2012.

[36] S. Giffard-Roisin, T. Jackson, L. Fovargue, J. Lee, H. Delingette, R. Razavi, N. Ayache, and M. Sermesant, "Noninvasive Personalization of a Cardiac Electrophysiology Model From Body Surface Potential Mapping," *IEEE Trans. Biomed. Eng.*, vol. 64, no. 9, pp. 2206–2218, Sep. 2017.

[37] M. Goharian, M. Soleimani, A. Jegatheesan, K. Chin, and G. R. Moran, "A DSP Based Multi-Frequency 3D Electrical Impedance Tomography System," *Ann Biomed Eng*, vol. 36, no. 9, pp. 1594–1603, Sep. 2008.

[38] S. Grimnes and Ø. G. Martinsen, "Sources of error in tetrapolar impedance measurements on biomaterials and other ionic conductors," *J. Phys. D: Appl. Phys.*, vol. 40, no. 1, pp. 9–14, Dec. 2006.

[39] M. Guermandi, R. Cardu, E. Franchi Scarselli, and R. Guerrieri, "Active Electrode IC for EEG and Electrical Impedance Tomography With Continuous Monitoring of Contact Impedance," *IEEE Trans. Biomed. Circuits Syst.*, vol. 9, no. 1, pp. 21–33, Feb. 2015.

[40] R. Halter, A. Hartov, and K. Paulsen, "A Broadband High-Frequency Electrical Impedance Tomography System for Breast Imaging," *IEEE Trans. Biomed. Eng.*, vol. 55, no. 2, pp. 650–659, Feb. 2008.

[41] M. A. Hanson, H. C. P. Jr, A. T. Barth, K. Ringgenberg, B. H. Calhoun, J. H. Aylor, and J. Lach, "Body Area Sensor Networks: Challenges and Opportunities," *Computer*, vol. 42, no. 1, pp. 58–65, Jan. 2009.

[42] A. Hartov, R. Mazzarese, F. Reiss, T. Kerner, K. Osterman, D. Williams, and K. Paulsen, "A multichannel continuously selectable multifrequency electrical impedance spectroscopy measurement system," *IEEE Trans. Biomed. Eng.*, vol. 47, no. 1, pp. 49–58, Jan. 2000.

[43] B. Hayes, *Non-Invasive Cardiovascular Monitoring*, ser. Principles and practice series. London: BMJ Publishing, 1997, oCLC: 728660287.

[44] H. Helmholtz, "Ueber einige Gesetze der Vertheilung elektrischer Ströme in körperlichen Leitern mit Anwendung auf die thierisch-elektrischen Versuche," *Ann. Phys. Chem.*, vol. 165, no. 6, pp. 211–233, 1853.

[45] C. R. Hogge, "A self correcting clock recovery circuit," *IEEE Trans. Electron Devices*, vol. 32, no. 12, pp. 2704–2706, Dec. 1985.

[46] D. Holder, Ed., *Electrical Impedance Tomography: Methods, History, and Applications*, ser. in medical physics and biomedical engineering. Institute of Physics Publishing, Bristol, UK, 2005, oCLC: ocm57430626.

[47] S. Hong, J. Lee, J. Bae, and H.-J. Yoo, "A 10.4 mW Electrical Impedance Tomography SoC for Portable Real-Time Lung Ventilation Monitoring System," *IEEE J. Solid-State Circuits*, vol. 50, no. 11, pp. 2501–2512, Nov. 2015.

[48] S. Hong, K. Lee, U. Ha, H. Kim, Y. Lee, Y. Kim, and H.-J. Yoo, "A 4.9 mΩ -Sensitivity Mobile Electrical Impedance Tomography IC for Early Breast-Cancer Detection System," *IEEE J. Solid-State Circuits*, vol. 50, no. 1, pp. 245–257, Jan. 2015.

[49] J. C. Huhta and J. G. Webster, "60-Hz Interference in Electrocardiography," *IEEE Trans. Biomed. Eng.*, vol. BME-20, no. 2, pp. 91–101, Mar. 1973.

[50] IEC 60601-1:2005, *Medical Electrical Equipment - Part 1: General Requirements for Basic Safety and Essential Performance*, 3rd ed. Geneva, Switzerland: International Electrotechnical Commission (IEC), Dec. 2005.

[51] IEC 60601-2-25:2011, *Medical Electrical Equipment - Part 2-25: Particular Requirements for the Basic Safety and Essential Performance of Electrocardiographs*, 2nd ed. Geneva, Switzerland: International Electrotechnical Commission (IEC), Oct. 2011.

[52] IEC 60601-2-47:2012, *Medical Electrical Equipment - Part 2-47: Particular Requirements for the Basic Safety and Essential Performance of Ambulatory Electrocardiographic Systems*, 2nd ed. Geneva, Switzerland: International Electrotechnical Commission (IEC), Feb. 2012.

[53] S. C. Jun, J. Kuen, J. Lee, E. J. Woo, D. Holder, and J. K. Seo, "Frequency-difference EIT (fdEIT) using weighted difference and equivalent homogeneous admittivity: Validation by simulation and tank experiment," *Physiol. Meas.*, vol. 30, no. 10, pp. 1087–1099, Sep. 2009.

[54] M. Kim, J. Jang, H. Kim, J. Lee, J. Lee, J. Lee, K. R. Lee, K. Kim, Y. Lee, K. J. Lee, and H. J. Yoo, "A 1.4- mΩ -Sensitivity 94-dB Dynamic-Range Electrical Impedance Tomography SoC and 48-Channel Hub-SoC for 3-D Lung Ventilation Monitoring System," *IEEE J. Solid-State Circuits*, vol. 52, no. 11, pp. 2829–2842, Nov. 2017.

[55] S. Krueger-Ziolek, B. Schullcke, B. Gong, U. Müller-Lisse, and K. Moeller, "EIT based pulsatile impedance monitoring during spontaneous breathing in cystic fibrosis," *Physiol. Meas.*, vol. 38, no. 6, pp. 1214–1225, May 2017.

[56] R. Kusche, A. Malhotra, M. Ryschka, G. Ardelt, P. Klimach, and S. Kaufmann, "A FPGA-Based Broadband EIT System for Complex Bioimpedance Measurements—Design and Performance Estimation," *Electronics*, vol. 4, no. 3, pp. 507–525, Jul. 2015.

[57] S.-Y. Lee, J.-H. Hong, C.-H. Hsieh, M.-C. Liang, S.-Y. Chang Chien, and K.-H. Lin, "Low-Power Wireless ECG Acquisition and Classification System for Body Sensor Networks," *IEEE J. Biomed. Health Inform.*, vol. 19, no. 1, pp. 236–246, Jan. 2015.

[58] S. Lehmann, S. Leonhardt, C. Ngo, L. Bergmann, I. Ayed, S. Schrading, and K. Tenbrock, "Global and regional lung function in cystic fibrosis measured by electrical impedance tomography," *Pediatr Pulmonol.*, vol. 51, no. 11, pp. 1191–1199, Nov. 2016.

[59] J. R. Levick, *An Introduction to Cardiovascular Physiology*, 4th ed.   London, UK: Hodder Arnold, 2003.

[60] C.-T. Lin, L.-D. Liao, Y.-H. Liu, I.-J. Wang, B.-S. Lin, and J.-Y. Chang, "Novel Dry Polymer Foam Electrodes for Long-Term EEG Measurement," *IEEE Trans. Biomed. Eng.*, vol. 58, no. 5, pp. 1200–1207, May 2011.

[61] W. R. B. Lionheart, J. Kaipio, and C. N. McLeod, "Generalized optimal current patterns and electrical safety in EIT," *Physiol. Meas.*, vol. 22, no. 1, p. 85, Jan. 2001.

[62] O. Luppi Silva, R. Gonzalez Lima, T. Castro Martins, F. Silva de Moura, R. Seiji Tavares, and M. Sales Guerra Tsuzuki, "Influence of current injection pattern and electric potential measurement strategies in electrical impedance tomography," *Control Eng. Pract.*, vol. 58, pp. 276–286, Jan. 2017.

[63] Y. Ma, L. Miao, H. Qin, X. Chen, X. Xiong, T. Han, P. Qin, X. Ji, and P. Cai, "A new modular semi-parallel EIT system for medical application," *Biomedical Signal Processing and Control*, vol. 39, no. Sup. C, pp. 416–423, Jan. 2018.

[64] J. Malmivuo, "Principle of reciprocity solves the most important problems in bioimpedance and in general in bioelectromagnetism," *J. Phys. Conf. Ser.*, vol. 224, p. 012001, Apr. 2010.

[65] A. McEwan, G. Cusick, and D. S. Holder, "A review of errors in multi-frequency EIT instrumentation," *Physiol. Meas.*, vol. 28, no. 7, pp. S197–S215, Jun. 2007.

[66] M. M. Mellenthin, J. L. Mueller, E. D. L. B. de Camargo, F. S. de Moura, S. J. Hamilton, and R. G. Lima, "The ACE1 thoracic Electrical Impedance Tomography system for ventilation and perfusion," in *2015 37th Annual International Conference of the IEEE Engineering in Medicine and Biology Society (EMBC)*, Aug. 2015, pp. 4073–4076.

[67] T. Menden, J. Orschulik, T. Tholen, S. Leonhardt, and M. Walter, "Approach to compensate measurement errors in electrical impedance tomography," in *2017 IEEE Biomedical Circuits and Systems Conference (BioCAS)*, Oct. 2017, pp. 1–4.

[68] P. P. Mercier and A. P. Chandrakasan, "A Supply-Rail-Coupled eTextiles Transceiver for Body-Area Networks," *IEEE J. Solid-State Circuits*, vol. 46, no. 6, pp. 1284–1295, Jun. 2011.

[69] N. Meziane, J. G. Webster, M. Attari, and A. J. Nimunkar, "Dry electrodes for electrocardiography," *Physiol. Meas.*, vol. 34, no. 9, pp. R47–R69, Sep. 2013.

[70] Y. Mohamadou, T. I. Oh, H. Wi, H. Sohal, A. Farooq, E. J. Woo, and A. L. McEwan, "Performance evaluation of wideband bio-impedance spectroscopy using constant voltage source and constant current source," *Meas. Sci. Technol.*, vol. 23, no. 10, pp. 1–10, Sep. 2012.

[71] U. Mour et al, "Le tâte-cul," *Journal des Brandons*, vol. 123, no. 1, p. 69, Feb. 2018.

[72] D. T. Nguyen, C. Jin, A. Thiagalingam, and A. L. McEwan, "A review on electrical impedance tomography for pulmonary perfusion imaging," *Physiol. Meas.*, vol. 33, no. 5, pp. 695–706, May 2012.

[73] T. I. Oh, H. Wi, D. Y. Kim, P. J. Yoo, and E. J. Woo, "A fully parallel multi-frequency EIT system with flexible electrode configuration: KHU Mark2," *Physiol. Meas.*, vol. 32, no. 7, pp. 835–849, Jul. 2011.

[74] T. I. Oh, T. E. Kim, S. Yoon, K. J. Kim, E. J. Woo, and R. J. Sadleir, "Flexible electrode belt for EIT using nanofiber web dry electrodes," *Physiol. Meas.*, vol. 33, no. 10, pp. 1603–1616, Oct. 2012.

[75] P. Pandian, K. Mohanavelu, K. Safeer, T. Kotresh, D. Shakunthala, P. Gopal, and V. Padaki, "Smart Vest: Wearable multi-parameter remote physiological monitoring system," *Med. Eng. Phys.*, vol. 30, no. 4, pp. 466–477, May 2008.

[76] A. Pantelopoulos and N. Bourbakis, "A Survey on Wearable Sensor-Based Systems for Health Monitoring and Prognosis," *IEEE Trans. Syst. Man Cybern. Part C Appl. Rev.*, vol. 40, no. 1, pp. 1–12, Jan. 2010.

[77] G. Pare, M. Jaana, and C. Sicotte, "Systematic Review of Home Telemonitoring for Chronic Diseases: The Evidence Base," *J. Am. Med. Inform. Assoc.*, vol. 14, no. 3, pp. 269–277, May 2007.

[78] M. Proença, "Non-invasive hemodynamic monitoring by electrical impedance tomography," Ph.D. dissertation, EPFL, Feb. 2017. [Online]. Available: https://infoscience.epfl.ch/record/225621

[79] M. Proença, F. Braun, J. Solà, A. Adler, M. Lemay, J.-P. Thiran, and S. F. Rimoldi, "Non-invasive monitoring of pulmonary artery pressure from timing information by EIT: Experimental evaluation during induced hypoxia," *Physiol. Meas.*, vol. 37, no. 6, pp. 713–726, Jun. 2016.

[80] M. Rapin, M. Proença, F. Braun, C. Meier, J. Solà, D. Ferrario, O. Grossenbacher, J.-A. Porchet, and O. Chételat, "Cooperative dry-electrode sensors for multi-lead biopotential and bioimpedance monitoring," *Physiol. Meas.*, vol. 36, no. 4, pp. 767–783, Apr. 2015.

[81] M. Rapin, D. Ferrario, E. Haenni, J. Wacker, A. Falhi, C. Meier, J.-A. Porchet, and O. Chételat, "Electromagnetic disturbances rejection with single skin contact in the context of ECG measurements with cooperative sensors," in *2017 39th Annual International Conference of the IEEE Engineering in Medicine and Biology Society (EMBC)*, Jul. 2017, pp. 4427–4430.

[82] M. Rapin, F. Braun, A. Adler, J. Wacker, I. Frerichs, B. Vogt, and O. Chetelat, "Wearable Sensors for Frequency-Multiplexed EIT and Multilead ECG Data Acquisition," *IEEE Trans. Biomed. Eng.*, pp. 1–1, 2018.

[83] M. Rapin, J. Wacker, and O. Chételat, "Two-Wire Bus Combining Full Duplex Body-Sensor Network and Multilead Biopotential Measurements," *IEEE Trans. Biomed. Eng.*, vol. 65, no. 1, pp. 113–122, Jan. 2018.

[84] M. Rapin, Y.-J. Regamey, and O. Chételat, "Common-mode rejection in the measurement of wearable ECG with cooperative sensors," *De Gruyter Oldenbourg*, pp. 1 – 12, 2018 (in press).

[85] M. Rau, T. Oberst, R. Lares, A. Rothermel, R. Schweer, and N. Menoux, "Clock/data recovery PLL using half-frequency clock," *IEEE J. Solid-State Circuits*, vol. 32, no. 7, pp. 1156–1159, Jul. 1997.

[86] B. Razavi, *Monolithic Phase-Locked Loops and Clock Recovery Circuits: Theory and Design*. John Wiley & Sons, Apr. 1996.

[87] Y. Rudy, "Noninvasive ECG imaging (ECGI): Mapping the arrhythmic substrate of the human heart," *International Journal of Cardiology*, vol. 237, no. Sup. C, pp. 13–14, Jun. 2017.

[88] E. Santos and F. Simini, "Electrical Impedance Tomography for pulmonary oedema extent monitoring: Review and updated design," *J. Phys. Conf. Ser.*, vol. 407, p. 012024, Dec. 2012.

[89] M. Seyedi, B. Kibret, D. T. H. Lai, and M. Faulkner, "A Survey on Intrabody Communications for Body Area Network Applications," *IEEE Trans. Biomed. Eng.*, vol. 60, no. 8, pp. 2067–2079, Aug. 2013.

[90] J. Solà, A. Adler, A. Santos, G. Tusman, F. S. Sipmann, and S. H. Bohm, "Non-invasive monitoring of central blood pressure by electrical impedance tomography: First experimental evidence," *Med. Biol. Eng. Comput.*, vol. 49, no. 4, pp. 409–415, Apr. 2011.

[91] J. S. Steinberg, N. Varma, I. Cygankiewicz, P. Aziz, P. Balsam, A. Baranchuk, D. J. Cantillon, P. Dilaveris, S. J. Dubner, N. El-Sherif, J. Krol, M. Kurpesa, M. T. La Rovere, S. S. Lobodzinski, E. T. Locati, S. Mittal, B. Olshansky, E. Piotrowicz, L. Saxon, P. H. Stone, L. Tereshchenko, G. Turitto, N. J. Wimmer, R. L. Verrier, W. Zareba, and R. Piotrowicz, "2017 ISHNE-HRS expert consensus statement on ambulatory ECG and external cardiac monitoring/telemetry," *Heart Rhythm*, vol. 14, no. 7, pp. e55–e96, Jul. 2017.

[92] Timpel, "Timpel Precision Ventilation," 2018. [Online]. Available: http://www.timpel.com.br/

[93] C. J. C. Trepte, C. Phillips, J. Solà, A. Adler, B. Saugel, S. Haas, S. H. Bohm, and D. A. Reuter, "Electrical impedance tomography for non-invasive assessment of stroke volume variation in health and experimental lung injury," *Br. J. Anaesth.*, vol. 118, no. 1, pp. 68–76, Jan. 2017.

[94] A. C. M. van Rijn, A. Peper, and C. A. Grimbergen, "High-quality recording of bioelectric events," *Med. Biol. Eng. Comput.*, vol. 29, no. 4, pp. 433–440, Jul. 1991.

[95] B. Vogt, S. Pulletz, G. Elke, Z. Zhao, P. Zabel, N. Weiler, and I. Frerichs, "Spatial and temporal heterogeneity of regional lung ventilation determined by electrical impedance tomography during pulmonary function testing," *Journal of Applied Physiology*, vol. 113, no. 7, pp. 1154–1161, Aug. 2012.

[96] B. Vogt, Z. Zhao, P. Zabel, N. Weiler, and I. Frerichs, "Regional lung response to bronchodilator reversibility testing determined by electrical impedance tomography in chronic obstructive pulmonary disease," *American Journal of Physiology-Lung Cellular and Molecular Physiology*, vol. 311, no. 1, pp. L8–L19, May 2016.

[97] A. Vonk-Noordegraaf, A. Janse, J. T. Marcus, J. G. F. Bronzwaer, P. E. Postmus, T. J. C. Faes, and P. M. J. M. de Vries, "Determination of stroke volume by means of electrical impedance tomography," *Physiol. Meas.*, vol. 21, no. 2, pp. 285–293, May 2000.

[98] J. Wacker, O. Chételat, M. Rapin, C. Meier, J.-A. Porchet, Y. Chang, B. Pierscionek, R. Kayyali, S. Elnabhani, and N. Philip, "Electrical and Mechanical Design of a Vest Measuring a Large Set of Physiological Signals," in *2014 4th International Conference on Wireless Mobile Communication and Healthcare - Transforming Healthcare Through Innovations in Mobile and Wireless Technologies (MOBIHEALTH)*, Nov. 2014, pp. 47–50.

[99] J. Wang, T. Fujiwara, T. Kato, and D. Anzai, "Wearable ECG Based on Impulse-Radio-Type Human Body Communication," *IEEE Trans. Biomed. Eng.*, vol. 63, no. 9, pp. 1887–1894, Sep. 2016.

[100] J. G. Webster, "Reducing Motion Artifacts and Interference in Biopotential Recording," *IEEE Trans. Biomed. Eng.*, vol. BME-31, no. 12, pp. 823–826, Dec. 1984.

[101] A. Welinder, L. Sörnmo, D. Q. Feild, C. L. Feldman, J. Pettersson, G. S. Wagner, and O. Pahlm, "Comparison of Signal Quality Between Easi and Mason-Likar 12-Lead Electrocardiograms During Physical Activity," *Am J Crit Care*, vol. 13, no. 3, pp. 228–234, Jan. 2004.

[102] A. J. Wilson, P. Milnes, A. R. Waterworth, R. H. Smallwood, and B. H. Brown, "Mk3.5: A modular, multi-frequency successor to the Mk3a EIS/EIT system," *Physiol. Meas.*, vol. 22, no. 1, pp. 49–54, Jan. 2001.

[103] F. N. Wilson and F. D. Johnston, "The vectorcardiogram," *American Heart Journal*, vol. 16, no. 1, pp. 14–28, Jul. 1938.

[104] G. K. Wolf, C. Gómez-Laberge, J. S. Rettig, S. O. Vargas, C. D. Smallwood, S. P. Prabhu, S. H. Vitali, D. Zurakowski, and J. H. Arnold, "Mechanical Ventilation Guided by Electrical Impedance Tomography in Experimental Acute Lung Injury," *Crit. Care Med.*, vol. 41, no. 5, pp. 1296–1304, May 2013.

[105] World Health Organization, *Global Status Report on Noncommunicable Diseases 2014: Attaining the Nine Global Noncommunicable Diseases Targets; a Shared Responsibility.* Geneva: World Health Organization, 2014, oCLC: 907517003.

[106] J. Xu, B. Busze, C. Van Hoof, K. A. A. Makinwa, and R. F. Yazicioglu, "A 15-Channel Digital Active Electrode System for Multi-Parameter Biopotential Measurement," *IEEE J. Solid-State Circuits*, vol. 50, no. 9, pp. 2090–2100, Sep. 2015.

[107] G. Yang, J. Chen, Y. Cao, H. Tenhunen, and L.-R. Zheng, "A novel wearable ECG monitoring system based on active-cable and intelligent electrodes," in *HealthCom 2008 - 10th International Conference on e-Health Networking, Applications and Services*, Jul. 2008, pp. 156–159.

[108] G. Yang, J. Chen, L. Xie, J. Mao, H. Tenhunen, and L.-R. Zheng, "A Hybrid Low Power Biopatch for Body Surface Potential Measurement," *IEEE J. Biomed. Health Inform.*, vol. 17, no. 3, pp. 591–599, May 2013.

[109] R. Yerworth and R. Bayford, "The effect of serial data collection on the accuracy of electrical impedance tomography images," *Physiol. Meas.*, vol. 34, no. 6, pp. 659–669, Jun. 2013.

[110] R. J. Yerworth, I. Frerichs, and R. Bayford, "Analysis and compensation for errors in electrical impedance tomography images and ventilation-related measures due to serial data collection," *J. Clin. Monit. Comput.*, vol. 31, no. 5, pp. 1093–1101, Oct. 2017.

[111] L. Yu, Q. Jin, Z. Zhou, L. Wu, and B. He, "Three-Dimensional Noninvasive Imaging of Ventricular Arrhythmias in Patients with Premature Ventricular Contractions," *IEEE Trans. Biomed. Eng.*, Oct. 2017.

[112] X. Yu, A. Boehm, W. Neu, B. Venema, N. Marx, S. Leonhardt, and D. Teichmann, "A wearable 12-lead ECG T-shirt with textile electrodes for unobtrusive long-term monitoring – Evaluation of an ongoing clinical trial," in *EMBEC & NBC 2017*, ser. IFMBE Proceedings. Springer, Singapore, Jun. 2017, pp. 703–706.

[113] L. Zhang, H. Wang, and L. Zhang, "Single source current drive patterns for electrical impedance tomography," in *2010 IEEE Instrumentation Measurement Technology Conference Proceedings*, May 2010, pp. 1477–1480.

[114] Z. Zhao, R. Fischer, I. Frerichs, U. Müller-Lisse, and K. Möller, "Regional ventilation in cystic fibrosis measured by electrical impedance tomography," *Journal of Cystic Fibrosis*, vol. 11, no. 5, pp. 412–418, Sep. 2012.

[115] P. Zipp and H. Ahrens, "A model of bioelectrode motion artefact and reduction of artefact by amplifier input stage design," *Journal of Biomedical Engineering*, vol. 1, no. 4, pp. 273–276, Oct. 1979.

[116] S. Zlochiver, M. Arad, M. Radai, D. Barak-Shinar, H. Krief, T. Engelman, R. Ben-Yehuda, A. Adunsky, and S. Abboud, "A portable bio-impedance system for monitoring lung resistivity," *Med. Eng. Phys.*, vol. 29, no. 1, pp. 93–100, Jan. 2007.

Michaël RAPIN

Rte. de la Ferme 32

1470 Estavayer-le-Lac

Switzerland

Phone: +41 79 796 41 64

Email: michael.rapin@gmail.com

21st of December 1985

with partner

Swiss & Italian citizenship

M. Sc. in Electrical Engineering, Electronics and Firmware

Research Interests

My research interests are related to the development of the next generation of wearables that will integrate large numbers of electronic sensors for multi-physiological parameters measurement with high spatial and temporal resolution, with a special focus on biopotentials (such as ECG) and bioimpedance.

Education

PhD candidate   2014 - now
Department of Health Sciences and Technology (D–HEST), ETHZ, Zürich & CSEM, Neuchâtel (CH)

Master's degree in Electrical Engineering (Energy)   2009 - 2012
EPFL, Lausanne (CH)

Bachelor's degree in Electrical Engineering (Mechatronics)   2004 - 2007
HEIG–VD, Yverdon-les-Bains (CH)

Federal Diploma of Vocational Education and Training in Electronics   2001 - 2004
CPNV, Yverdon-les-Bains (CH)

Professional Experience

Senior R&D Engineer, Wearable sensors design, Medical Application   2018 - now
CSEM, Neuchâtel (CH)

R&D Engineer, Wearable sensors design, Medical Application   2012 - 2018
CSEM, Neuchâtel (CH)

R&D Engineer (Internship), Signal Processing, Medical Application   2012 (4 mos)
Department of Systems and Computer Engineering, Carleton University, Ottawa (CA)

R&D Engineer (Master Thesis), Electromagnetic Actuators, Medical Application   2011 (6 mos)
CSEM, Neuchâtel (CH) & Integrated Actuators Laboratory (LAI), EPLF, Lausanne (CH)

R&D Engineer, Industrial Electronics, Motion Control   2007 - 2009
Institute of Industrial Automation (IAI), HEIG–VD, Yverdon-les-Bains (CH)

Featured Skills

Electronics, Embedded systems, Wearable sensors, Biomedical instrumentation, Medical devices, Electrocardiogram (ECG), Bioimpedance, Electrical impedance tomography (EIT), IEC 60601, ISO 13485 , Analog and digital signal processing, Microcontroller, Power electronics, Motion control, PCB design.

Languages

French   Native language

English   Professional working proficiency

German   Limited working proficiency

Volunteer Experience

Steering committee member (Youth section responsible), TriClub Esta-Broye	2017 - now
Coach for Youth (triathlon), with brevet, TriClub Esta-Broye	2016 - now
Steering committee member (secretary), Football Club Corcelles-près-Payerne	2009 - 2016

Personal Interests

Sports: long distance triathlon, ski mountaineering, hiking

Art: music, cinema, photography

Travelling

Publication List

This section is a chronological list of all publications (**journals**, conferences, and *scientific reports*) related to my PhD thesis.

First author contributions

<u>M. Rapin</u>, M. Proença, F. Braun, C. Meier, J. Solà, D. Ferrario, O. Grossenbacher, J.-A. Porchet, and O. Chételat, "Cooperative dry-electrode sensors for multi-lead biopotential and bioimpedance monitoring," *Physiol. Meas.*, vol. 36, no. 4, pp. 767-783, April 2015.

<u>M. Rapin</u>, J. Wacker, and O. Chételat, "Two-wire bus combining full duplex body-sensor network and multilead biopotential measurements," *IEEE Trans. Biomed. Eng.*, vol. 65, no. 1, pp. 113-122, Jan. 2018.

<u>M. Rapin</u>, F. Braun, A. Adler, I. Frerichs, J. Wacker, B. Vogt, and O. Chételat, "Wearable Sensors for Frequency-Multiplexed EIT and Multilead ECG Data Acquisition," *IEEE Trans. Biomed. Eng.*, 2018, early access, DOI: 10.1109/TBME.2018.2857199.

<u>M. Rapin</u>, Y.-J. Regamey, and O. Chételat, "Common-mode rejection in the measurement of wearable ECG with cooperative sensors," *De Gruyter – Autom.*, 2018 (in press).

<u>M. Rapin</u>, M. Proença, F. Braun, and O. Chételat, "Cooperative Dry-Electrode Sensors for Multilead ECG monitoring," Annual Swiss Society for Biomedical Engineering (SSBE) meeting, Zürich (CH), Aug. 2014.

<u>M. Rapin</u>, M. Proença, F. Braun, J. Solà, P. O. Gaggero, A. Adler, M. Correvon, and O. Chételat, "Discarding the Direct Component in Electrical Impedance Tomography," 15th International Conference on Biomedical Application of Electrical Impedance Tomography, Gananoque (CA), April 2014.

<u>M. Rapin</u>, M. Proença, F. Braun, J. Solà, and O. Chételat, "Cooperative sensors: a new approach towards wearable EIT systems," 16th International Conference on Biomedical Application of Electrical Impedance Tomography, Neuchâtel (CH), June 2015.

<u>M. Rapin</u>, F. Braun, M. Proença, J. Wacker, and O. Chételat, "Wearable 12-lead ECG monitoring system by means of cooperative sensors," Annual Swiss Society for Biomedical Engineering (SSBE) meeting, Neuchâtel (CH), Aug. 2015.

<u>M. Rapin</u>, J. Wacker, O. and Chételat, "Cooperative sensors: a new wired body-sensor-network approach for wearable biopotential measurement," 5th International Conference on Wireless Mobile Communication and Healthcare – MobiHealth, London (GB), Oct. 2015.

<u>M. Rapin</u>, F. Braun, J. Wacker, and O. Chételat, "A wearable EIT system based on cooperative sensors," 18th International Conference on Biomedical Application of Electrical Impedance Tomography, Hanover (USA), June 2017.

<u>M. Rapin</u>, D. Ferrario, E. Haenni, J. Wacker, A. Falhi, C. Meier, J.-A. Porchet, and O. Chételat, "Electromagnetic Disturbances Rejection with Single Skin Contact in the Context of ECG Measurements with Cooperative Sensors," 39th Annual International Conference of the IEEE Engineering in Medicine and Biology Society (EMBC), Jeju Island (Korea), pp. 4427-4430, July 2017.

<u>M. Rapin</u>, F. Braun, J. Wacker, and O. Chételat, "A Wearable System for Multichannel Bioimpedance and Multilead ECG Monitoring," Annual Swiss Society for Biomedical Engineering (SSBE) meeting, Winterthur (CH), Aug. 2017.

<u>M. Rapin</u>, D. Ferrario, C. Pellaton, E. Haenni, S. Dasen, and O. Chételat, "ECG quality assessment of dry-electrode cooperative sensors," 4th European Congress on eCardiology and eHealth, Berlin (DE), November 2017.

<u>M. Rapin</u>, F. Braun, J. Wacker, and O. Chételat, "Performance Assessment of a Wearable EIT System," 19th International Conference on Biomedical Application of Electrical Impedance Tomography, Edinburgh (UK), June 2018.

M. Rapin, O. Chételat, C. Meier, J.-A. Porchet, J. Wacker, A. Falhi, A. De Sousa, M. Frosio, and R. Rusconi, "ECG12CS - 12-lead ECG monitoring system with cooperative sensors," CSEM's scientific and technical report 2015.

M. Rapin, F. Braun, J. Wacker, E. Haenni, J.-A. Porchet, A. Falhi, C. Meier, and O. Chételat, "A wearable system based on cooperative sensors for multi-lead ECG monitoring and electrical impedance tomography imaging," CSEM's scientific and technical report 2017.

M. Rapin, Y.-J. Regamey, and O. Chételat, "Common-mode rejection in the measurement of wearable ECG with cooperative sensors," CSEM's scientific and technical report 2018 (in press).

Co-author contributions

F. Braun, M. Proença, <u>M. Rapin</u>, M. Lemay, A. Adler, B. Grychtol, J. Solà, and J.-P. Thiran, "Aortic blood pressure measured via EIT: investigation of different measurement settings," *Physiol. Meas.*, vol. 36, no. 6, pp. 1147-1159, June 2015.

M. Proença, F. Braun, <u>M. Rapin</u>, J. Solà, A. Adler, B. Grychtol, S. H. Bohm, M. Lemay, and J.-P. Thiran, "Influence of heart motion on cardiac output estimation by means of electrical impedance tomography," *Physiol. Meas.*, vol. 36, no. 6, pp. 1075-1091, June 2015.

C. J. C. Trepte, C. R. Phillips, J. Solà, A. Adler, S. A. Haas, <u>M. Rapin</u>, S. H. Bohm, and D. A. Reuter, "Electrical impedance tomography (EIT) for quantification of pulmonary edema in acute lung injury," *Critical Care*, vol. 20, no. 1, pp. 1-9, Jan. 2016.

C. J. C. Trepte, C. R. Philips, J. Solà, A. Adler, <u>M. Rapin</u>, S. H. Böhm, and D. A. Reuter, "Assessment of Extravascular lung water by electrical impedance tomography in acute lung injury," ESICM2013, Paris (FR), Nov. 2013.

C. J. C. Trepte, C. R. Philips, J. Solà, A. Adler, <u>M. Rapin</u>, S. H. Böhm, and D. A. Reuter, "Measurement of heart-lung interactions by electrical impedance tomography," ESICM2013, Paris (FR), Nov. 2013.

J. Wacker, O. Chételat, <u>M. Rapin</u>, C. Meier, J.-A. Porchet, Y. L. Chang, B. K. Pierscionek, R. Kayyali, S. Elnabhani, and N. Philip, "Electrical and Mechanical Design of a Vest Measuring a Large Set of Physiological Signals," 4th International Conference on Wireless Mobile Communication and Healthcare – MobiHealth, Athene (GR), Nov. 2014.

M. Proença, <u>M. Rapin</u>, F. Braun, J. Solà, M. Lemay, and J.-P. Thiran, "Cardiac Output Measured by Electrical Impedance Tomography: Applications and Limitations," IEEE BIOCAS 2014, Lausanne (CH), Oct. 2014.

F. Braun, M. Proença, <u>M. Rapin</u>, B. Grychtol, M. Bührer, P. Krammer, S. H. Bohm, M. Lemay, J. Solà, and J.-P. Thiran, "Non-invasive blood pressure via Electrical Impedance Tomography (EIT): Influence of belt position," Annual Swiss Society for Biomedical Engineering (SSBE) meeting, Zürich (CH), Aug. 2014.

M. Proença, F. Braun, <u>M. Rapin</u>, J. Solà, A. Adler, B. Grychtol, M. Bührer, P. Krammer, S. H. Bohm, M. Lemay, and J.-P. Thiran, "Non-invasive stroke volume estimation via electrical impedance tomography: influence of heart motion," Annual Swiss Society for Biomedical Engineering (SSBE) meeting, Zürich (CH), Aug. 2014.

O. Chételat, <u>M. Rapin</u>, O. Grossenbacher, J.-A. Porchet, C. Meier, R. Schmid, and R. Abächerli, "Standalone electrode-sensors for multilead ECG monitoring in mobile patients," 8th Conference of the European Study Group on Cardiovascular Oscillations, ESGCO, Trento (IT), May 2014.

F. Braun, M. Proença, <u>M. Rapin</u>, B. Grychtol, M. Bührer, P. Krammer, S. H. Bohm, M. Lemay, J. Solà, and J.-P. Thiran, "Comparing belt positions for monitoring the descending aorta by EIT," 15th International Conference on Biomedical Application of Electrical Impedance Tomography, Gananoque (CA), April 2014.

M. Proença, F. Braun, <u>M. Rapin</u>, J. Solà, A. Adler, B. Grychtol, M. Bührer, P. Krammer, S. Böhm, M. Lemay, and J.-P. Thiran, "Influence of heart motion on EIT-based stroke volume estimation," 15th International Conference on Biomedical Application of Electrical Impedance Tomography, Gananoque (CA), April 2014.

M. Proença, F. Braun, M. Lemay, B. Grychtol, M. Bührer, M. Rapin, P. Krammer, S. Böhm, J. Solà, and J.-P. Thiran, "Understanding the Genesis of Cardiac Signals in Electrical Impedance Tomography," 7th International Conference on Bio-inspired Systems and Signal Processing - BIOSIGNALS 2014, March 2014.

F. Braun, M. Proença, M. Rapin, X. Alba, K. Lekadir, M. Lemay, J. Solà, A. F. Frangi, and J.-P. Thiran, "4D Heart Model Helps Unveiling Contributors to Cardiac EIT Signal," 16th International Conference on Biomedical Application of Electrical Impedance Tomography, Neuchâtel (CH), June 2015.

M. Proença, F. Braun, M. Rapin, J. Solà, M. Lemay, and J.-P. Thiran, "Feasibility of EIT-based pulmonary arterial pressure monitoring," 16th International Conference on Biomedical Application of Electrical Impedance Tomography, Neuchâtel (CH), June 2015.

O. Chételat, M. Rapin, C. Meier, A. Bischof, and M. K. Augustyniak, "Synchronization and communication of cooperative sensors," 37th annual international conference of the IEEE Engineering in Medicine and Biology Society, Milan (IT), Aug. 2015.

M. Proença, F. Braun, M. Rapin, J. Solà, M. Lemay, and J.-P. Thiran, "Non-invasive pulmonary artery pressure monitoring: a pulse wave velocity approach," Annual Swiss Society for Biomedical Engineering (SSBE) meeting, Neuchâtel (CH), Aug. 2015.

F. Braun, M. Proença, M. Rapin, X. Alba, K. Lekadir, M. Lemay, J. Solà, A. F. Frangi, and J.-P. Thiran, "Stroke volume measured via electrical impedance tomography (EIT): a simulation based feasibility study," Annual Swiss Society for Biomedical Engineering (SSBE) meeting, Neuchâtel (CH), Aug. 2015.

O. Chételat, J. Wacker, M. Rapin, J.-A. Porchet, C. Meier, A. Falhi, E. Haenni, L. Caldani, C. Mancuso, R. Paradiso, and L. Arneth, "New biosensors and wearables for cardiorespiratory telemonitoring," BHI 2016, Las Vegas (USA), Feb. 2016.

J. Wacker, M. Rapin, P. Theurillat, M. Crettaz, P. Liechti, E. Haenni, and O. Chételat "ASICSENSE: A highly integrated thin and soft sensor system for ECG and bioimpedance measurement," World Congress on Medical Physics and Biomedical Engineering, Prague (CZ), June 2018.

I. Frerichs, B. Vogt, J. Wacker, R. Paradiso, F. Braun, M. Rapin, O. Chételat, and N. Weiler, "Wearable chest electrical impedance tomography system – a validation study in healthy volunteers," 19th International Conference on Biomedical Application of Electrical Impedance Tomography, Edinburgh (Scotland), June 2018.

O. Chételat, O. Grossenbacher, J.-A. Porchet, M. Rapin, C. Meier, R. Gentsch, L. Zhou, and M. Correvon, "MONIMIP – Standalone Sensors for Physiological Monitoring," CSEM's scientific and technical report 2013.

O. Chételat, M. Rapin, J.-A. Porchet, C. Meier, J. Wacker, M. Frosio, and P. Pilloud, "MONIMIP – Wearable EIT System with Cooperative Sensors," CSEM's scientific and technical report 2014.

F. Braun, M. Proença, M. Rapin, M. Lemay, and J. Solà, "Blood Pressure Monitoring via EIT: Optimizing the Technology", CSEM's scientific and technical report 2014.

O. Chételat, A. Bischof, C. Meier, E. Haenni, J.-A. Porchet, J. Solà, M. Rapin, M. K. Augustyniak, and Y. Zha, "MiniNOB - Miniaturized Wearable System for NOBP Measurement", CSEM's scientific and technical report 2015.

J. Wacker, O. Chételat, M. Rapin, E. Haenni, J.-A. Porchet, A. Falhi, C. Meier, F. Braun, A. De Sousa, and R. Rusconi, "WELCOME: Versatile Wearable Sensors for Monitoring Cardiopulmonary Diseases", CSEM's scientific and technical report 2016.

P. Theurillat, M. Rapin, O. Chételat, and P. Liechti, "Demonstration of a proprietary dry electrode chip for ECG and bioimpedance measurements", CSEM's scientific and technical report 2017.

O. Chételat, M. Rapin, D. Ferrario, E. Haenni, S. Dasen, C. Meier, A. Falhi, J. Wacker, and C. Pellaton, "ECG quality assessment of dry-electrode cooperative sensors", CSEM's scientific and technical report 2017.

D. Ferrario, P. Theurillat, A. De Sousa, M. Frosio, M. Proença, C. Verjus, M. Rapin, P. Liechti, and O. Chételat, "Chest based PPG for pulse oximetry and non-occlusive blood pressure monitoring," CSEM's scientific and technical report 2018 (in press).

A. Fivaz, O. Chételat, K. Badami, M. Rapin, J.-A. Porchet, M. Crettaz, and J. Wacker, "Low-cost low-power cooperative sensors," CSEM's scientific and technical report 2018 (in press).